Malignant Progression Impacts Small Extracellular Vesicle (sEV) Interstitial Transport and Spatial Distribution

By

PETER A. SARIANO
DISSERTATION

Submitted in partial satisfaction of the requirements for the degree of

DOCTOR OF PHILOSOPHY

in

Biomedical Engineering

in the

OFFICE OF GRADUATE STUDIES

of the

UNIVERSITY OF CALIFORNIA

DAVIS

Approved:

Steven C. George, Chair

Randy Carney

Alexander D. Borowsky

Committee in Charge

2022

Acknowledgements

I would like to thank first and foremost, Dr. Steven George, and all of the members in the George lab for their support, generosity, and comradery over the course of the PhD. This work could not have been performed without your guidance, training, and valuable input to strengthen the science performed in this body of work. Thank you to my committee members, Dr. Randy Carney and Dr. Sandy Borowsky, for providing critical feedback and advice at all stages of my project development. Special thanks to members of the Carney lab and the Simon lab for providing training and advice on many of the experiments and techniques used in this work. I am grateful for the uncompromising collaborative and generous atmosphere in the Department of Biomedical Engineering at UC Davis, without which, this work could not have been performed. Finally, I would like to thank my friends (old and new), family, and Liz for supporting me throughout the trying process which is the PhD. I could not have done it without you.

Abstract

From 2000 to 2015, 97% of clinical trials in oncology failed, in part, due to an incomplete understanding of the dynamic tumor microenvironment (TME). The interplay between the developing neoplasm, resident immune and stromal cells, the extracellular matrix, and signaling molecules results in a complex balance that can promote or prevent tumor progression. An improved understanding of the relationship between these features will facilitate the development of novel cancer therapeutics.

The primary goal of this thesis is to characterize how cancer cell-secreted small extracellular vesicles (sEV) are transported and distributed within the interstitial space of the TME. sEVs influence cancer progression through interactions with a range of cell populations in the TME. However, how sEVs are physically distributed within the interstitial matrix, and how this distribution is altered over the course of malignant cancer progression is poorly defined.

To assess sEV interstitial transport, sEVs were isolated from the MCF10 series—a model human cell line of breast cancer progression. sEV characterization demonstrated increasing presence of laminin-binding integrins α3β1 and α6β1 on sEVs as the malignant potential of the MCF10 cells increased. Diffusion experiments using fluorescence recovery after photobleaching (FRAP) provided quantitative characterization of diffusion and kinetic binding parameters between bulk sEVs and a laminin-rich ECM, and demonstrated increased accumulation of bound sEVs in the matrix as the malignancy of the parent cell increased. *In silico* finite element models illustrated sEV accumulation in the matrix resulting in higher bound interstitial sEV concentrations as well as the formation of a transient spatial gradient. Subsequent *in vitro* microfluidic device convective flow experiments confirmed enhanced concentration of sEVs in the matrix and the formation of interstitial concentration gradients mediated by integrin interactions with laminin-rich ECM. Taken together, these studies demonstrate that sEV interstitial transport, concentration,

and spatial distribution are partially dependent on integrin binding to laminin, and evolves with cancer cell malignancy.

Table of Contents

Chapter 1: Introduction 1
Background 1
Hypothesis and Study Strategy 8
Chapter 2: Materials and Methods 13
Cell culture 13
sEV Isolation 13
Nanoparticle tracking analysis (NTA) 14
Transmission electron microscopy (TEM) 15
Western blot 15
Single sEV protein characterization-ExoView 16
The microfluidic platform 16
In vitro diffusion experiments 17
Particle tracking 18
Fluorescence recovery after photobleaching (FRAP) Imaging 19
FRAP analysis 19
Finite element simulations 21
In vitro microfluidic device convective flow experiments 22
Monocyte migration 23
Immunofluorescence 24
Statistical analysis and figure generation 24
Chapter 3: Characterization of Increasingly Malignant sEVs 25
Chapter 4: sEV Diffusive Transport through Laminin-Rich ECM 33
Chapter 5: Finite Element Model of sEV Convective Transport in a Microfluidic Device 44
Chapter 6: Convective Transport of sEVs in a Microfluidic Device 55
Chapter 7: Discussion and Conclusion 63
Chapter 8: Future Directions 71
References 74

Figures

Figure 1. Sample diffusion coefficients…….. 9
Figure 2. Graphical abstract…….. 10
Figure 3. Isolation protocol yields sEVs……... 25
Figure 4. Isolated sEVs possess appropriate tetraspanin markers……. 26
Figure 5. sEVs are stained with CellTrace Far Red (CTFR) and are visible via confocal microscopy…… 28
Figure 6. Select sEV isolates possess laminin-binding integrins α3, α6, β1 by western blotting……... 30
Figure 7. Increasing sEV presence of laminin-binding integrins α3, α6, β1 with malignancy…. 30
Figure 8. Variable integrin colocalization across MCF10 series sEVs…… 31
Figure 9. Graphical depiction of integrin activation states…… 33
Figure 10. Graphical depiction of integrin activation states…….. 34
Figure 11. 100 nm beads show diminished D_{eff} in matrix…….. 35
Figure 12. sEV diffusive transport is influenced by anti-integrin blocking antibodies……... 36
Figure 13. Characteristic fluorescence recovery after photobleaching (FRAP) curve……. 37
Figure 14. FRAP methodology is validated with 40 kDa dextran, 150 kDa dextran, and 100 nm fluorescent beads…… 38
Figure 15. MCF10 series sEVs can be fit by FRAP equations……. 39
Figure 16. Sensitivity analysis demonstrates sensitivity of fitting procedure……. 40
Figure 17. sEV diffusive transport is impacted by parent cell malignancy……. 40
Figure 18. Raw curves reflect similar trend as fitted data……. 41
Figure 19. Increased sEV binding with parent cell malignancy…… 41
Figure 20. sEV D_{eff} does not vary with parent cell malignancy…… 42
Figure 21. sEV diffusive transport is not fully explained by integrin activation state…… 43
Figure 22. sEV bind matrix, and binding sites are in excess…… 46
Figure 23. Low diffusion coefficients significantly impact sEV diffusive transport……. 47
Figure 24. Higher convective flow flattens soluble and bound sEV gradients……... 50
Figure 25. Small molecule soluble mediator convective transport differs from sEV transport by D_{eff} alone…….. 52
Figure 26. sEV form transient free and bound concentration gradients……. 53
Figure 27. The experimental design to assess sEV convective flow…….. 55
Figure 28. Interstitial fluid velocity was determined via experimental dextran flow and computational modeling…….. 56
Figure 29. Representative images of devices after T=30 min of convective flow……. 59
Figure 30. sEV convective transport is affected by parent cell malignancy and integrin activation state……... 60
Figure 31. sEV convective transport is affected by integrin activation state…….. 62
Figure 32. MCF10 series sEVs influence monocyte chemotaxis……. 72
Figure 33. The MCF10 series expresses CX3CL1…… 73

Tables

Table 1. The percentage of MCF10 series sEVs with colocalized integrins. 32
Table 2. Baseline modeling parameters used for *in silico* COMSOL simulations. 44
Table 3. Kinetic binding parameters for several theoretical sEV binding states. 45
Table 4. Peclet numbers calculated for baseline interstitial flow velocity 0.5 µm/sec. 51
Table 5. Integrin activation state assessed by each experimental convective flow experimental condition 58

Chapter 1: Introduction

Background

From 2000 to 2015, 97% of clinical trials in oncology failed[1], in part, due to an inability to overcome heterogeneous and dynamic tumor microenvironments. The tumor microenvironment (TME) constitutes the physical location of the developing tumor as well as adjacent tissues and resident cell populations which have the potential to influence tumor progression[2]. Conventional therapeutic strategies, which remain the most common first line therapies across most advanced solid cancers, typically include systemically administered chemotherapies, radiation therapy, surgical excision, or a combination[3,4]. These strategies all focus on exploiting classic characteristics of the developing neoplasm such as cellular genetic instability and mutation, dysregulated cellular metabolism, and resisting apoptotic cellular death[5,6] to prevent (or at the very least slow) progression towards invasive disease.

More recently, successes of monoclonal antibody targeted therapies such as trastuzumab (Herceptin; anti-HER2/neu) and bevacizumab (Avastin; anti-VEGF) in solid tumors demonstrated the efficacy of treatment strategies targeting specific soluble mediators in the TME[7,8]. The extraordinary growth and clinical successes of onco-immunotherapies in the mid-late 2010's including anti-PD-1 and anti-PD-L1 checkpoint inhibitors[9] and CAR-T cell therapy[10] highlighted the concept that tumor growth could be modulated by factors external to the primary tumor[11]. The TME is multifaceted with profound heterogeneity (both inter- and intra-tumorally)[12], and the growing appreciation of this concept has revolutionized cancer treatment.

Despite improvements in therapy regimens, there remains a need for more efficacious treatment strategies[7]. This has prompted the field to reevaluate *why* therapies underperform (often with severe side effects), including the underlying causes. Reevaluation of tumorigenesis beginning in the late 20th century and continuing today, has provided a new appreciation that the

TME can promote or prevent tumor progression. The features of the TME that influence tumor progression are numerous and dynamic. Extensive reviews have focused on describing these features in depth[13–18]. Key characteristics of the TME, besides the developing neoplasm, include the extracellular matrix (ECM)[19], immune cell populations[20], stromal cell populations[21], variations in biophysical parameters such as interstitial flow rate and oxygen gradients[22], and soluble mediators such as cytokines, chemokines, and exosomes[23,24].

The interplay between each of these components results in a complex balance of features that can promote or prevent tumor progression and is dynamic over the course of tumor evolution. Though each TME is unique and some features have been shown to dominate certain types of cancers (e.g. non-small cell lung cancer is characteristically immunologically "hot" and often contains a robust anti-tumor immune cell infiltrate while breast tumors are often considered immunologically "cold" by comparison[25]), an understanding of the interactions between all features is required for a comprehensive understanding of the TME. For the purposes of this thesis, soluble mediators, specifically small extracellular vesicles (exosomes) were considered in the context of breast cancer progression.

"Extracellular vesicle" (EV) is the general term describing a lipid-bilayer particle released from a cell. Apoptotic bodies (1000-5000 nm), intermediate microvesicles (200-1000 nm), and exosomes (30-150 nm) are examples of EVs, each with distinct biogenesis, cargo, and functional interaction with recipient cells[26–28]. Numerous studies have implicated the involvement of exosomes in a variety of cancers[29]. The multivesicular endosomal origin of exosomes results in vesicles with a lipid-bilayer orientation and internal composition that mirrors parent cells[27]. Consequently, exosomes carry membrane bound proteins (e.g. integrins) and are enriched in nucleic acids (DNA and coding and noncoding RNA), chemokines, and cytosolic proteins representative of the parent cell which enables long distance cell-to-cell signaling[26].

The role of exosomes in cancer derives from their unique transport properties (compared to single molecule cytokines and chemokines) as well as their diverse cargo capable of altering

the phenotype of recipient cells. Patients suffering from breast cancer have two times the number of circulating exosomes, and these vesicles are enriched in proteins and miRNA capable of eliciting an immune response[30]. Exosomes released from primary tumors survive in the circulation and have been shown to target specific tissues to prime a pre-metastatic niche in the pancreas, lungs, and lymph nodes[29]. Cancer-derived exosomes alter the phenotype of T-cells[31], natural killer cells[32], dendritic cells[33], and confer an immunosuppressive phenotype to macrophages[34–38]. Exosomes isolated from breast cancer cell lines also encourage monocyte survival[39], and can harbor the chemokine CCL2 on their surface, a potent monocyte and macrophage chemoattractant[40]. Additionally, exosomes promote chemotaxis of cancer cells[41,42], neutrophils via leukotriene B_4[43], and macrophages via sphingosine-1-phosphate[44,45]. Collectively, these studies suggest cancer derived extracellular vesicles confer phenotypic changes to immune cells and are capable of inducing migration. When considering that other features of the TME are affected by EVs as well such as stromal cell differentiation to cancer associated fibroblasts[46,47], interaction with the ECM and ECM remodeling[48–50], and angiogenesis[51,52], it is clear exosomes have the unique potential to modulate the TME and tumor progression.

Although numerous studies have investigated the functional biology of exosomes, experimental constraints often limit the conclusions of these studies. For example, the nomenclature “exosome” refers to vesicles from multivesicular endosomal origins, but experimental isolation techniques (ultracentrifugation, size exclusion chromatography, etc.) distinguish particles based on size not cellular origin. As a result, it is inaccurate to label these vesicles as “exosomes” because there is the possibility that other lipid fragments with disparate origins (e.g. lipoproteins) are also isolated in the process. Thus, the terminology “small extracellular vesicle” (sEV) will be employed for the remainder of this body of work in recognition of MISEV 2018 guidelines[53].

While much work has been dedicated to characterize the functions of sEVs in the TME, much less is known about their physical location and distribution over the course of tumor

progression. For an sEV to have a functional consequence, it must be physically located in an area where it will have an effect. Biodistribution studies following intravenous injection of sEVs have been performed in several animal models including mice and zebrafish[54–59]. These studies generally show sEV clearance via the liver, spleen, and kidney[56,59,60], but also demonstrate targeting of specific tissues due to relevant receptors expressed on sEVs. Collection of sEVs often occurs in the lungs[54,56,60], and macrophages have been shown to uptake sEVs from the circulation[55,58,61]. While these biodistribution studies offer insights into systemic distributions of sEVs, fewer studies have considered the spatial distribution of sEVs within a tumor microenvironment. Understanding sEV interstitial distribution is necessary to uncover the dynamic effect sEV may play in shaping the TME.

Like other soluble mediators, sEVs are transported by a combination of two modes of transport: 1) diffusion; and 2) forced convection (advection). Diffusion is described as the passive, random motion of particles due to internal energy resulting in net particle movement from high concentration to low. Fick's first law of diffusion captures the relationship between particle diffusivity and net diffusive flux:

$$J = -D\nabla C \qquad Eq.1$$

where J [$\frac{mol}{s*m^2}$] is diffusive flux, D [$\frac{m^2}{s}$] is the molecular diffusion coefficient or diffusivity, and ∇C [$\frac{mol}{m^4}$] is the spatial concentration gradient of the diffusing species. This expression conveys that the diffusive flux of a species is proportional to (and in the opposite direction) of a spatial concentration gradient. The coefficient of proportionality is the diffusivity. Diffusivity is inversely proportional to solute radius and acts more quickly over shorter versus longer distances. Diffusion therefore dominates the transport of small molecules such as oxygen across the epithelial barrier in the lungs and glucose inside of a cell.

As soluble mediators become larger, the effect of diffusion become less dominant relative to convective transport. Forced convection, or advection, is the bulk movement of a species within

a fluid due to fluid flow from an applied force such as pressure. The concentration change of a species over time is described by:

$$\frac{\partial c}{\partial t} = -\nabla * (vc) \qquad Eq.2$$

where $\frac{\partial c}{\partial t}$ [$\frac{mol}{l*s}$] is the concentration change of a species over time, v [$\frac{m}{s}$] is fluid velocity, and c [$\frac{mol}{l*m}$] is the spatial concentration of the species. Convective transport generally dominates solute transport with increasing fluid flow and over longer distances. For example, while diffusive transport dominates oxygen flow in the alveolar region, in the trachea during inhalation or exhalation, convective transport dominates oxygen transport due to the rapid fluid flow (~200 ml/sec) and longer characteristic lengths. A dimensionless relationship between convection and diffusion, termed the Peclet number (Pe), is often applied as a simple index to compare these two modes of transport:

$$Pe = \frac{lv}{D} \qquad Eq.3$$

where l [m] is the characteristic length over which the particle is being transported, v [$\frac{m}{s}$] is flow velocity, and D [$\frac{m^2}{s}$] is diffusivity or the diffusion coefficient. Pe represents the ratio of the rate of convection to diffusive transport. Transport where Pe=1 is considered to be affected equally by both diffusion and convection while conditions when Pe<<1 is considered diffusion dominant and Pe>>1 convection dominant. From this relationship it is clear that not only particle size and flow velocity impact Pe; the characteristic length is a crucial component as well and explains why transport over shorter distances is more susceptible to diffusion as the dominant transport mode.

The interstitial space broadly describes the tissue microenvironment between the blood and lymphatic microvasculature. This environment varies considerably between different organ systems in the body and between normal and pathologic tissue such as a developing tumor. Although this microenvironment surrounds the vasculature, a small amount of fluid exits the capillary bed (due to osmotic and hydrostatic pressure differences) and is reabsorbed by the

lymphatics. This fluid flow is termed interstitial flow, and is present in essentially all tissues[62]. Interstitial flow is a fundamental feature of the TME that affects cell phenotype through mechanical forces[63,64] as well as mediating cell-cell signaling by transporting cytokines and chemokines[64,65]. Interstitial flow is dynamic, and not only varies depending on tissue function and location, but also the pathophysiological state of the tissue[66]. In most healthy tissues, fluid flow velocity generally ranges between 0.1-1 μm/s but can reach as high as 10 μm/s in cases of acute edema or inflammation in the TME[67,68].

The flow of fluid through the interstitium is governed by the properties of the fluid (similar to blood plasma, and comparable with some deviations, throughout the body), but more importantly the pressure difference driving flow and the properties of the interstitial tissue to inhibit flow[66]. The components of the ECM (e.g. types of extracellular matrix proteins-collagens, laminins, proteoglycans; fiber organization-fibrillar, layered; fiber orientation-orthogonal or parallel to flow) and cell populations residing within this 3D matrix contribute to a fluid's ability to pass through the matrix[22,66,69]. Characteristics such as porosity, tortuosity, and void volume (among others) all dictate how fluid may flow in the interstitium. Darcy's law, which was derived in the 1800's to describe fluid transport through a porous gravel bed, is commonly used to approximate interstitial volumetric flow rate and flow velocity[67]:

$$\frac{Q}{A} = \frac{-K'\Delta P}{\Delta x} \qquad Eq.4$$

where Q [$\frac{m^3}{\mathrm{s}}$] is bulk volumetric flowrate, A [m^2] is the cross-sectional area for flow, K' [$\frac{\mathrm{m}^4}{\mathrm{s}*\mathrm{dyne}}$] is hydraulic conductivity, ∇P [$\frac{dyne}{\mathrm{m}^2}$] is the pressure difference driving bulk flow, and Δx [m] is the distance of transport. K' captures features of the interstitium such as void volume and tortuosity. Typical interstitial distances, unsurprisingly, vary among tissue types but are generally on the order of 100-200 μm[68].

Given the characteristic interstitial distance of 100-200 μm and the relatively large size of sEVs compared to soluble molecules, it is clear that convection may play a principal role in sEV interstitial transport. Transport is integral to sEV function. For an exosome derived from a cancerous cell (or any cell in the interstitial space) to reach the circulation, it must be secreted by the parent cell, navigate the interstitial space including the extracellular matrix, and cross an endothelial barrier (either post-capillary venule or lymphatics). This path is complex, yet few studies have considered how a tumor-derived sEV may reach the circulation. Significantly, if sEV transport is impaired compared to bulk flow (e.g. binding to the extracellular matrix in the interstitial space), the resulting accumulation could impact concentration and spatial distribution, and thus have fundamental consequences for the developing TME.

sEVs have been shown to colocalize with ECM in a variety of different *in vitro* and *in vivo* model systems. Colocalization with matrix has been proposed to occur either through physical containment due to small pore sizes relative to EV diameters and/or active binding via adhesion molecules present on the surface of EV populations. The effects of pore size, matrix mechanical properties, and resulting sEV transport by diffusion was recently described by Lenzini *et al*., where sEVs were shown to be transported through nanoporous ECM despite having diameters larger than the ECM mesh size[70]. Diffusion was facilitated by stress relaxing properties of the ECM as well as sEV deformation due to presence of membrane bound aquaporins. This study builds off of the work from other groups which have demonstrated sEVs are resident constituents of the ECM[33,71], and can influence ECM architecture and structure through aggrecanases, matrix metalloproteinases, elastase, and likely other matrix digesting proteases[49,72–74].

sEV binding to ECM also occurs through receptor-ligand pairs on sEVs and ECM[54,75]. Binding is mediated through adhesion molecules such as integrins (α2β1, α6β1, αvβ5, α6β4), CD44, or surface-bound glycocalyx and glycan binding proteins among others[73,75,76]. This finding is supported by the relatively high expression of adhesion molecules on cancer derived EVs[77]. Further, several proteomics studies have demonstrated increasing presence of relevant integrins

on sEVs from increasingly malignant parent epithelium, including integrins α3, α6, and β1[78,79]. Studies have shown sEV binding to a variety of extracellular matrices including collagen, laminin, and fibronectin[49,71,75,80]. Once confined to the ECM, sEVs can interact with resident cells as well as the native ECM, and serve as consequential mediators in a developing TME[48].

Although binding to matrix is a property of sEVs, quantitative binding parameters such as on rates (K_{on}), off rates (K_{off}), and dissociation constants (K_d) remain largely uncharacterized. In addition, the transport of sEVs in the interstitium by convection and how binding to the matrix impacts the rate of transport and concentration (both bound and unbound/free) has not been described. Finally, sub-populations of sEVs capable of binding matrix have been identified[71], but it is still unknown how these EVs are transported within the TME. Even less is known about how dynamic sEV transport evolves over the course of cancer malignancy. Due to the unique transport features of EVs, their extensive influence in disparate processes of tumor progression, and the fundamental need to improve the understanding of the TME, the **primary goal** of this thesis work is to characterize interstitial sEV transport in the context of breast cancer progression.

Hypothesis and Study Strategy

We hypothesized that sEVs are transported predominantly by convection through the interstitium where accumulation and the formation of a spatial gradient occurs via sEV binding to laminin through integrins α3β1 and α6β1 expressed on sEVs. Further, we hypothesized transport is altered over the course of malignant progression, with sEVs from more malignant parent cells accumulating to higher concentrations and forming steeper bound gradients in the interstitium due to the increased presence of laminin binding integrins on those sEVs. This hypothesis arose from the observation that integrin expression on breast epithelial cells, such as integrins α3 and α6[81–83], increased with malignant progression. Since sEVs often contain many of the same

proteins as parent cells, we questioned the functional consequence of what would occur *if* sEVs also contained increasing levels of laminin binding integrins.

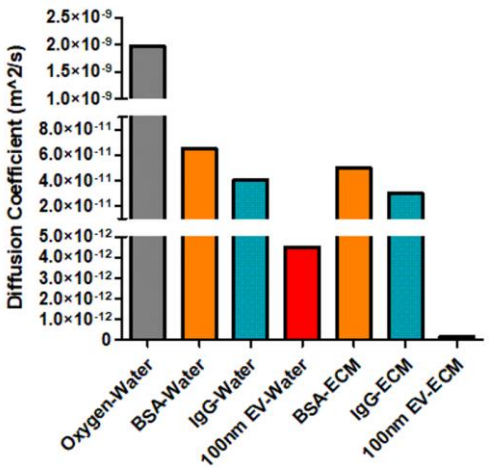

Figure 1. Sample diffusion coefficients of common small molecules soluble mediators and sEVs in water and ECM.

Due to the size of sEVs compared to standard small molecule transport (20-50x larger hydrodynamic diameter than small molecules) and published[70] preliminary diffusion coefficients roughly 3 orders or magnitude slower than small molecules (**Fig. 1**), we hypothesized that convective flow would dominate sEV transport. The consequences of convective flow coupled with the idea of binding through integrins, resulted in the unified concept that sEVs have the potential to accumulate in the interstitial space and form a gradient with high concentration at the tumor source and low concentration at the post-capillary venule or lymphatic sink (**Fig. 2**). Significantly, this would present a novel mechanisms of: 1) generating interstitial cytokine/chemokine gradients compared to traditionally small molecule soluble mediators which rely on diffusion to establish gradients[63] which could guide cell migration; and/or 2) alter the concentration of mediators in the interstitium which could impact the phenotype of resident cells.

To address our primary goal and hypotheses, the study strategy was carefully designed to include a model cell line of breast cancer progression, the MCF10 series, from which EVs would be isolated and their transport assessed in a microfluidic platform capable of precise fluid flow control and dynamic visualization of sEVs.

The MCF10A series (MCF10A, normal; MCF10DCIS, pre-malignant; MCF10CA1, malignant) was derived from the MCF10M mortal, breast epithelial cell isolated from benign tissue from a patient with fibrocystic disease. From the MCF10M, the spontaneously immortalized MCF10A lines was generated, and is regarded as an immortalized but otherwise normal breast

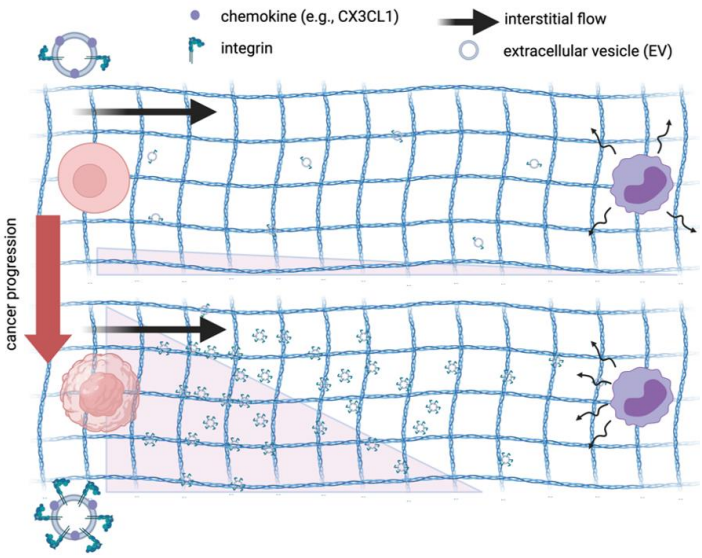

Figure 2. Graphical abstract. During malignant progression, secreted sEV profiles possess higher levels of surface bound laminin-binding integrins. Due to convective interstitial flow, sEVs are transported through the interstitial space where they may bind laminin through integrins α3β1 and α6β1. Due to higher levels of integrins, sEVs from malignant parent cells will bind the matrix with higher avidity resulting in higher accumulation of sEVs as well as the formation of a bound gradient. Accumulated sEVs and bound gradient may induce phenotypic response including cell migration from tissue resident immune cells.

epithelial cell[84]. From the MCF10A line, the MCF10AT1 line was generated via transduction of the constitutively active HRAS oncogene which resulted in pre-malignant neoplasms when injected into immunodeficient mice[85]. From the MCF10AT1 line, serial passaging into immunodeficient mice selected for increasingly invasive phenotype including the MCF10DCIS.com (henceforth referred to as “MCF10DCIS”) line which forms ductal carcinoma in situ (DCIS) like growths when injected into immunodeficient mice as well as the fully malignant MCF10CA1 line[86,87]. The MCF10 series is triple negative (ER-, PR-, HER2-), wild type P53, and is molecularly classified as basal b[88]. This progression series is widely used in both *in vitro* and *in vivo* studies of breast cancer[89–92], including several studies assessing sEVs isolated from these parent cells[79,93–95]. By isolating sEVs from each of these MCF10 lines, we have a well-defined model system to enhance our understanding of sEV transport dynamics at discrete stages of breast cancer malignant progression.

The breast basement and interstitial ECM is comprised predominantly of collagens, but is also rich in laminins, fibronectin, entactin, and many other ECM proteins[96,97]. Due to the likely presence of integrins α3, α6, and β1 on sEVs isolated from the MCF10 series, sEV transport through a laminin-rich ECM was selected to assess α3β1 and α6β1 binding to laminin. While other extracellular proteins such as collagens, entactin, and the heparin sulfate proteoglycan perlecan

are present in the laminin-rich ECM selected (Matrigel), laminin constitutes 60% of the protein fraction[98]. To ensure binding effects were specific to laminin via integrins α3β1 and α6β1, initial studies assessed the presence of collagen binding integrins α1β1 and α2β1 on MCF10 series sEVs. Further, laminin-rich ECM is ubiquitously used for *in vitro* and *in vivo* studies related to the breast cancer field[98], and would serve as an adequate starting point for these studies.

A microfluidic platform was selected to address the key considerations in these studies. The selected microfluidic device was previously used to demonstrate that interstitial flow velocity rapidly removes soluble mediator gradients, and provides the ability to establish well-defined fluid flow profiles[63]. This microfluidic approach offers the ability to probe 3D sEV transport through a laminin rich ECM while retaining the ability to control fluid flows and monitor dynamic spatiotemporal processes. For the questions proposed in this study, a microfluidic organ-on-chip device is the appropriate tool to draw meaningful scientific conclusions. Organ-on-chip devices are uniquely situated to address biological questions concerning dynamic cell-cell interactions on the scale of a few hundred micrometers. Although they are limited in terms of recapitulating the full scope of *in vivo* complexity, numerous studies utilize these devices to address questions in cancer biology[99–102]. By using a microfluidic organ-on-chip system we will address a previously unexplored set of questions that will improve the understanding of sEV biology and their potential role in the developing TME.

The results of this study add to the growing body of evidence that sEVs are capable of interacting with laminin, a common extracellular matrix protein enriched in the breast tumor microenvironment. Individual sEV analysis techniques such as ExoView demonstrate evidence of integrin colocalization on single sEVs as well as the percent of sEVs that are capable of binding ECM through integrin/matrix interactions. Diffusion experiments using fluorescence recovery after photobleaching (FRAP) provide the first kinetic binding parameters between bulk sEVs and a laminin-rich ECM (Matrigel), and demonstrates the changes in diffusive sEV transport with changes in breast cancer parent-line malignancy. *In silico* computational models iteratively built

using parameters found in *in vitro* experiments demonstrates the feasibility of sEV accumulation in the interstitial space as well as the formation of a transient sEV concentration gradient, high in concentration by the tumor source with decreasing concentration towards a blood-vessel sink. Subsequent, *in vitro* microfluidic device convective flow experiments validate key takeaways from the computational model and demonstrate enhanced sEV bound concentrations and the formation of a spatial gradients via integrin binding. Finally, preliminary experiments with a significant immune cell population in breast cancer progression, the monocyte and macrophage, demonstrate a phenotypic response towards sEVs through migration and provide the foundation for future studies to investigate the functional consequence of interstitial sEV concentration and spatial distribution.

Chapter 2: Materials and Methods

Cell culture

The MCF10 breast cancer progression series (MCF10A, normal; MCF10DCIS, pre-malignant; MCF10CA1, malignant) was purchased from Karmanos Cancer Center, and sub-cultured according to advised protocols. Culture medium for MCF10A cells consisted of DMEM/F12 (Thermo Fisher Scientific), supplemented with 5% horse serum (Thermo Fisher Scientific), 500 mM $CaCl_2$ (Sigma-Aldrich), 20 ng/ml EGF (Thermo Fisher Scientific), 105 ng/ml cholera toxin (Millipore Sigma), 10 µg/ml insulin (Sigma), 0.5 µg/ml hydrocortisone (StemCell Technology). MCF10DCIS and MCF10CA1 culture medium consisted of DMEM/F12 supplemented with 5% horse serum and 500 mM $CaCl_2$.

THP-1 human monocytes (TIB-202, ATCC) were subcultured in RPMI 1640 (Thermo Fisher Scientific) supplemented with 10% HI FBS (Thermo Fisher Scientific) and 0.05 mM beta-mercaptoethanol (Thermo Fisher Scientific) according to manufacturer protocols. Subculture cell densities were maintained between 250,000 and 1,000,000 cells/ml.

sEV Isolation

To prepare sEV-depleted serum for culture media, serum-depleted horse serum was prepared by serial centrifugation. Serum was centrifuged for 300xg for 10 minutes at 4°C to remove live cells and large debris, 2,000xg for 15 minutes at 4°C to remove dead cells and apoptotic bodies, 10,000xg for 30 minutes at 4°C to remove larger microvesicles, and finally spun via ultracentrifugation overnight at 120,000xg at 4°C. Absence of serum sEVs was validated via nanoparticle tracking analysis (NTA) with the NanoSight LM10 (Malvern Panalytical Ltd.).

To isolate MCF10 series sEVs, MCF10A, MCF10DCIS, and MCF10CA1 cells were loaded into 3 T-150 flasks each at a starting confluency of approximately 15% ($1.5x10^6$ MCF10A cells, $1.5x10^6$ MCF10DCIS cells, $2x10^6$ MCF10CA1 cells) and cultured for 24 hours in non-EV depleted

media. Following 24-hour culture, flasks were triple rinsed with ample PBS + 1mM $CaCl_2$ and 1 mM $MgCl_2$ (Thermo Fisher Scientific) to remove horse serum-derived sEVs. 15ml of EV-depleted serum media was added to each flask and cells were cultured for 72 hours. Final cell concentration was observed following 72-hour culture and was between 80-95% confluent. Initial seeding was optimized to prevent 100% confluence over the course of the 4-day culture.

Conditioned media was collected and subjected to increasing centrifugation spins to remove live cells (300xg for 10 minutes at 4°C), dead cells and apoptotic bodies (2,000xg for 15 minutes at 4°C), and larger microvesicles (10,000xg for 30 minutes at 4°C). 150,000 kDa Amicon filters (Millipore Sigma) were loaded with 15ml of pre-spun conditioned media and spun at 4,000xg for 45 minutes according to manufacturer protocols for crude EV purification. The EV-retentate was collected and filters were washed with MilliQ water. sEVs for downstream imaging analysis were stained with 2 mM CellTrace Far Red (Thermo Fisher Scientific) and incubated for 2 hours at 37°C [103].

Following incubation with CellTrace Far Red (CTFR), sEVs were separated from excess dye as well as free proteins via size exclusion chromatography (SEC). An Izon Automatic Fraction Collector and $qEV_{Original}$ 35 nm SEC columns (Izon) were loaded with 1 ml of concentrated EV stock. EV-rich fractions one through four were collected (0.5 ml each) and utilized for downstream experiments, while fractions five through twelve were collected to serve as EV-free controls.

Nanoparticle tracking analysis (NTA)

sEV samples were diluted 1:250 in 0.22 μm filtered MilliQ water, and 1 ml samples were added to a NanoSight LM10 (Malvern Panalytical Ltd) to characterize sEV size and concentration. An automated syringe pump (Harvard Bioscience) provided consistent flow of sEV samples across the field of view to provide multiple measurements. 3 x 30s videos were acquired per sample, and NanoSight NTA 3.1 software was utilized for analysis.

Transmission electron microscopy (TEM)

sEVs were fixed in 1% glutaraldehyde for 5 minutes. A 10 µL droplet of EV/ glutaraldehyde mix was placed on parafilm and a copper formvar grid was floated, copper side down, on the droplet for 40 minutes. The grid was then dried on filter paper, moved to a 100 µL droplet of MilliQ water to wash, dried again, and moved to a 50 µL droplet of 0.2 um filtered 4% uranyl acetate for 8 minutes. Grids were then dried again on filter paper and allowed to air dry for at least 10 minutes before imaging. Grids were imaged on a Talos FEI L120C TEM (Thermo Fisher Scientific) from 11,000x to 36,000x magnification.

Western blot

MCF10 series conditioned media was prepared as described and centrifuged at 300xg for 10 min to pellet cells. Supernatant was transferred to a new tube and centrifuged at 2,000xg for 15 min to remove dead cells. Supernatant was transferred to a new tube and centrifuged at 10,000xg for 30 min to remove microvesicles and cell debris. Supernatant was transferred to a new tube, and diluted if necessary in 0.22 µm filtered PBS and ultracentrifuged at 120,000xg for 70 min to pellet EVs. Free protein containing supernatant was discarded, the pellet was resuspended in filtered PBS and ultracentrifuged at 120,000xg for 70 min. Supernatant was again discarded, the pellet was resuspended in roughly 300 µL of PBS, and frozen in aliquots.

EV pellets were lysed in RIPA lysis buffer (Millipore) containing protease inhibitor cocktail (Roche) according to manufacturer instructions. For EV fractions, maximal volume of protein per lane (39 µL) was loaded. Proteins were loaded on an 8-16% graded Tris-Glycine polyacrylamide gel and transferred to a 0.2µm PVDF membrane (Life Technologies). Membranes were blocked in 5% milk in phosphate-buffered saline with Tween-20 (TBST) at 0.05% for one hour at room temperature with rocking, and then incubated with primary antibody in blocking buffer at 4˚C overnight. Antibodies against CD9 were used at 1:1000 dilution (BioLegend), β-1 integrin at

1:1000 (Cell Signaling), α3 integrin at 1:1000 (Abcam), α6 integrin at 1:1000 (Cell Signaling). Secondary antibody mouse IgGκ-HRP (Santa Cruz Biotechnology) or anti rabbit IgG HRP (Cell Signaling) were diluted at 1:5000 in block buffer and incubated at 1 hour at room temperature with rocking. Proteins were visualized with Supersignal West Pico PLUS chemiluminescent substrate (Thermo Fisher) using a FluorChem E (Protein Simple).

Single sEV protein characterization-ExoView

An ExoView R100 (NanoView Biosciences) was utilized for individual sEV immunofluorescent analysis. sEVs were diluted to an initial concentration between 6.66E6-1.32E7 sEV/ml, and diluted 1:1 with incubation solution (NanoView Biosciences) according to manufacturer protocols. sEV solutions were loaded onto EV-TETRA-C ExoView Kits (NanoView Biosciences) and prepared via an ExoView CW100 Chips washer (NanoView Biosciences). Fluorescently conjugated integrin antibodies (1:400 AF488 anti-integrin β1, clone-TS2/16, BioLegend; 1:200 PE anti-integrin β1, clone-TS2/16, BioLegend; 1:400 AF647 anti-integrin β1, clone-TS2/16, BioLegend; 1:400 PE anti-integrin α3, clone-ASC-1, BioLegend; 1:400 AF488 anti-integrin α6, clone-GoH3; BioLegend) anti-chemokine antibodies (5 µg/ml APC anti-CX3CL1, clone-51637, R&D Systems), and ExoView tetraspanin kit antibodies (1:500 AF647 anti-CD63, clone-H5C6; 1:500 AF555 anti-CD81, clone-JS 81; 1:500 AF488 anti-CD9, clone-HI9a) were added at the appropriate steps during the incubation procedure. MIgG thresholds were selected at approximately the 75th percentile to reject the majority of non-specific binding. sEV counts and integrin or tetraspanin colocalization was normalized to MIgG counts.

The microfluidic platform

The microfluidic device leveraged for diffusion, convection, and *in silico* experiments was previously developed in the lab[63]. This device consists of three tissue chambers (chambers 2-4)

and two microfluidic lines running parallel to each other (chambers 1, 5) (**Fig. 10**; **Fig. 24a**; **Fig. 27**). Microfluidic devices were fabricated with via soft-lithography with polydimethylsiloxane (PDMS). PDMS which was prepared by mixing Sylgard^{TM} 184 silicone elastomer base and curing agent in a 10:1 ratio (Dow Corning) and pouring over SU-8 master molds. Cast-PDMS devices were bonded to glass coverslips (Thermo Fisher Scientific) via plasma treatment (Harrick Plasma).

200 µl pipette tips (Genesee Scientific) were added to fluidic ports at the end of chambers 1, 3, and 5, and filled with varying fluid volumes to establish controlled hydrostatic pressure heads. Differences in hydrostatic pressure head heights were leveraged to drive convective flow in *in silico* and *in vitro* convective flow experiments. Communication between chambers was established by structural micropores, the geometries of which were previously optimized to avoid leakage of gels into neighboring chambers while also providing air-bubble free gel/fluid interfaces (pore width=30 µm; pore length=550 µm). The devices were designed with the same number of communication pores between the tissue chambers and the fluidic lines to facilitate formation of near linear concentration and pressure gradients across the length of the tissue chambers[63].

In vitro diffusion experiments

To assess diffusion of Fluoro-Max 100 nm polystyrene red fluorescent beads (Thermo Scientific) and CTFR stained MCF10 series sEVs, beads diluted to a final concentration of 1:3000 or 1E9 sEVs were incubated with .1% TWEEN-20 (Sigma-Aldrich) or 1 mg/ml BSA (Thermo Scientific) respectively for 15 minutes at 4°C to block nonspecific binding interactions. sEVs were then incubated with a working solution of either 0.1 mM $CaCl_2$ and 1 mM $MgCl_2$, 1 mM MnCl2, 0.1 mM $CaCl_2$ and 1 mM $MgCl_2$ (all from Sigma-Aldrich) with a cocktail of functionally inhibitory integrin blocking antibodies (20 µg/ml anti-α3, clone-ASC-6, Millipore Sigma; 20 µg/ml anti-α6, clone-GoH3, Thermo Fisher Scientific; 50 µg/ml anti-β1, clone-mAb13, Millipore Sigma; 20 µg/ml anti-

β4, clone-ASC-6, Millipore Sigma), or 1 mM $MnCl_2$ with the cocktail of functionally inhibitory integrin blocking antibodies. Bead or sEV solutions were then mixed with laminin-rich ECM (Matrigel-GF Reduced; Corning) for a final laminin-rich ECM working concentration of 3 mg/ml, and loaded in chambers 2 and 4 (**Fig. 10**). Laminin-rich ECM was left to polymerize for 30 min at 37°C before particle tracking or FRAP imaging. Care was taken to prevent bulk convective fluid flow by ensuring loading heads were roughly equivalent, incubating for an additional 15 minutes at room temperature to allow time for fluid height equilibration, and leaving other device chambers devoid of fluid.

Particle tracking

For particle tracking analysis, bead and/or sEV loaded devices were imaged with an Olympus FV3000 laser scanning confocal microscope (Olympus) via a 60x objective oil immersion lens and captured by high sensitivity-spectral detectors. Images were acquired every 440 ms for one minute. Resulting image stacks were analyzed in FIJI with the Mosaic plugin[104] using the following optimized settings: Radius: 1, Cutoff: 0.001, Per/Abs: 0.7, Link Range: 1, Displacement: 5, Dynamics: Brownian. Particle tracks and resulting diffusion coefficients were calculated in the plugin via mean square displacement. To delineate bound, partially bound, and freely diffusing sEVs, 60 qualitatively similar tracks across all experimental conditions were selected for each transport mode. D_{eff} values were averaged to find ranges for each transport mode: Bound range: $D_{eff} \leq$7.25E-14 m^2/s ; Partially bound: 7.25E-14 $m^2/s < D_{eff} <$3.88E-13 m^2/s ; Freely diffusing: $D_{eff} \geq$3.88E-13 m^2/s. Bound percentages of MCF10 series sEVs were assessed by dividing bound tracks by total particle tracks.

Fluorescence recovery after photobleaching (FRAP) imaging

FRAP was performed on an Olympus FV3000 laser scanning confocal microscope (Olympus) via a 20x objective with 3x digital zoom and captured by high sensitivity-spectral detector. FRAP images were acquired every 240 ms over the course of 5 minutes with a 100% laser excitation pulse after the first four frames to generate a circular 18 μm diameter bleach spot. Laser power was tuned to ensure that the final non-bleached background fluorescence was within 15% of the initial non-bleached background fluorescence on average.

FRAP analysis

The underlying second-order kinetic equation describing sEV interactions with the ECM can be described by:

$$sEV + B \underset{K_{off}}{\overset{K_{on}}{\rightleftarrows}} sEVB \qquad Eq.5$$

where sEV is the concentration of free sEVs, B is the concentration of binding sites within the matrix, and sEVB is the concentration of matrix-bound sEVs. Initial concentrations of each species as well as forward (K_{on}) and reverse (K_{off}) rate constants determine final steady state concentrations of each species.

Raw FRAP data was analyzed in FIJI using a standard analysis pipeline. In brief, the "create profile" plugin[105] was implemented to generate average fluorescent intensity spectrum curves over the full image stack. ROIs were generated for the bleach spot as well as a control ROI for the background fluorescence. The bleach spot fluorescent spectrum was normalized to a function fit to the background fluorescence ROI to control for photobleaching. Spectrum data was exported to MATLAB for further analysis. To perform fits, background-normalized spectrum data was normalized to fall within 0 and 1 by setting the maximum value pre-bleach equal to 1 and the minimum value post-bleach equal to 0. A progressive sliding window was utilized to average

timepoints in order to smooth the curves and to prevent biased overfitting of later timepoints[106]. Sliding window conditions were as follows: T=0-0.72s (Pre-bleach) - no averaging; T=0.96-29.76s – averaged 2 points; T=30.76-44.4s – averaged 5 points; T=46.8-58.8s – averaged 10 points; T=62.4-66s – averaged 15 points; T=70.8-299.76s – averaged 20 points. Log space parameter arrays with 50 values were generated to screen the three fitting parameters: D_{eff} (1E-13->1E-11), K_{on} (1E-7->1E-2), and K_{off} (1E-7->1E-2).

FRAP curve fitting procedures followed the general methodology outlined in Sprague *et al.* [106], to fit experimental data with second order kinetics (Eq. 5). The following fitting equation[106] was applied to fit experimental FRAP recovery curves:

$$\overline{frap}(p) = \frac{1}{p} - \frac{F_{eq}}{p}(1 - 2K_1(qw)I_1(qw)) * \left(1 + \frac{K_{on}^*}{p + K_{off}}\right) - \left(\frac{C_{eq}}{p + K_{off}}\right) \qquad Eq.6$$

where,

$$K_{on}^* = K_{on} * B_{eq} \qquad Eq.7$$

$$F_{eq} = \frac{K_{off}}{K_{on}^* + K_{off}} \qquad Eq.8$$

$$C_{eq} = \frac{K_{on}^*}{K_{on}^* + K_{off}} \qquad Eq.9$$

$$q = \sqrt{\left(\frac{p}{D_f}\right) * (1 + \frac{K_{on}^*}{p + K_{off}})} \qquad Eq.10$$

where $\overline{frap}(p)$ is the average of the Laplace transform of the fluorescent intensity within the bleach spot, p is the Laplace variable that inverts to yield time, I_1 and K_1 are modified Bessel functions of the first and second kind respectively, w is the bleach spot radius, B_{eq} is the equilibrium concentration of binding sites, and D_f is the sEV free diffusion coefficient. The numerical inversion of this function was performed via the "invlap.m" routine[107]. A matrix of 50x50x50 curve libraries was generated by importing each combination of D_f, K_{on}, and K_{off} fitting parameters. A sum of squares approach was applied to minimize the error between library curves and experimental data. Preliminary best-fit parameters were extracted from the best fit curve.

To refine the fitting procedure, the MATLAB routine “fitnlm”, was applied for higher accuracy fitting of K_{on} and K_{off}. D_f was constrained to the value determined through the first sum of squares residual estimation to reduce the burden on the fitting process and risk of overfitting the data. The “fitnlm” routine used the Levenberg-Marquardt nonlinear least squares algorithm. Resulting refined-fit parameters for K_{on} and K_{off} are presented in results, although the difference between the initial sum of squares fit and the refined fit were negligible.

Finite element simulations

Computational finite element simulations were performed using COMSOL Multiphysics™ 5.2a software. The convection–diffusion equations of mass and momentum transport were solved to find flow velocities and spatial concentration profiles of sEVs, binding sites, and bound sEVs. The Free and Porous Media Flow module was used to model fluid through the porous ECM, and Transport of Diluted Species Modules were implemented to track transport of each species. Chemistry modules were added to capture the relationship between sEVs and binding sites (Eq. 5). 2D solutions were generated assuming incompressible, single-phase, laminar flow with no-slip boundary conditions applied to all surfaces with the exception of terminal port inlets and outlets (ends of chambers 1-5). sEVs were modeled as a dilute, dissolved species which neglected physiologic drag and interactions with matrix porosity. Binding sites and bound sEVs were modeled as effectively immobile with D_{eff}= 1E-16 m^2/s. Baseline modeling parameters (**Table 2**) were used unless otherwise specified. Additional parameter values were: dynamic viscosity of water at 25°C = 0.89 cP; density of water at 25°C = 1000 kg/m3; porosity of matrix = 0.99 %. Various parameter and time sweeps were performed, and parameter values were tested iteratively along with *in vitro* experiments.

In vitro microfluidic device convective flow experiments

Identical microfluidic devices as those used in FRAP and particle tracking experiments were utilized for convective flow experiments (**Fig. 27**). CTFR-stained sEVs were prepared as described above, but were not embedded in laminin-rich ECM. Rather, laminin-rich ECM was prepared at 3 mg/ml and loaded into chambers 2 and 4 (**Fig. 27**). Following a 30 minute incubation at 37°C, warmed PBS was added to chambers 1, 3, and 5 to establish hydrostatic pressure heads and convective flow from chamber 3 outwards across the matrix-filled chambers 2 and 4 towards fluidic chambers 1 and 5. To initiate fluid flow for convective flow experiments the following fluid volumes were added to 200µl pipette tips to establish hydrostatic pressure heads: Chamber 1: Inlet-15 µl, Outlet-10 µl ; Chamber 2: filled with laminin-rich ECM, no additional pressure head was applied ; Chamber 3: Inlet-35 µl, Outlet-30 µl ; Chamber 4: filled with laminin-rich ECM, no additional pressure head was applied ; Chamber 5: Inlet-15 µl, Outlet-10 µl. Pressure heads were selected to ensure symmetry from the middle of chamber 3 outwards to fluidic chambers 1 and 5.

40 kDa FITC dextran (Sigma-Aldrich) was added to sEV solutions to serve as a control for fluid flow. sEV and dextran flows were visualized via an Olympus FV3000 confocal microscope (Olympus) with a 10x objective using 647nm and 488nm lasers and captured by high sensitivity-spectral detectors to maximize capture of the sEV fluorescent signal. Dextran velocity was calculated using iterative *in vitro* experiments and finite element modeling. In brief, displacements of dextran fluorescence over time were compared between *in vitro* and computational models. *In silico* parameter sweeps of ECM permeability provided associated interstitial flow velocity values. Curves were generated to plot ECM permeability vs. dextran displacement and interstitial fluid velocity vs. ECM permeability. *In vitro* dextran displacement was plotted along these curves to identify interstitial flow velocity.

To assess sEV convective flow and accumulation in the matrix, the following solutions were added to each device chamber via the same methodology and volumes indicated above:

Chamber 1: PBS ; Chamber 2: filled with laminin-rich ECM ; Chamber 3: 3E9 sEV + 40 kDa dextran + treatment condition + PBS ; Chamber 4: filled with laminin-rich ECM ; Chamber 5: PBS. sEV treatment conditions used the same concentrations of blocking antibodies described in diffusion experiments. 5mM EDTA (Thermo Fisher Scientific) and RPMI 1640 were added for additional treatment conditions. `

Images were acquired at 1.08 second intervals over the first 10 minutes of flow. After 30 minutes of flow, images of the full device were acquired as a terminal endpoint. Data for convective flow experiments was analyzed in FIJI. Fluorescent intensity line profiles were generated to show sEV concentration gradients across laminin-rich ECM chambers. Fluorescent intensity ROIs were generated via built-in FIJI plugins. Multiple ports from each device were measured, but analysis was limited to ports with flow velocities within a binned range: 0.15 μm/sec ≤ v ≤ 0.75μm/sec. Binning was performed to exclude ports with negligible flow as well as those with rapid flow caused by degraded laminin-rich ECM. The majority of ports were within the binned range.

Monocyte migration

Transwell experiments were performed by loading 100,000 CTFR-stained THP-1 monocytes in 200 μl of serum-free RPMI 1640 to the top of 6.5mm, 5μm pore transwell supports (Corning). 1E9 sEVs from each of the MCF10 series lines was added to the bottom of the well plate in EV-depleted RPMI 1640. Devices were incubated for 5 hours and imaged via an Olympus FV3000 confocal microscope (Olympus) with a 10x objective using the 647nm laser. Migration of THP-1 monocytes on the bottom of the well plate were counted in FIJI.

Immunofluorescence

MCF10 series cells were cultured on glass coverslips until 70-85% confluent, and then fixed in 10% formalin. Blocking was performed with 1% BSA overnight at 4°C. Primary staining was performed overnight at 4°C with 1:500 unconjugated polyclonal anti-CX3CL1 (Thermo Fisher Scientific) in .1% BSA. Coverslips were triple rinsed with PBS, and secondary staining was performed for 2 hours at room temperature with 4 µg/ml AF488 goat-anti-rabbit (Thermo Fisher Scientific). Coverslips were triple rinsed with PBS and mounted on glass slides with ProLong™ Gold Antifade Mountant with DAPI (Thermo Fisher Scientific). Imaging was performed on an Olympus FV3000 confocal microscope (Olympus) using a 10X objective.

Statistical analysis and figure generation

The majority of experimental conditions were performed in triplicate at minimum. PRISM 5 was utilized for statistical analysis and generation of graphs. One-way ANOVA tests with a p-value < 0.05 and Tukey-Post hoc tests were employed when comparing three or more conditions, while student T-tests with a p-value < 0.05 were used to show significance when comparing only two conditions. MATLAB was used to generate select graphs for FRAP analysis, and Biorender.com was used for the creation of descriptive figures.

Chapter 3: Characterization of Increasingly Malignant sEVs

sEVs from each line of the MCF10 series were isolated, and concentration assessed through nanoparticle tracking analysis (NTA). Representative graphs demonstrate expected sEV size distributions which were centered near 100nm with the majority of measured particles within the expected range of 50-150nm (**Fig. 3a**). When normalizing by the number of cells in each flask from which the sEVs were isolated, NTA revealed increased secretion of sEVs per cell from the malignant MCF10CA1 line compared to the normal MCF10A with the pre-malignant MCF10DCIS line in between (**Fig. 3b**). This result is consistent with results from other groups, indicating that sEV secretion is often increased in cancerous cells due to signaling dysregulation or microenvironmental factors such as acidic pH or hypoxia[108].

sEV identity was further confirmed with transmission electron microscopy (TEM). Although SEC isolation techniques suffer from reduced yield and concentration compared to ultracentrifugation isolation techniques[53], sEV yields were sufficiently high for TEM membrane coverage (**Fig. 3c**). Particles were principally within the 50-150 nm diameter range, in concordance with NTA data, and many particles exhibited the characteristic cup-shaped morphology caused by dehydration and rupture of hydrated particles during TEM preparation.

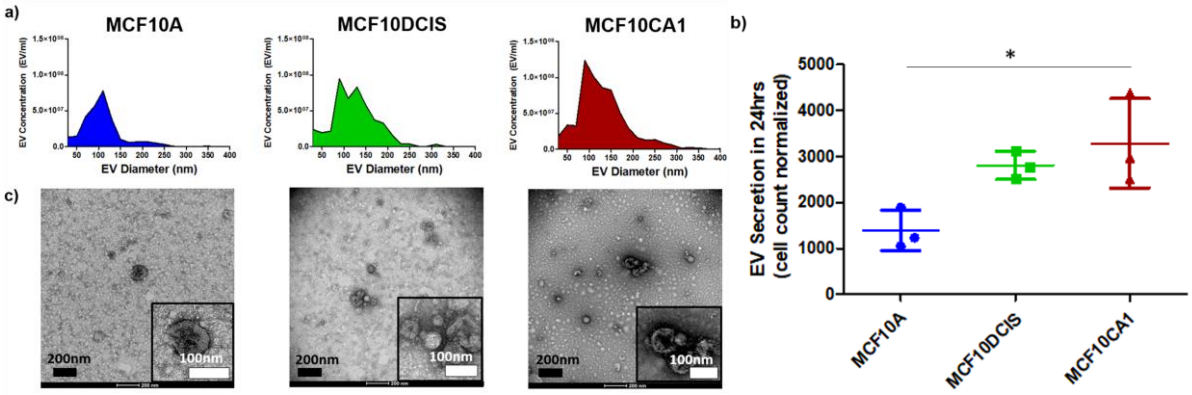

Figure 3. Isolation protocol yields sEVs. a) Nanoparticle tracking analysis (NTA) revealed expected sEV size distribution and adequate concentration for *in vitro* studies as well as b) increasing secretion with malignancy when normalized by cell number. c) Transmission electron microscopy (TEM) demonstrated sufficient sEV concentration and the characteristic cup-shape morphology suggesting successful isolation of exosomes. *p<0.05; One-way Anova, Tukey post-hoc.

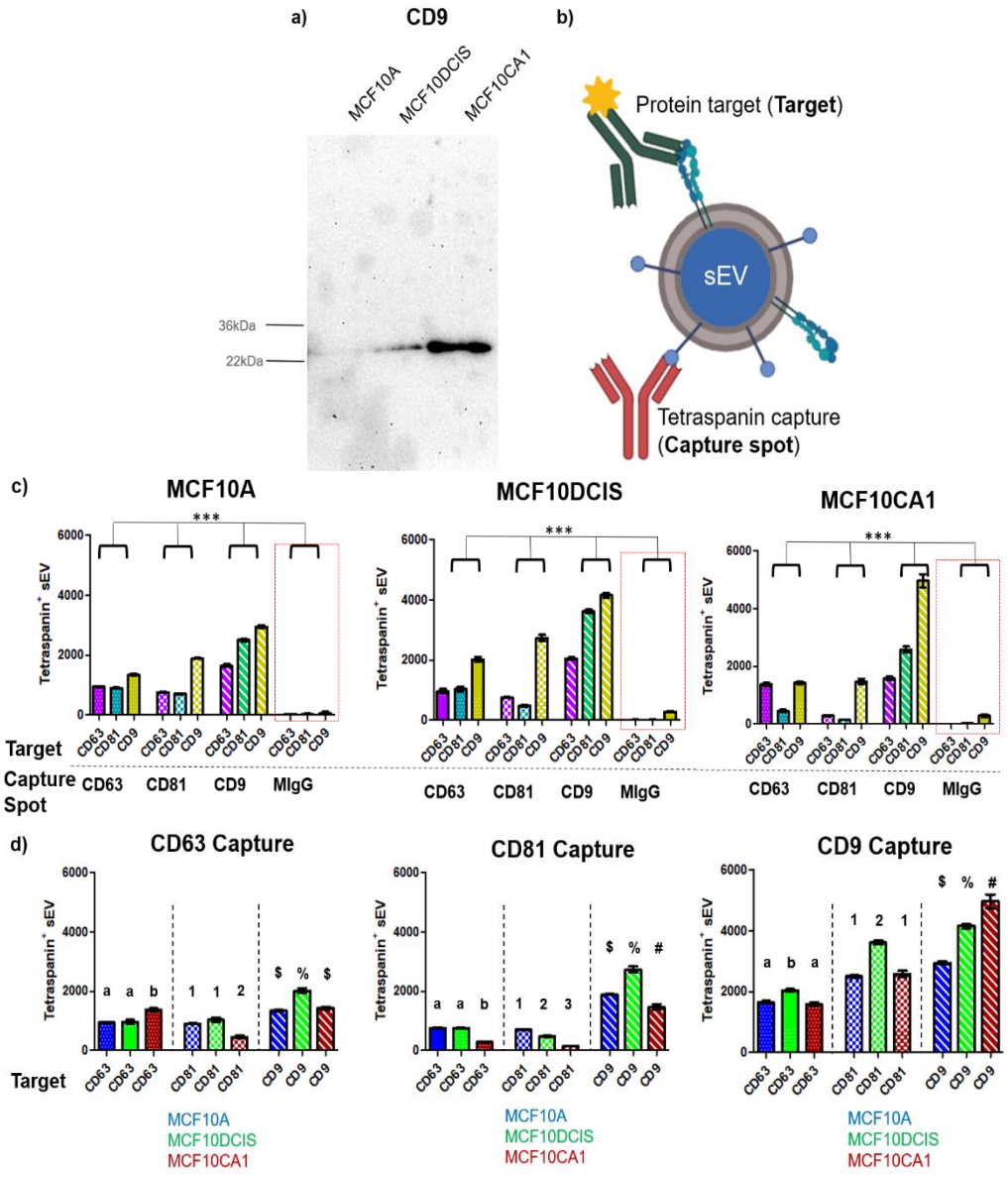

Figure 4. Isolated sEVs possess appropriate tetraspanin markers. a) MCF10DCIS and MCF10CA1 sEVs assessed by western blot reveal bulk expression of tetraspanin CD9. Weak banding was observed from MCF10A sEVs. b) Graphical representation of ExoView methodology demonstrates immobilized tetraspanin capture antibodies bind sample sEVs. Probing with an additional fluorescently conjugated primary antibody permits evaluation of protein presence at the single sEV resolution. c) ExoView analyses revealed CD63, CD81, and CD9 tetraspanin presence on sEVs isolated from each of the MCF10 series lines when compared to negative MIgG capture antibody control (red boxed). ***p<0.001; One-way Anova, Tukey post-hoc. d) Comparing tetraspanin targets across the MCF10 series reveals differential presence of each tetraspanin, further highlighting sEV heterogeneity. Letters, numbers, and symbols above data denote groups within graphs that can be compared. Differences in symbol denotes statistical significance. p<0.05 (stronger significance between some conditions); One-way Anova, Tukey post-hoc.

Evidence of these “popped” vesicles is indicative of an exosome population versus the more general term “sEV”, which suggests that the isolation procedure is primarily collecting exosomes.

To validate exosome identity, western blots were performed to probe CD9 tetraspanin expression (**Fig. 4a**). Due to the dilution caused by an SEC isolation procedure, samples were below the detection limit to quantify protein concentration via BCA. Despite this, equal volumes of sEV samples were loaded in each lane, and results indicate strong presence of CD9 on MCF10CA1 sEVs, presence on MCF10DCIS sEVs, and weak presence on MCF10A sEVs. Weak banding from MCF10A sEVs likely suggests low protein yield since protein concentration was below the detection limit for BCA.

Tetraspanin presence on individual sEVs was further assessed via an ExoView instrument (**Fig. 4b**). All three lines demonstrated the presence of each tetraspanin target (CD63, CD81, CD9) when compared to the negative MIgG isotype control (**Fig. 4c**; red box). sEVs from each cell line exhibited the highest presence of CD9 compared to CD63 and CD81 as evidenced by the highest level of sEV capture via the CD9 tetraspanin capture spot compared to CD63 and CD81 tetraspanin capture spots. Presence of tetraspanins provided further evidence that a significant portion of the sample isolates derived from endosomal origin and could thus be termed “exosomes”. The general term “sEV” will still be used moving forward to account for non-exosome particles which also likely comprise a population of the isolate.

Comparing the number of sEVs from each of the cell lines at each capture spot revealed general differences in sEV tetraspanin composition (**Fig. 4d**). Since the ExoView technique requires staining with different fluorescently conjugated antibody targets, direct comparisons between different targets within the same tetraspanin capture spot cannot be performed. Rather, comparisons can be made between sEVs stained with the same fluorophore antibody which is reflected by the dotted lines in **Figure 4d** (e.g. direct comparisons can only be made within the dotted line separators; e.g. MCF10A CD63 target cannot be compared with CD81 or CD9 target even within the same capture antibody). The resulting trends demonstrate significant sEV

heterogeneity in tetraspanin presence across the MCF10 series. General trends demonstrate low presence of CD81 for MCF10CA1 sEVs and high presence of CD9. MCF10A and MCF10DCIS sEVs also display distinct tetraspanin presence although no clear trend can be discerned. These data further support the consensus that sEVs from distinct cell sources can carry markedly different protein profiles[109], and significantly, that these profiles can transform with malignancy.

To ensure sEVs were properly stained with Cell Trace Far Red (CTFR), CTFR-stained sEVs were loaded on ExoView chips and the number of captured CTFR+ particles was assessed

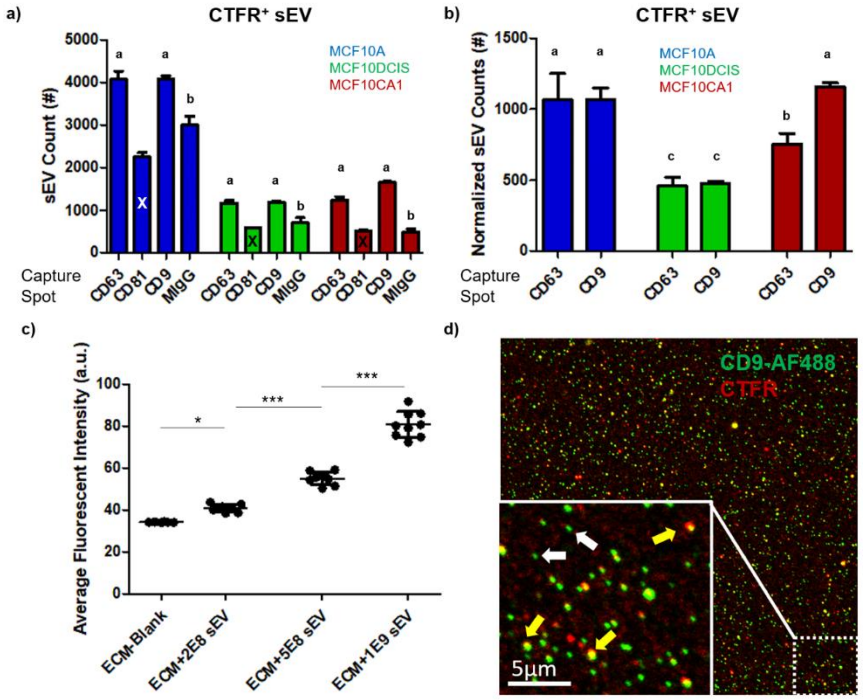

Figure 5. sEVs are stained with CellTrace Far Red (CTFR) and are visible via confocal microscopy. a) ExoView analysis revealed sEVs captured by CD63 and CD9 were CTFR$^+$ compared to MIgG control, while CD81 sEVs were negative. Letters above data denote statistically distinct groups compared to relevant MIgG control. $p<0.05$ (stronger significance between some conditions); One-way Anova, Tukey post-hoc. b) When normalized to MIgG controls, similar numbers of MCF10A and MCF10CA1 sEVs captured by CD63/CD9 and CD9 respectively were CTFR$^+$. Lower amounts of MCF10CA1 CD63 captured sEVs as well as MCF10DCIS CD63/CD9 captured sEVs were CTFR$^+$. Differences in symbol denotes statistical significance. $p<0.05$ (stronger significance between some conditions); One-way Anova, Tukey post-hoc. c) A fluorescence calibration curve demonstrates increasing sEV concentrations can be recorded via confocal microscopy. ECM: 3 mg/ml laminin-rich ECM. *$p<0.05$, ***$p<0.001$; One-way Anova, Tukey post-hoc. d) MCF10CA1 sEVs were stained with CTFR and CD9-AF488 conjugated antibody and isolated via size exclusion chromatography to remove unbound antibody. Confocal imaging revealed significant colocalization (yellow arrows), as well as single CD9-AF488$^+$ particles (white arrows).

(**Fig. 5a,b**). Comparing to the negative MIgG control, CD63 and CD9 captured sEVs were $CTFR^+$ for each cell line while CD81 captured sEVs were not. Normalizing tetraspanin capture by MIgG control, demonstrated similar CTFR staining between MCF10A CD63 and CD9 captured sEVs and MCF10CA1 CD9 captured sEVs. Fewer MCF10DCIS sEVs stained positive for CTFR. Despite differences in $CTFR^+$ sEV populations, each set showed ample presence of CTFR+ sEVs for downstream *in vitro* experiments.

To confirm visualization by confocal scanning microscope, a fluorescent intensity concentration curve was generated by loading increasing concentrations of CTFR-labeled sEVs in laminin-rich ECM (**Fig. 5c**). As expected, increasing sEV concentrations resulted in measurable increases in fluorescent intensity. Comparison between the blank (laminin-rich ECM) control and the 2e8 EV condition reveals the minimum detectable limit in this experimental setup.

To further confirm visualization by confocal microscopy, sEVs from the MCF10CA1 line were co-stained with a fluorescently-conjugated anti-CD9 antibody prior to SEC isolation in order to separate free antibody from sEV-bound antibody. Confocal analysis demonstrated colocalization of AF488-CD9+CTFR+ particles (**Fig. 5d**), although a sizeable percentage of CD9+CTFR- particles were present. These CD9+CTFR- particles could be a subpopulation of sEVs that was unable to be stained by CTFR or could be false signal due to the accumulation of antibodies.

To assess laminin-binding integrin expression on MCF10 series sEVs, western blots were performed targeting integrins α3, α6, and β1. Since sEV isolates were too dilute to perform BCA, maximum volumes of each fraction were added to gel lanes. MCF10CA1 sEVs possess high levels of each integrin assessed, while MCF10DCIS sEVs only stained positive for integrins α3 and α6 (**Fig. 6**). MCF10A sEVs showed a slight positive band for integrin α3. Due to the inability to load normalized amounts of sEVs per lane, these results should not be used for comparison between lines. Rather, they serve as binary evidence for integrin presence on each sEV

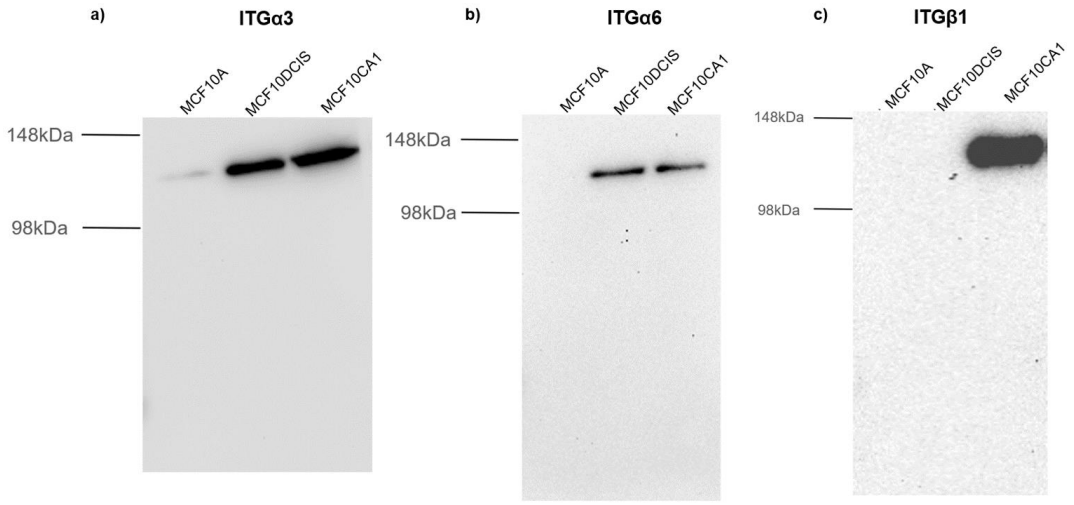

Figure 6. Select sEV isolates possess laminin-binding integrins α3, α6, β1 by western blotting. a) sEVs from all MCF10 lines possess integrin α3 while b) only MCF10DCIS and MCF10CA1 sEVs possess α6. c) MCF10CA1 sEVs were the only sEV samples positive for integrin β1. Samples were below the detection limit for BCA, and therefore maximum sample volume was loaded per well.

population. Lack of signal in MCF10A and MCF10DCIS lanes could reasonably be assumed to be due to lack of protein sample.

While western blot can reveal the presence of protein on bulk sEV samples, further analysis was needed to demonstrate presence of colocalized integrins on individual sEVs. CTFR stained sEV samples from each cell line were immobilized on ExoView chips and probed for laminin-binding integrins α3, α6, and β1. Integrin positive sEVs were determined by thresholding against the MIgG negative control. Comparison across the lines revealed significantly increased

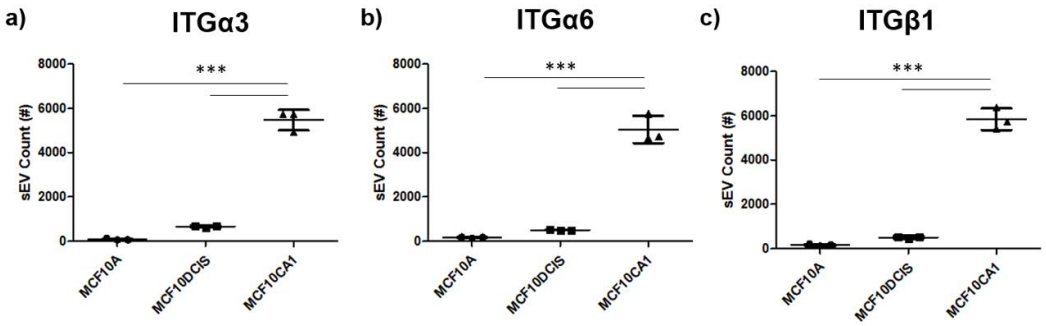

Figure 7. Increasing sEV presence of laminin-binding integrins α3, α6, β1 with malignancy. a) Loading the same concentration of sEVs revealed increasing expression of integrin α3, b) α6, and c) β1 with parent cell malignancy by ExoView analysis. MCF10A and MCF10DCIS sEVs were statistically similar. ***p<0.001; One-way Anova, Tukey post-hoc.

expression of all three integrins on MCF10CA1 sEVs compared to normal or pre-malignant MCF10A or MCF10DCIS sEVs (**Fig. 7**). Interestingly, there was no significant difference between MCF10A and MCF10DCIS sEVs.

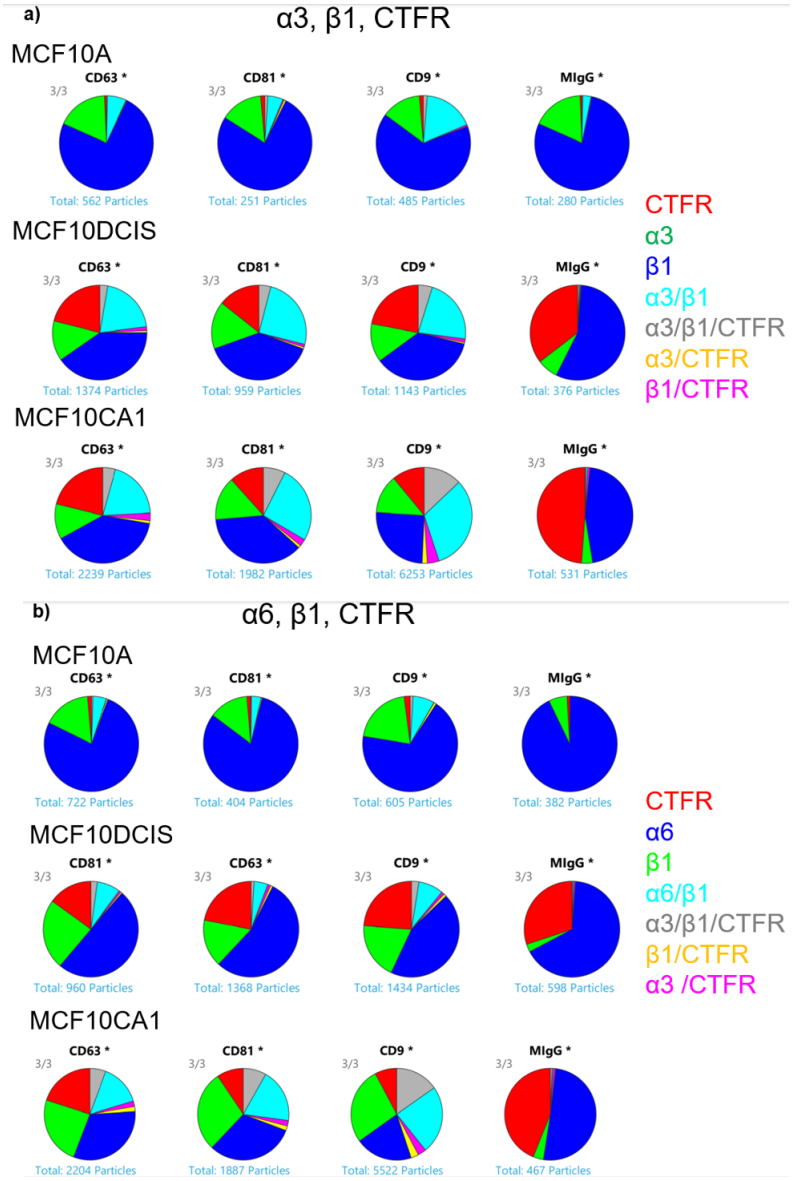

Figure 8. Variable integrin colocalization across MCF10 series sEVs. a) Pie charts comparing CTFR$^+$, integrin α3, and integrin β1 colocalization generally show higher percentages of colocalized markers on increasingly malignant sEVs. b) CTFR$^+$, integrin α6, and integrin β1 colocalization follows a similar trend. Although the same number of sEVs (counted by NTA) were loaded, differences in captured sEV counts were observed.

Integrins require dimerization of α and β subunits to effectively bind ligand targets[110], which prompted analysis of the colocalization of integrins α3, α6, and β1 on individual sEVs. Colocalization pie charts were generated to show integrin colocalization as well as integrin+CTFR colocalization on individual sEVs (**Fig. 8**). The presence of colocalized integrins on individual sEVs (**Fig. 8**; cyan+gray fractions) increased with increasing parent cell malignancy for both α3β1 and α6β1 integrin pairs. Since downstream *in vitro* experiments were limited to only visualize sEVs that were $CTFR^+$, comparison of $\alpha3\beta1^+CTFR^+$ and $\alpha6\beta1^+CTFR^+$ fractions (**Fig. 8**; gray fractions) also shows increasing colocalization. The summation of integrin-double positive sEVs and integrin-double positive $CTFR^+$ sEVs (**Fig. 8**; cyan+gray fractions), revealed overall increases in colocalization with increased parent cell malignancy (**Table 1**).

The results of these studies demonstrate that: 1) sEV secretion increases with increasing malignant potential; 2) laminin-binding integrin expression on sEVs increases with increasing malignant potential; and 3) integrins α3 and α6 colocalize with β1 on individual sEVs. Although colocalization does not necessarily guarantee integrin dimerization, these experiments provide strong support for further in-depth analysis of sEV binding and functionality.

Table 1. The percentage of MCF10 series sEVs with colocalized integrins.

	MCF10A	MCF10DCIS	MCF10CA1
CD63 Capture			
α3β1	7%	23%	24%
α6β1	5%	6%	20%
CD9 Capture			
α3β1	19%	27%	45%
α6β1	8%	11%	39%

Chapter 4: sEV Diffusive Transport through Laminin-Rich ECM

To assess sEV functional interactions with laminin-rich extracellular matrix, sEVs were treated to model different integrin activation states (**Fig. 9**). Although integrins must form non-covalent heterodimer pairs to facilitate ligand binding, dimerization does not guarantee binding[111]. Rather, integrins can exist in a range of activation states governed by both inside out as well as outside in signaling[112,113]. For the purposes of this study, only outside-in signaling integrin affinity was assessed via the introduction or omission of key divalent metal ions and through functionally validated integrin blocking antibodies. For integrins to form heterodimer pairs, divalent cations such as Ca^{2+} or Mg^{2+} are necessary to stabilize the interaction[111].

Chelating free cations via EDTA or inhibiting integrin activity via functionally-validated integrin blocking antibodies[114] prevents integrin binding (**Fig. 9a**). It is unclear whether the introduction of these antibodies prevents the formation of heterodimers or prevents heterodimers from binding requisite ligands. To model intermediate integrin binding affinity, physiologic ion concentrations of $MgCl_2$ and a reduced physiologic concentration of $CaCl_2$ were mixed with sEVs (**Fig. 9b**). A sub-physiologic $CaCl_2$ concentration was selected to enable the highest chance of

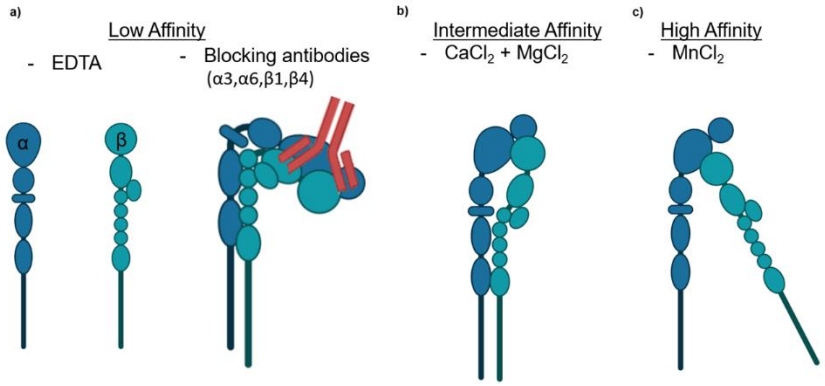

Figure 9. Graphical depiction of integrin activation states. a) Integrins exist as distinct subunits and require the presence of divalent cations to dimerize. Low affinity integrin binding was induced with EDTA (divalent cation chelator) or with the introduction of functionally inhibitory integrin blocking antibodies. b) Intermediate affinity integrin binding was induced with physiologic divalent cations Ca^{2+} and Mg^{2+}. c) Integrins were placed in a high affinity binding state by introducing Mn^{2+} which locks integrin dimers into a hyper-affinity binding state.

integrin binding with physiologic divalent cations due to the inhibitory effects of Ca^{2+} on integrin dimerization[115]. Alternatively, the addition of Mn^{2+} has been demonstrated to not only displace Ca^{2+} or Mg^{2+} to stabilize integrin dimers, but also locks integrins into an active-binding state[115] (**Fig. 9c**).

To demonstrate dynamic binding between sEVs and laminin-rich ECM, we first employed particle tracking via optical confocal microscopy. Although the size range of the sEVs of interest in this study is 50-150 nm in diameter, optical techniques in the form of confocal microscopy have been leveraged to track individual sEVs despite particle sizes smaller than the wavelength of

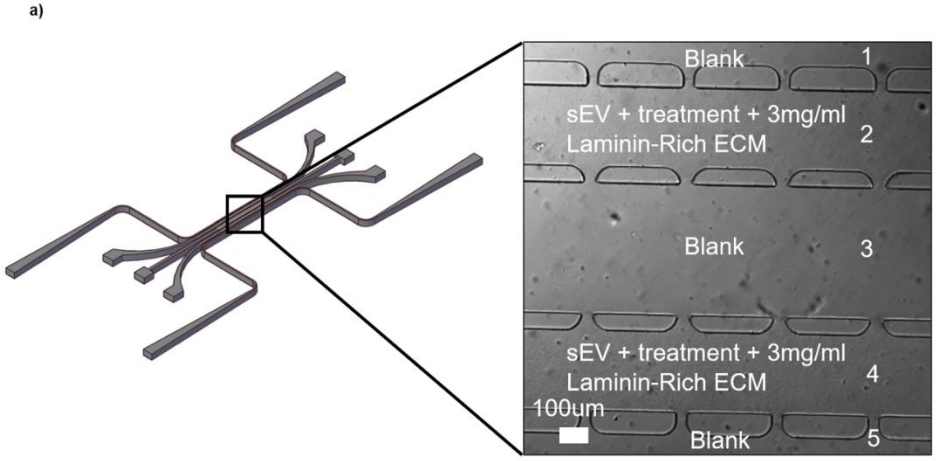

Figure 10. The experimental design to assess sEV diffusion. a) A microfluidic platform featuring five parallel chambers (1-5) was loaded with fluorescent beads or $CTFR^+$ sEVs with the experimental treatment condition in 3 mg/ml laminin-rich ECM in chambers 2 and 4.

emitted light[70]. We assessed the diffusion of both 100 nm diameter fluorescent polystyrene beads and sEVs using a microfluidic platform previously developed in the lab. Fluidic channels were loaded with either the beads or CTFR-stained sEVs in a laminin-rich ECM (**Fig. 10**). Bead+ECM or sEV+ECM solutions were loaded in either chamber 2 or chamber 4, with chambers 1, 3, and 5 left empty to ensure no mixing between experimental conditions. No hydrostatic pressure heads were added to the device to ensure bulk convective flow remained negligible.

Proof of principle particle tracking studies with 100 nm diameter fluorescent polystyrene beads validated the capability to track 100 nm particles (**Fig. 11**). Particles could be tracked over several image frames, and tracks exhibited “random-walk” Brownian diffusion. No bulk shifts in

track direction were evident, suggesting convective flow was indeed negligible. Extracting the diffusion coefficient from the mean squared displacement of tracks revealed slightly decreased effective diffusion (D_{eff}) for particles embedded in laminin-rich ECM (Matrigel) compared to particles in PBS (**Fig. 11b**). These results indicate there are properties of the ECM which inhibit the transport of a 100 nm particle, although these effects were relatively minor (~30% reduction in D_{eff}). It is unclear whether decreased D_{eff} is due to steric effects of the ECM (e.g. pore size) or properties of the polystyrene beads (e.g. electrostatic interactions).

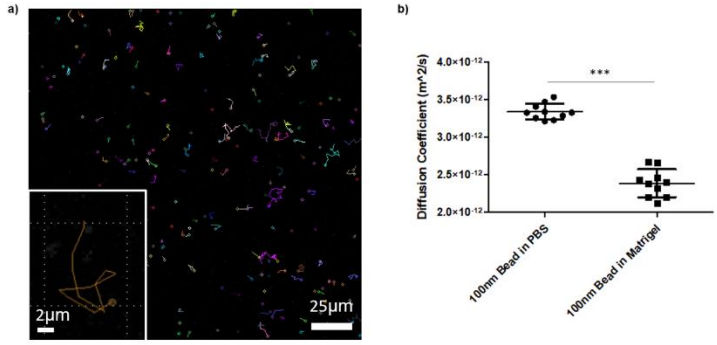

Figure 11. 100 nm beads show diminished D_{eff} in matrix. a) Particle tracks show numerous tracks with random paths suggesting primarily diffusive transport with negligible convective flow. b) Diffusion coefficients were extracted from the mean square displacement of particle tracks and revealed reduced D_{eff} for beads in 3 mg/ml matrix compared to a PBS control. ***p<0.001; Two-tailed T-test.

To assess sEV diffusion via particle tracking, CTFR-labeled sEVs from each of the MCF10 lines were treated with each integrin activating/blocking condition, mixed with laminin-rich ECM, and loaded into the microfluidic device as performed in the bead diffusion studies. Resulting sEV tracks were visible over several image frames, and demonstrated heterogeneous transport phenotypes (**Fig. 12a,b**). To differentiate bound, partially bound, and freely diffusing sEVs, 60 observations were selected for each transport phenotype to generate D_{eff} cutoff values (Fully bound: D_{eff}<7.25E-14 m^2/s ; Partially bound/bound and released: 7.25E-14 m^2/s<D_{eff}<3.88E-13 m^2/s ; Freely diffusing: D_{eff}>3.88E-13 m^2/s). Comparing bound sEV fractions across various integrin activation states demonstrated the highest percentages of bound sEVs when treated with integrin-activating Mn^{2+} (**Fig. 12c-e**). Binding was reduced with the addition of the integrin antibody blocking cocktail for MCF10DCIS and MCF10CA1 sEVs (**Fig. 12d,e**). Physiologic Ca^{2+} and Mg^{2+} conditions resulted in the lowest fractions of bound sEVs with a marginal impact of integrin blocking

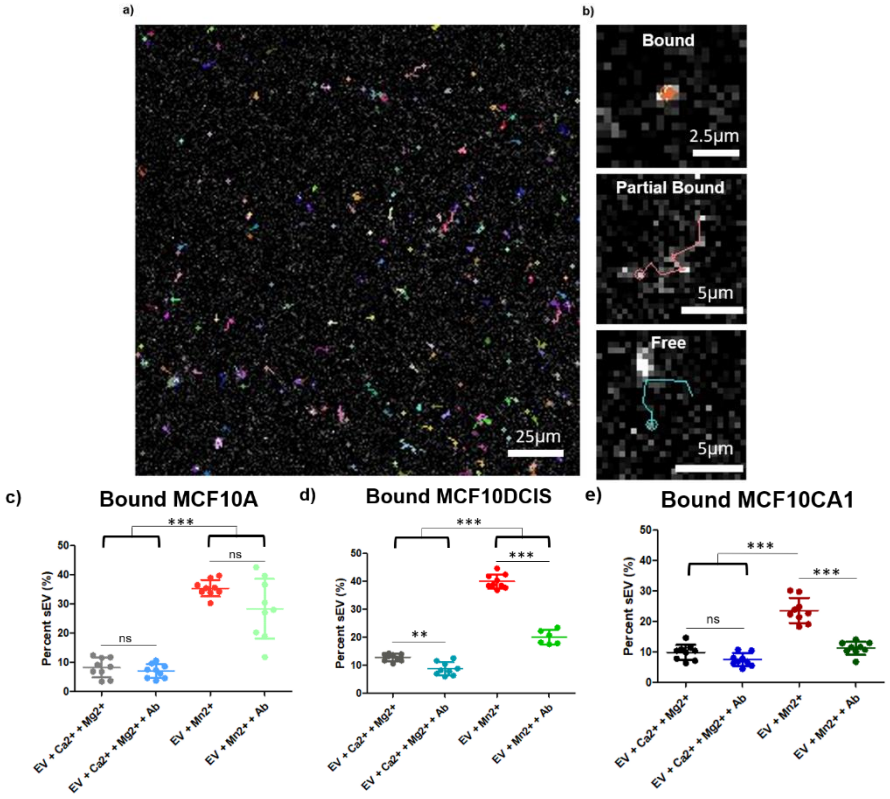

Figure 12. sEV diffusive transport is influenced by anti-integrin blocking antibodies. a) Representative image of sEV particle tracks. Many tracks were captured in each field of view, and random particle paths indicate diffusive transport with negligible convective flow. b) sEV populations exhibited unique transport properties. Subpopulations of sEVs were found to be fully bound (D_{eff}<7.25E-14 m^2/s), free (D_{eff}>3.88E-13 m^2/s), or exhibited instances of binding and release (7.25E-14 m^2/s<D_{eff}<3.88E-13 m^2/s). Representative image tracks display each subpopulation. c) Higher percentages of MCF10A sEVs treated with Mn^{2+} were bound compared to physiologic ions, although no difference was found with blocking antibodies. ***p<0.001; One-way Anova, Tukey post-hoc. d) Higher percentages of MCF10DCIS sEVs treated with Mn^{2+} were bound compared to physiologic ions, and binding was statistically reduced with the addition of integrin blocking antibodies. **p<0.01, ***p<0.001; One-way Anova, Tukey post-hoc. e) MCF10CA1 sEVs displayed a similar trend to MCF10DCIS sEVs, although physiologic ion conditions did not exhibit reduced bound percentage with the addition of integrin blocking antibodies. ***p<0.001; One-way Anova, Tukey post-hoc.

antibodies. Although we expected higher total percentages of bound MCF10CA1 sEVs due to higher colocalization of laminin binding integrins compared to MCF10DCIS and MCF10A sEVs, this trend was not observed. This result could be due EV clumping which was more prevalent in MCF10CA1 conditions (effectively sequestering large amounts of bound EVs) or due to inherent biases in the particle tracking methodology (preference for only the largest, brightest particles).

A significant limitation of this particle tracking technique is the inherent size bias of the particles observed. Larger diameter sEVs have larger volumes (assuming a sphere, volume scales with r^3), and thus the potential to contain higher concentrations of CTFR. Therefore, although particle tracking has been used to demonstrate sEV transport, criticisms surrounding the ability to dynamically track individual particles given optical constraints and particle size bias encouraged us to consider assessing sEV diffusion via bulk transport. Fluorescence recovery after photobleaching (FRAP) analysis afforded the ability to not only measure sEV diffusion in bulk, but also to derive kinetic binding parameters including K_{on}, K_{off}, and K_d[106]. These kinetic parameters can be observed directly from the shape and recovery profile of FRAP curves (**Fig. 13**). The asymptotic level reached by FRAP curves is indicative of a bleached immobile fraction as well as the unbleached freely diffusing mobile fraction[116,117].

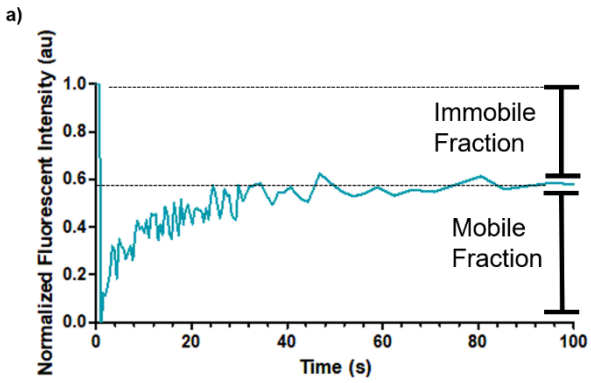

Figure 13. Characteristic fluorescence recovery after photobleaching (FRAP) curve. a) Fluorescent species (1 a.u.) are bleached with a high intensity laser (0 a.u.), and recovery dynamics are recorded in the bleached region of interest. Where the FRAP curve asymptotically recovers to in relation to pre-bleach intensity reveals the proportion of species that are freely mobile versus immobile.

The FRAP methodology and the analysis pipeline was first validated by performing bleaching experiments with 40 kDa and 70 kDa dextran as well as 100 nm fluorescent beads (**Fig. 14**). Dextran conditions recovered to nearly 1 a.u., reflective of the expected lack of binding to matrix. Curve fitting was successfully performed for all conditions despite noisy recoveries for 100 nm beads. Diffusion coefficients were then extracted from the fitted recovery curves and compared to theoretical (Stokes-Einstein)[118] diffusion coefficients in water (**Fig. 14d**). Interestingly, measured D_{eff} of 100 nm beads in ECM were comparable to D_{eff} values measured through particle tracking (**Fig. 11**). While FRAP measurement were not recorded for freely

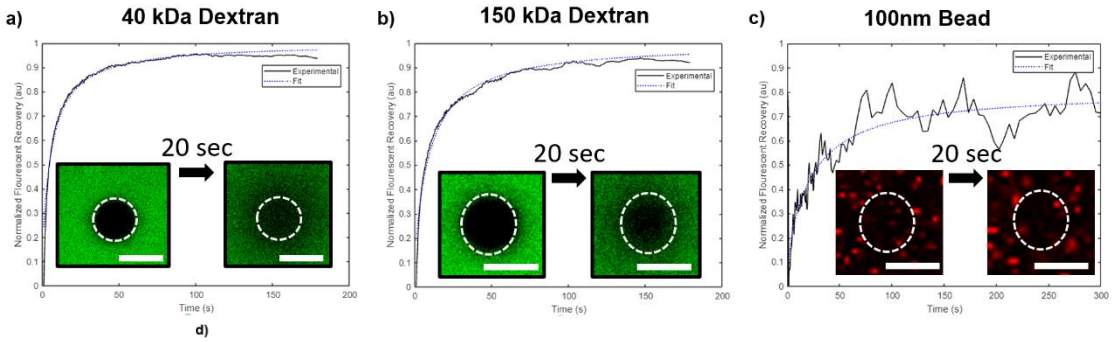

d)

	Measured D_{eff} (m^2/s) in 3mg/ml laminin-rich ECM	Theoretical D (m^2/s) in Water
40 kDa Dextran	1.578E-11	3.53E-11
150 kDa Dextran	9.39E-12	2.59E-11
100 nm Fluorescent Beads	1.04E-12	4.6E-12

Figure 14. FRAP methodology is validated with 40 kDa dextran, 150 kDa dextran, and 100 nm fluorescent beads. a) 40 kDa FITC dextran, b) 150 kDa FITC dextran, and c) 100 nm red fluorescent polystyrene beads all demonstrated characteristic FRAP recoveries in 3 mg/ml laminin rich ECM. Representative bleach spot recoveries over 20 seconds. Scalebars=20 µm; n=6-9 averaged replicates per curve. d) Extracted effective diffusion coefficients from fitted curves were lower, but comparable to theoretical diffusion coefficients of each species in water.

diffusing dextran and beads in these sets of experiments, similar but lower D_{eff} values compared to theoretical free diffusion in water supported the validation of the FRAP methodology.

With the FRAP methodology and analysis pipeline validated, sEV samples were embedded in laminin-rich ECM and FRAP experiments were performed. Model fits closely matched representative experimental data (**Fig. 15**). As outlined in Sprague *et al.*[106], three parameters required fitting; the effective diffusion coefficient (D_{eff}), the forward reaction (binding) constant (K_{on}), and the reverse reaction (release) constant (K_{off}). An array of potential values was provided for each parameter, and the sum of squares residual (SSR) was minimized to approximate each value (**Fig. 15b**). K_{on} and K_{off} fitted values are evident by the minimum in the sum of squares residual plot (**Fig. 15b**; black arrow). As noted in the text of Sprague *et al*, fitting for exact values of K_{on} and K_{off} is difficult due to the long trough of minimized SSR. Therefore, the ratio of two, K_d ($K_d=K_{off}/K_{on}$) was utilized to compare kinetic parameters between different experimental conditions.

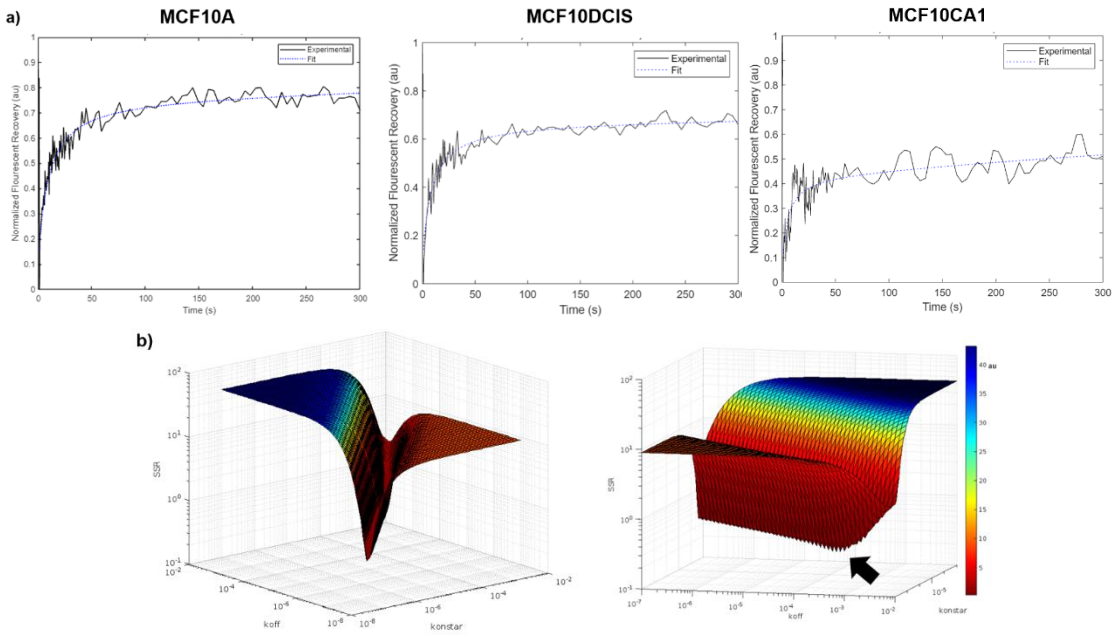

Figure 15. MCF10 series sEVs can be fit by FRAP equations. a) Representative FRAP curves for sEVs from each MCF10 line were fit by published equations[106], despite noisy features in the curves. b) Surface plots displaying sum of squares residuals for two of the fitted parameters (K_{on}, K_{off}) showed a minimized trough representing a range of potential solutions which would provide approximate fits to the curves. Minimums are achieved (black arrow), which reflected the K_{on} and K_{off} pair with minimized error.

To further explore the sensitivity of the fitting procedure, a sensitivity analysis was performed on representative curves to determine the effects of changing K_{on} and K_{off}. Maintaining the fitted value of K_{off} constant and performing a parameter sweep for K_{on} significantly affected fitted curves (**Fig. 16a**). Deviations from the ideal fit where smaller when K_{on} was smaller than the refined fit versus when K_{on} was larger. Similarly, large changes in fits were observed by holding K_{on} constant and sweeping K_{off} (**Fig. 16b**), but increasingly larger K_{off} values resulted in smaller deviations (compared to lower K_{on} values in **Fig. 16a**). Interestingly, keeping the same value of K_d constant but multiplying K_{on} and K_{off} by the same constant value resulted in minimal changes in the model fit (**Fig. 16c**). Deviations from the model fit were larger when K_{on} and K_{off} were higher than refined fit parameters. Due to minimal deviations in the K_d sweeps compared to K_{on} and K_{off} sweeps, K_d was selected as the kinetic parameter to compare between sEV treatment conditions.

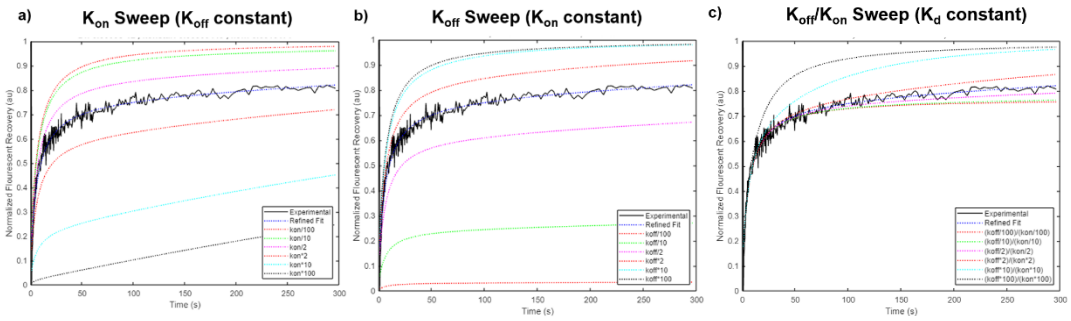

Figure 16. Sensitivity analysis demonstrates sensitivity of fitting procedure. a) K_{on} parameter sweeps while leaving K_{off} constant showed large deviations in model fits. b) K_{off} sweeps with a constant K_{on} revealed similar trends in model behavior to K_{on} sweeps. c) Maintaining K_d (K_{off}/K_{on}) constant, but multiplying K_{off} and K_{on} by the same scaling factor demonstrated the model was sensitive to specific values of K_{on} and K_{off} and not just the ratio of the two.

Following validation and interpretation of the FRAP fitting methodology, MCF10 FRAP fits were combined, averaged, and plotted according to the integrin treatment conditions (**Fig. 17**). For each condition, sEVs isolated from the malignant MCF10CA1 line exhibited the slowest and lowest recovery curves, followed by MCF10DCIS sEVs which shared 95% confidence intervals with MCF10A sEVs at most time points. Comparing conditions from the smoothed data, rather

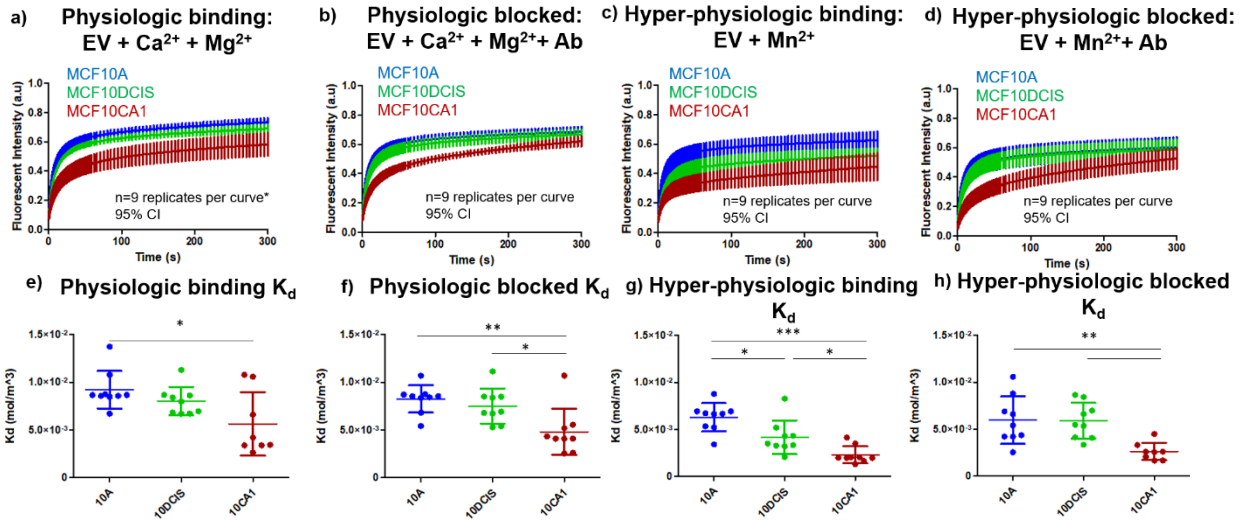

Figure 17. sEV diffusive transport is impacted by parent cell malignancy. a-d) FRAP recovery fitted curves were consistently slower and lower for malignant MCF10CA1 sEVs across all treatment conditions, followed by MCF10DCIS and MCF10A sEVs. Recoveries generally appeared to display asymptotic behavior by t= 300sec. Error bars= 95% CI; n=9 replicates per curve; n*=8 replicates for MCF10CA1 curve. e-h) Extraction of K_{on} and K_{off}, and subsequent calculation of K_d was consistent with behavior in FRAP curves. MCF10CA1 sEVs exhibited lowest K_d values, indicating the highest levels of sEV binding to the matrix. *p<0.05, **p<0.01, ***p<0.001; One-way Anova, Tukey post-hoc.

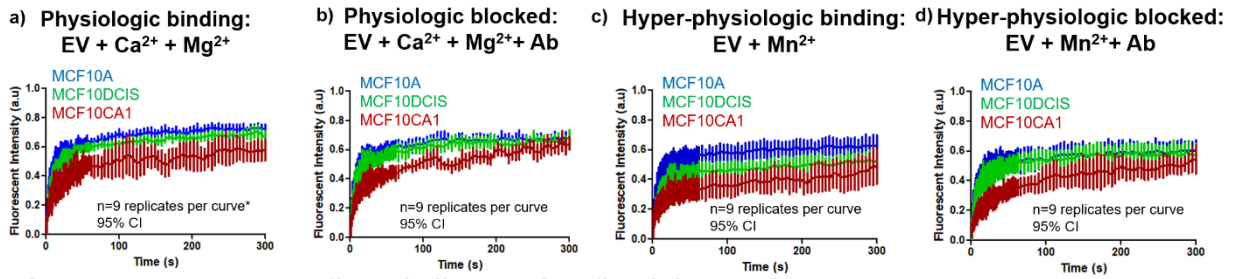

Figure 18. Raw curves reflect similar trend as fitted data. a-d) Raw FRAP recovery curves mirrored conclusions drawn from fitted curves. Due to the inherent noise characteristic of FRAP data, raw curves were generally noisier than their fitted curve counterparts. Error bars= 95% CI; n=9 replicates per curve; n*=8 replicates for MCF10CA1 curve.

than the curve fits (**Fig. 18**), revealed similar trends, albeit with increased noise due to the inherent noise associated with the FRAP methodology. To directly compare the characteristic shapes of the recovery curves, and thus information regarding sEV binding, the dissociation constant K_d was compared across conditions by extracting the ratio of K_{off} and K_{on} from the parameter fits (**Fig. 17e-h**). sEVs from the MCF10CA1 line consistently exhibited the lowest K_d across all conditions. Integrin blocking had minimal impact on K_d.

Comparing the immobile, bound sEV fraction (C_{eq}) for each condition resulted in similar conclusions to K_d comparisons (**Fig. 19**). MCF10CA1 sEVs had higher bound fractions than MCF10A and MCF10DCIS under physiologic conditions (Ca^{2+}/Mg^{2+}). A step-wise increase in binding fraction was observed with hyper-physiologic sEV binding (**Fig. 19c**). As expected based on similar sEV size distribution, D_{eff} across cell lines and integrin activation conditions showed no statistical difference (**Fig. 20**). Differences between the FRAP recovery curves were therefore

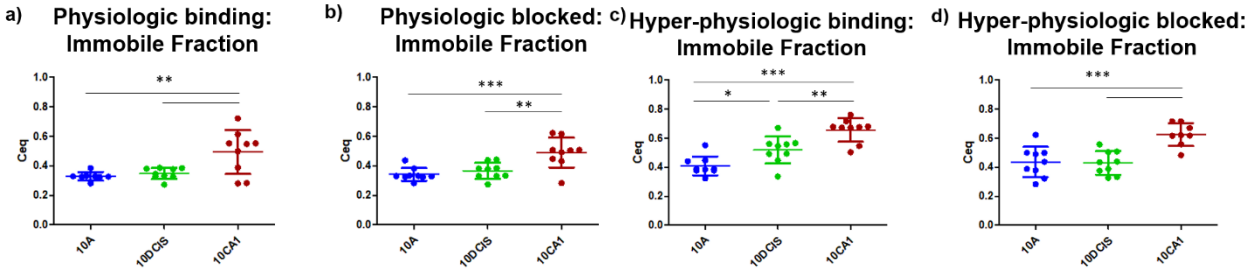

Figure 19 Increased sEV binding with parent cell malignancy. a-d) The bound fraction (C_{eq}) was assessed for each integrin binding state. Highest sEV binding fractions were observed with MCF10CA1 sEVs in all conditions compared to sEVs from MCF10A and MCF10DCIS. *p<0.05, **p<0.01, ***p<0.001; One-way Anova, Tukey post-hoc.

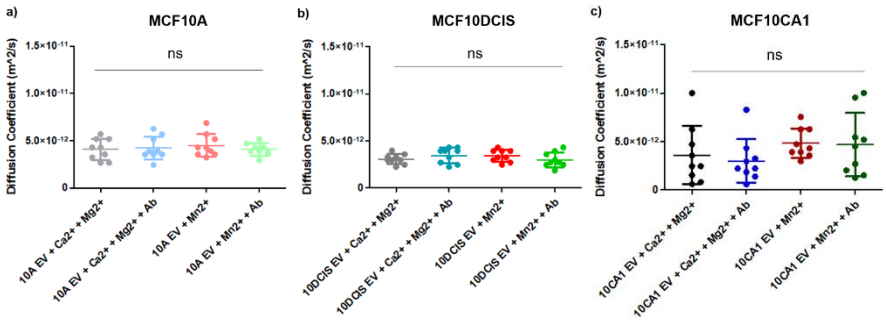

Figure 20. sEV D_{eff} does not vary with parent cell malignancy. a-c) Despite differences in recovery curves and K_d, fitted D_{eff} values did not vary across the sEV conditions nor across MCF10 line. One-way Anova, Tukey post-hoc.

captured by differences in K_d. These results indicate that any differences in transport and concentration of sEVs from between the cell lines is not due to differences in diffusion, but due to binding to the ECM.

Finally, the individual integrin blocking conditions were compared within each cell line to determine if these trends were explained entirely by integrin binding to laminin-rich ECM (**Fig. 21**). Although MCF10DCIS and MCF10CA1 sEVs display expected trends with lowest recovery in the Mn^{2+} treatment and higher recovery when treated with integrin blocking antibodies, 95% confidence intervals as well as a comparison across fitted K_d parameters suggest no statistically meaningful differences between the majority of the conditions (**Fig. 21**). The largest differences were expected within the MCF10CA1 sEV conditions since these sEVs were found to possess the highest amounts of surface integrins by ExoView analysis. While the inherent noise in FRAP measurements suggests larger sample sizes may be warranted, these studies suggest that integrin binding can only partially explain differences between the cell lines in ECM binding (**Fig. 17**). Alternative mechanisms such as sEV entrapment due to ECM pore size, alternative ligand binding pairs, or inadequate integrin blocking antibodies offer possible explanations to describe this behavior.

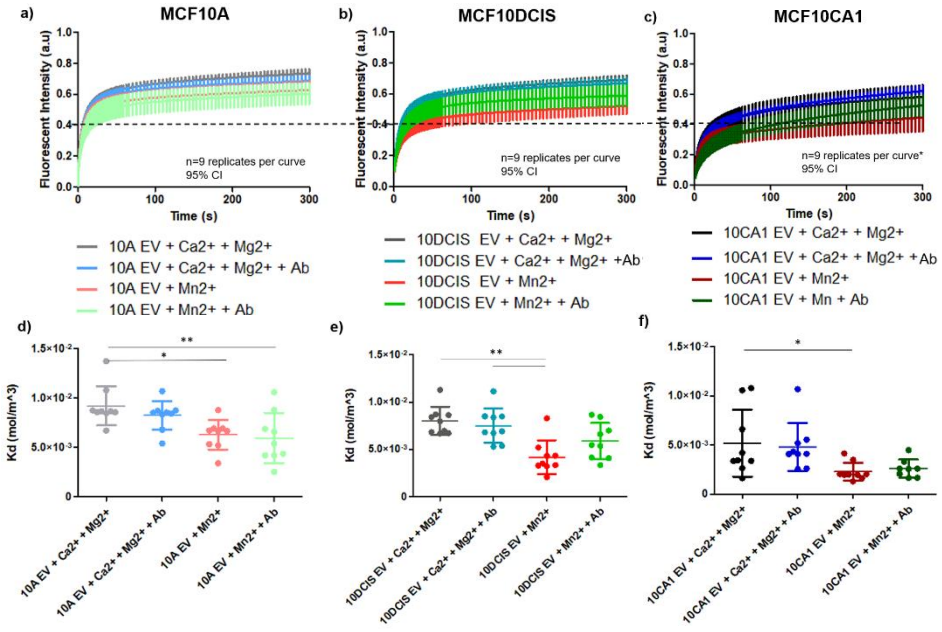

Figure 21. sEV diffusive transport is not fully explained by integrin activation state. a-c) Despite differences in sEV diffusion based on parent line malignancy, regrouping curves to compare the effect of integrin activation state revealed limited statistical differences. Error bars= 95% CI; n=9 replicates per curve; n*=8 replicates for MCF10CA1+Mn^{2+} curve. d-f) K_d values reflected the trends observed in the FRAP recovery curves. Some conditions were found to be statistically significant, and hyper-physiologic integrin binding Mn^{2+} K_d values were among the lowest across the conditions indicating that integrins likely are playing a partial role in sEV diffusive transport. *p<0.05, **p<0.01; One-way Anova, Tukey post-hoc.

Chapter 5: Finite Element Model of sEV Convective Transport in a Microfluidic Device

With properties of sEV diffusion and binding uncovered via FRAP, sEV non-equilibrium transport was investigated via computational finite element analysis in COMSOL. A geometry of the microfluidic device utilized in the FRAP experiments, as well as subsequent convective flow experiments, was imported into COMSOL. Kinetic binding parameters, theoretical hydrostatic pressure heads to generate physiological interstitial convective flow, matrix permeability, species concentrations, and diffusion coefficients were gathered from literature or found experimentally through iterative *in vitro-in silico* experiments (**Table 2**).

Table 2. Baseline modeling parameters used for *in silico* COMSOL simulations.

Parameter	Value	Units	Source
Permeability	2E-14	m^2	-Experimentally determined for 3mg/ml laminin-rich ECM
D_{free}	4.5E-12	m^2/s	-Theoretically determined for 100nm sphere via Stokes-Einstein[118] -Experimentally verified via NTA
D_{eff}	1.53E-12	m^2/s	-Approximated from experimental FRAP results and literature[70]
Concentration of binding sites	4.2E-3	mol/m^3	-Calculated from concentration of 3 mg/ml laminin-rich ECM with one binding site per laminin monomer[140]
EV influx concentration	4.16E-8	mol/m^3	-Experimentally determined via secretion rate of MCF10CA1 for approximate number of cells in 100 µm diameter tumor
Interstitial flow velocity	0.5E-6	m/s	-General value for interstitial flow according to published studies[67,68]

Initial simulations were designed to verify the model was performing as expected. A range of sEV binding states were assessed, representing values of K_{on} and K_{off} extracted from FRAP experiments as well as no binding and hyper-binding conditions (**Table 3**). This range of integrin binding states was applied to an initial model assessing a sweep of binding site and initial sEV concentrations (**Fig. 22**). Baseline parameters (**Table 2**) were applied with the exception of hydrostatic pressure head heights, which were set to 0 mm to ensure only sEV diffusion was assessed. Concentration curves of binding sites (**Fig. 22**; left column) and bound sEVs (**Fig. 22**;

right column) were plotted to match the interstitial concentration of the species at T=0 min and T=30 min over a uniform line profile across the interstitial space.

Table 3. Kinetic binding parameters for several theoretical sEV binding states.

Binding State	K_{on} (m^3/mol/s)	K_{on} (1/s)	K_d (mol/m^3)
No binding	0	0	n/a
Low binding (10A Ca^{2+} + Mg^{2+})	0.11272	9.39E-4	8.33E-3
High binding (10CA1 + Mn^{2+})	0.5418	1.115E-3	2.123E-3
High binding^{+}	5.418	9.39E-4	1.73E-4
High binding^{++}	54.18	9.39E-4	1.73E-5

Across all integrin binding states and initial binding site concentrations, consumption of binding sites was negligible (**Fig. 22b-f**; left column). This is evident by T=30 min curves completely overlapping T=0 minute curves for each condition, indicating no changes in concentration occurred over that time. Even at the highest level of binding (High binding^{++}; **Fig. 22f**; left column), T=0 min and T=30 min curves of binding site concentration completely overlapped. Considering the binding site concentration was calculated to be several orders of magnitude higher than sEV influx concentration, it is not surprising binding site consumption was negligible. Graphs of bound sEV fractions with increasing initial free sEV concentration (**Fig. 22b-f**; right column), demonstrate higher values of bound sEVs with higher integrin binding state and higher initial sEV concentrations (yellow curves, right column). These results indicate that sEVs have the potential to accumulate in the interstitial space which increases with K_{on} as well as the initial concentration of free sEVs.

With the computational modules validated, we first addressed whether sEV size, and resultant effective diffusivity "D_{eff}", could impact transport compared to traditional small molecule soluble mediators. A 100 µm diameter circle was added within the interstitial ECM to model a growing tumor (**Fig. 23**). Boundary conditions on the tumor periphery were set to continuously secrete sEVs at the baseline sEV influx concentration, and hydrostatic pressure heads were equilibrated so only the effects of diffusive transport would be assessed. Effects of sEV size on

a)

Parameter	Sweep of values (mol/m^3)
Concentration of Binding Sites	4.2E-5, 4.2E-4, 4.2E-3
Concentration of free sEV	3.825E-10, 3.825E-8, 3.825E-6

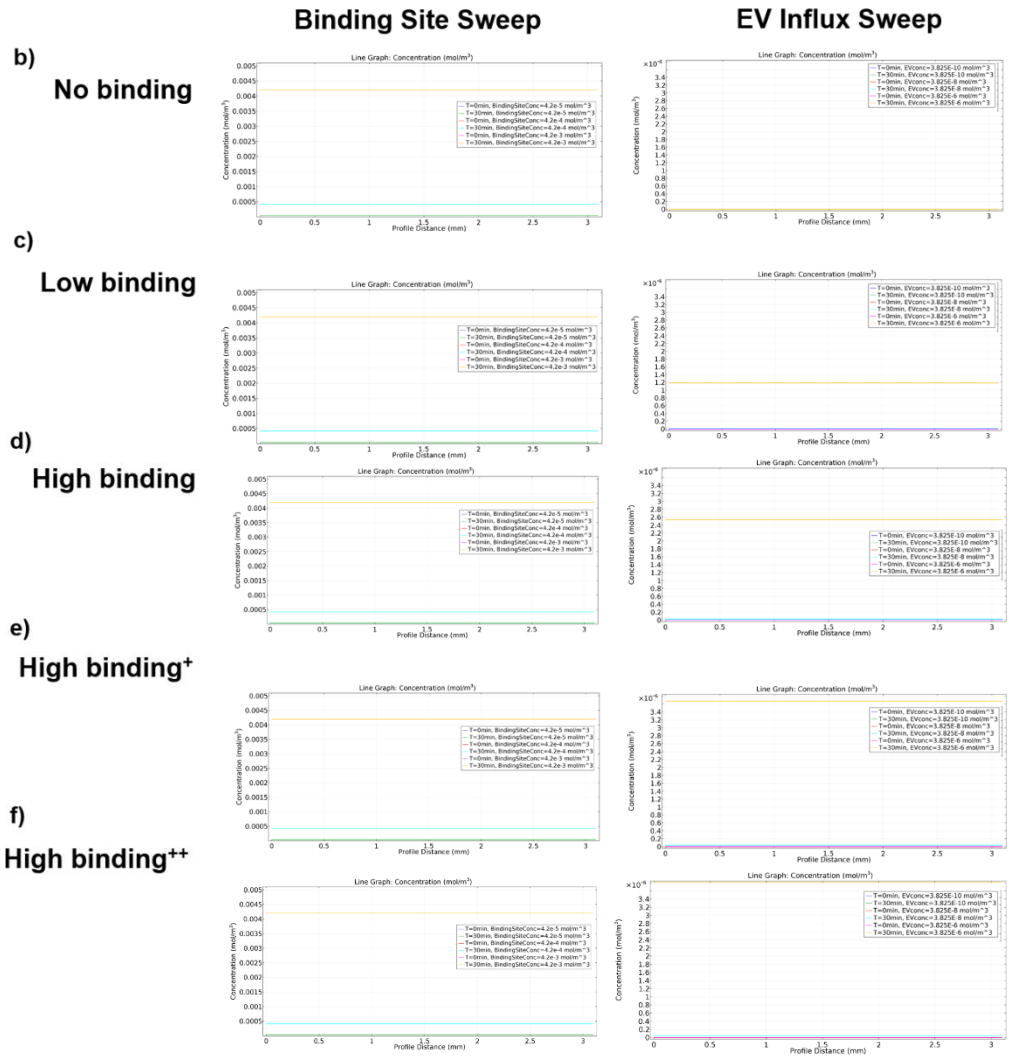

Figure 22. sEV bind matrix, and binding sites are in excess. a) Baseline simulation values were used (**Table 2**) with binding site concentration and free sEV concentration sweeps. Concentration profiles were generated to measure the concentration of binding sites (left column) or bound sEV concentration (right column) at T=30min. b) sEV with no binding (K_{on}=0 m^3/mol/s) showed no consumption of binding sites, nor generation of bound sEVs. c-f) Over the range of sEV binding conditions, binding sites showed negligible consumption. Increasing sEV binding resulted in higher concentrations of bound sEVs (yellow curves, right column).

a)

Condition	D_{eff} (m^2/s)
40kDa dextran	3.5E-11
Averaged FRAP sEV D_{eff}	1.53E-12
Range from Lenzini *et al.*[70]	1.53E-13
	1.53E-14
	1.53E-15

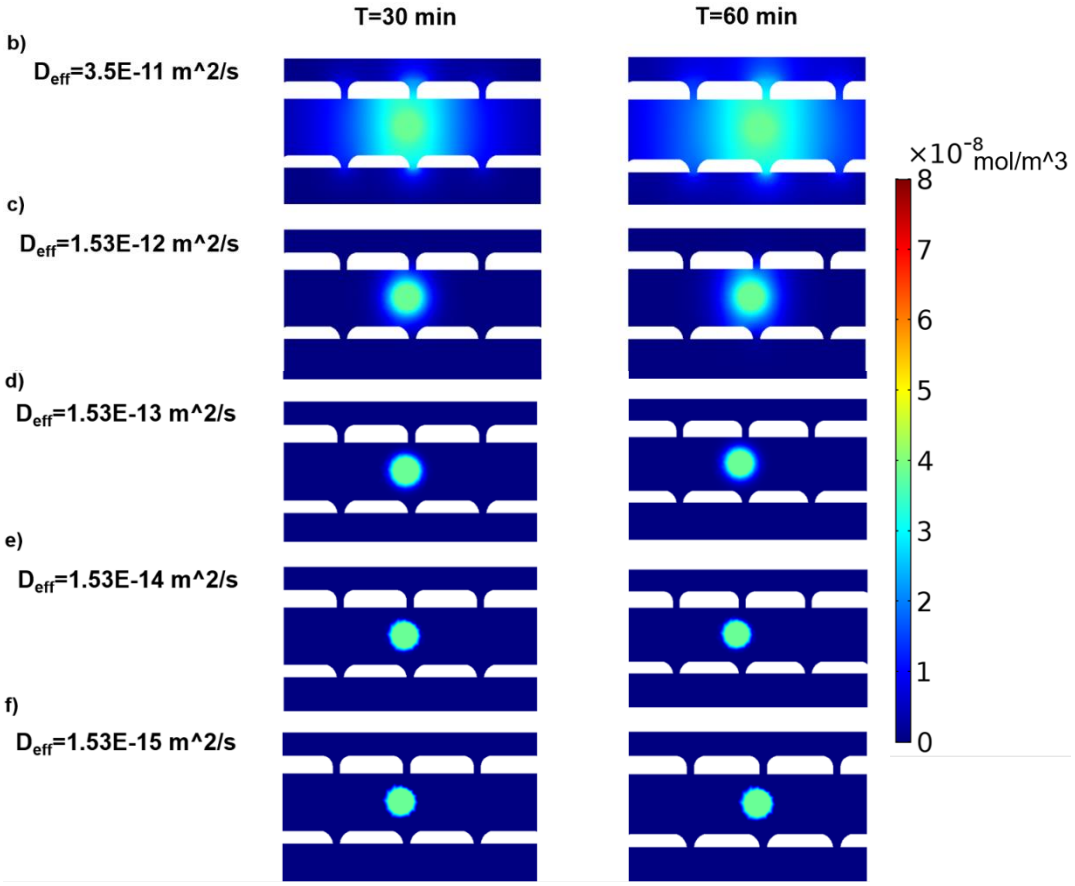

Figure 23. Low diffusion coefficients significantly impact sEV diffusive transport. a) Baseline simulation values were used with the introduction of sEV D_{eff} sweeps across a range of values. Hydrostatic pressure head heights were set to 0mm to ensure only sEV diffusion was assessed. A 100µm circle was initialized to continuously secrete sEV at the baseline influx value. Free sEV concentrations were assessed. b-f) Comparisons between T=30 and T=60min showed significantly reduced free sEV penetration into the surrounding matrix when D_{eff} values approximated sEV diffusion. (continued on next page).

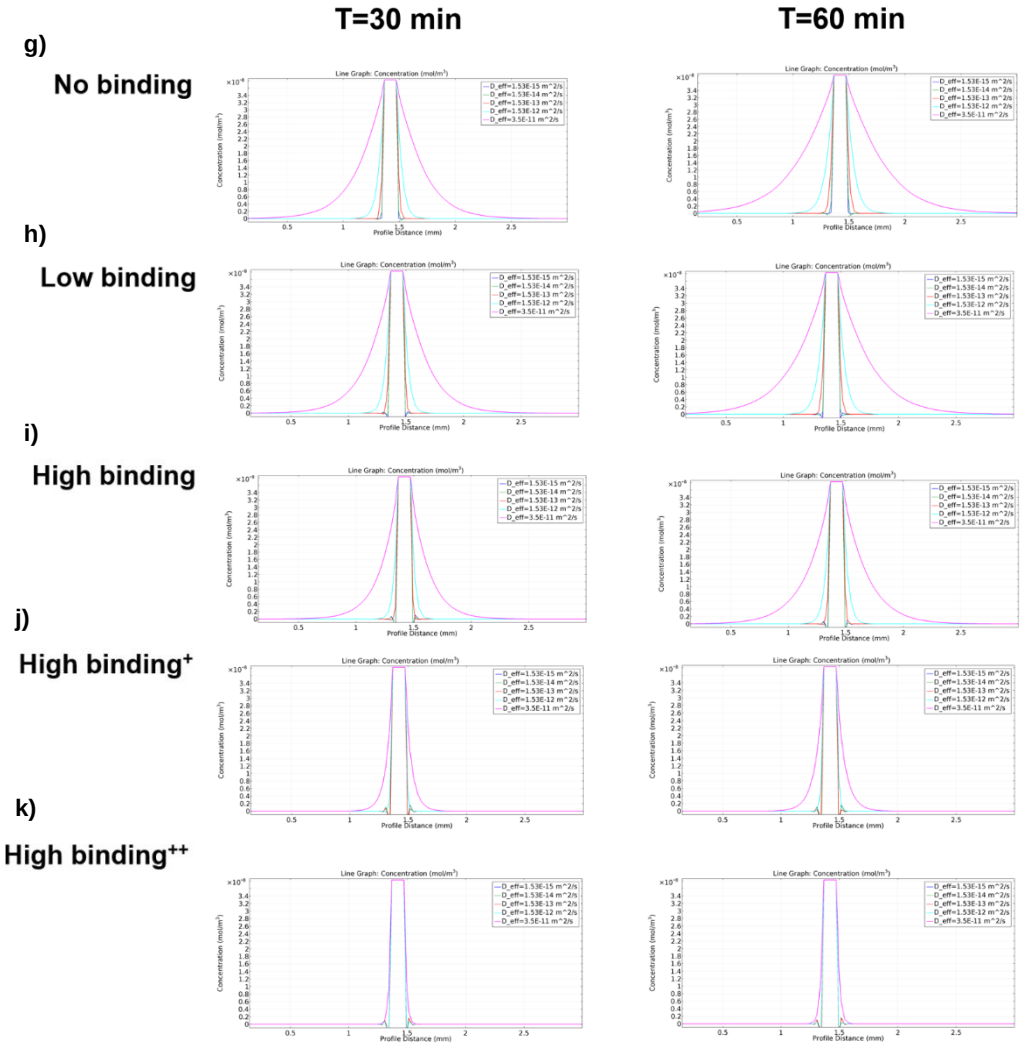

Figure 23. (continued). g-k) Concentration profiles generated with a line profile through the center of the 100 µm sEV-producing zone provided quantification.

diffusion were assessed through a sweep of D_{eff} (**Fig. 23a**). 40 kDa dextran was included to assess standard "small molecule" transport, while sEV D_{eff} values lower than what was measured experimentally were included to model published values of D_{eff}[70]. Species diffusion was captured at T=30 and T=60 min time points, and revealed significant differences in spatial free EV concentration profiles between "small molecule" diffusion coefficients and sEV diffusion coefficients (**Fig. 23b-f**). Differences between sEV tissue penetration at D_{eff}=1.53E-12 m^2/s through D_{eff}=1.53E-15 m^2/s were marginal which highlights the fact that diffusion coefficients

below a certain limit (~D_{eff}=1.53E-12 m^2/s) have diminishing effects on transport at these time and length scales.

Representation of spatial profiles by drawing a line profile extending across the 100μm zone of sEV secretion, further highlights these trends (**Fig. 23g-k**). Free EV profiles extended spatially from T=30 min to T=60 min but were reduced with increasing binding. Even without binding, curves with D_{eff}<1.53E-12m^2/s displayed similar sEV penetration which was distinct from the soluble mediator D_{eff}=3.5E-11m^2/s. These results indicate that due to the size of sEVs alone (and resulting lower D_{eff}), diffusive transport is negligible compared to that of small molecule soluble mediators. In the absence of convective flow, this results in pronounced differences in spatial concentration gradients.

With an initial assessment of sEV diffusive transport, we next evaluated the effects of convective interstitial flow on sEV transport and spatial distribution. A range of hydrostatic pressure head heights (∆H) between the central line (chamber 3) and outer fluidic lines (chambers 1 and 5) were applied to induce variations in interstitial (chambers 2 and 4) convective flow velocity (**Fig. 24a**). Line profiles drawn through the interstitial compartment revealed flow velocities ranging from 0.5-1 μm/sec (**Fig. 24b**). To determine the effect of interstitial flow velocity on free and bound sEV spatial concentration profiles in the interstitial space, flow velocities were varied across different integrin binding states (**Fig. 24c-g**). Profile curves at T=30 min show negligible consumption of binding sites for all integrin binding affinity and flows (**Fig. 24c-g**; right column). Concentration gradients were evident in both free and bound sEV species, and were steeper with increasing integrin binding affinity. Bound sEV profiles were an order of magnitude or more higher than the concentration of free sEVs (note y-axes scale). Significantly, faster interstitial flow velocities flattened free and bound gradients at all levels of integrin binding state. To match experimental interstitial flow velocities, all subsequent simulations were designed with hydrostatic pressure heads ∆H=5.5mm, resulting in average interstitial flow velocities of 0.5 μm/sec.

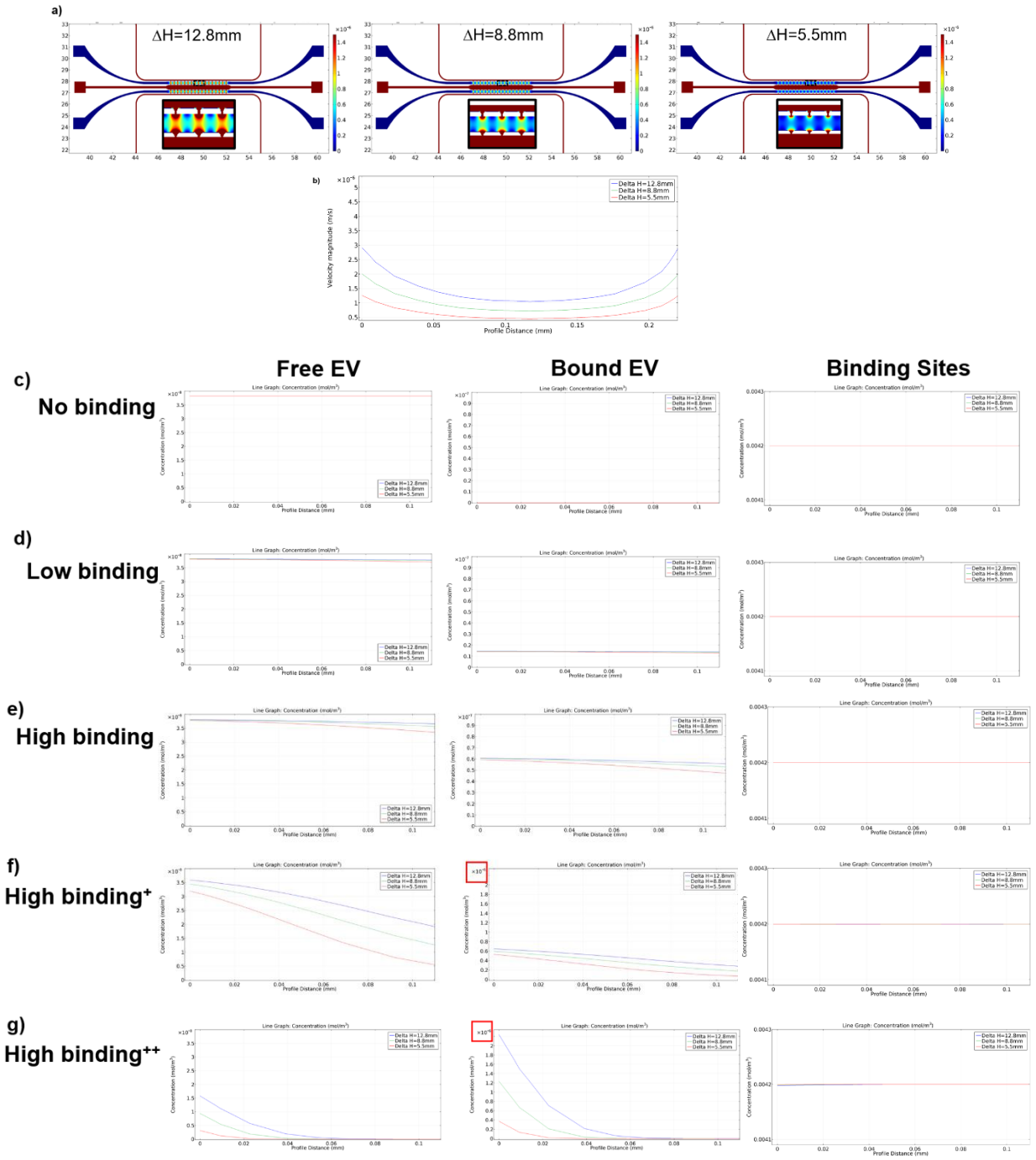

Figure 24. Higher convective flow flattens soluble and bound sEV gradients. a) Differences in hydrostatic pressure head height (ΔH) between the central line (chamber 3) and outer fluidic lines (chambers 1 and 5), resulted in b) average interstitial flow velocities ranging from approximately 0.5-1 μm/sec. c-g) Various integrin binding states affected the formation of free and bound sEV gradients in response to flow at the T=30 min timepoint. Only sEVs with high binding and above (e-f) showed appreciable formation of free and bound gradients (note-bound sEV high binding^{+} and high binding^{++} graphs y-axes are scaled differently).

We next asked whether differences in the diffusion coefficients of sEVs would affect convective transport to the extent it affected diffusive transport. Peclet numbers were calculated for various possible values of D_{eff} with a characteristic length of 100 µm and interstitial flow velocity of 0.5 µm/sec. (**Table 4**). Peclet numbers greater than 10 generally indicate situations where transport is considered convective-dominant while values less than 0.1 are considered in the diffusion dominant regime. Interestingly, while small molecule soluble mediator transport is around 1 (indicating both diffusion and convection play important roles in transport), all potential sEV D_{eff} values result in Peclet numbers greater than 10 which indicates convective dominated transport.

Table 4. Peclet numbers calculated for baseline interstitial flow velocity 0.5 µm/sec.

Condition	D_{eff} (m^2/s)	Peclet Number
40 kDa Dextran	3.5E-11	1.43
Averaged FRAP sEV D_{eff}	1.53E-12	32.68
Range from Lenzini *et al.*[70]	1.53E-13	326.8
	1.53E-14	3,268
	1.53E-15	32,680

Resulting simulation curves at T=30 min demonstrate this phenomenon with no apparent differences in free or bound concentration curves when D_{eff}<1.53E-12 m^2/s (**Fig. 25**). Comparing soluble mediator (D_{eff}=3.5E-11 m^2/s) to sEV (D_{eff}<1.53E-12 m^2/s) concentration profiles showed higher levels of both free and bound particles across all conditions. This data supports the hypothesis that convective transport of sEVs dominates diffusive transport in the interstitial space. Gradient formation of free and bound species was only apparent in cases of high K_{on} (**Fig. 25d,e**). Bound fractions were often much higher than free sEV concentrations (refer to scale of y-axes). These trends are not the result of binding site consumption, as the concentration of binding sites remains almost entirely constant as observed in previous simulations.

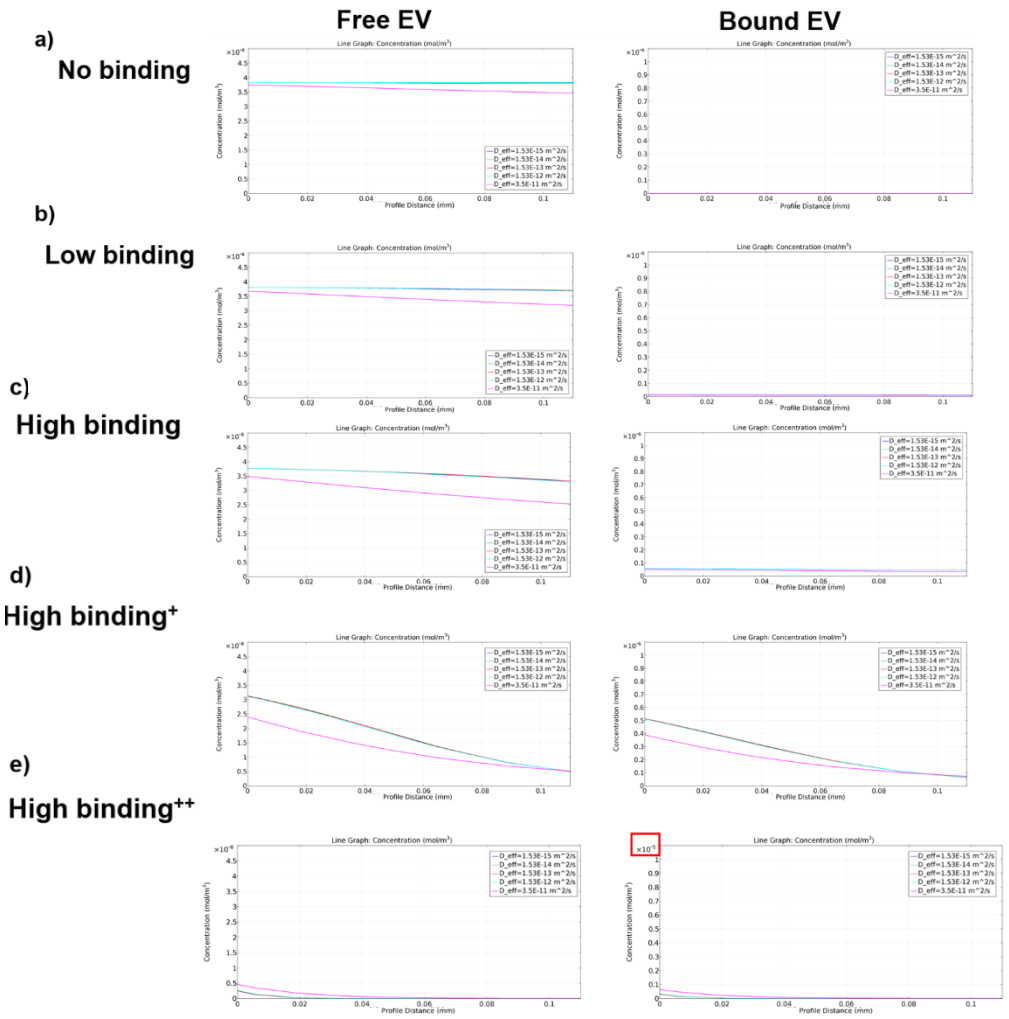

Figure 25. Small molecule soluble mediator convective transport differs from sEV transport by D_{eff} alone. a) Simulations comparing a range of sEV diffusion coefficients to small molecule soluble mediators demonstrated marginally different free sEV curves at T=30 min. b-e) Differences between small molecule soluble mediator diffusion and sEV diffusion was more apparent with increasing integrin binding avidity (note- bound sEV high binding^{++} graph y-axis is scaled differently). Differences between sEV D_{eff} curves were marginal, with most curves collapsing on identical lines.

To compare computational results to *in vitro* convective flow experiments (**Chapter 6**), computational models were initiated to approximate experimental conditions (**Table 2**). Four integrin binding states were assessed (**Table 3**; no binding through high binding^{+}), and resulting simulations evaluated free and bound sEV concentrations at T=30 min (**Fig. 26a-d**). "High binding" kinetic parameters, reflective of K_d values extracted from high binding MCF10CA1 +

$MnCl_2$ FRAP curves demonstrated clear spatial gradients which high concentration near the centerline EV-source and lower concentration near the fluidic line sink (**Fig. 26c**). “Low binding” parameters which were reflective of low binding MCF10A + $CaCl_2$ + $MgCl_2$ EV conditions as well as the “no binding” (K_{on} = 0 m^3/mol/s) conditions showed no appreciable sEV gradient formation (**Fig. 26a,b**). Line profile depictions of these curves demonstrated shallow spatial gradients for the “high binding” condition and steeper profiles when K_{on} is increased an order of magnitude (**Fig. 26g,h**). Gradients appear to be transient and approaching a constant steady state value, evident by the decreasing distance between subsequent curves from T=0-60 min. Importantly, accumulation of bound sEVs was evident, seen through increasing bound sEV curves at each time point with increasing K_{on} (**Fig. 26f-h**; right column).

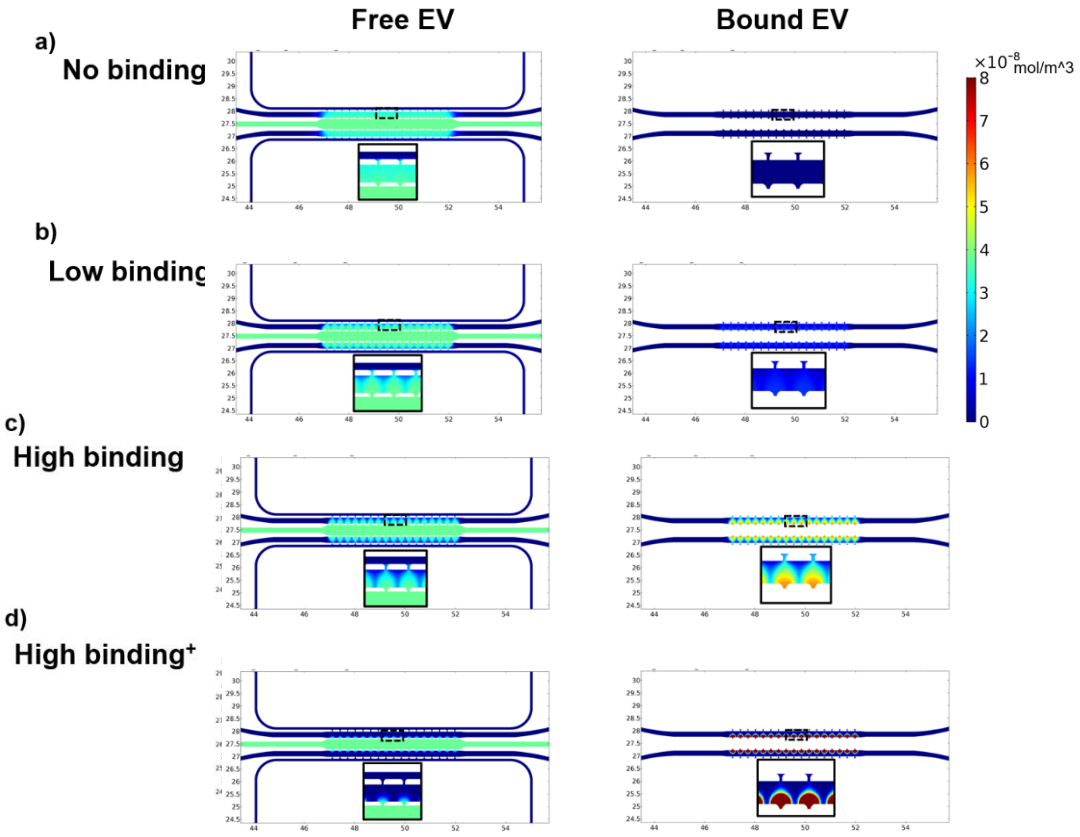

Figure 26. sEV form transient free and bound concentration gradients. a-d) Simulations were performed using all baseline modeling conditions, and assessed a range of integrin binding states. T=30min images showed the formation of free and bound sEV gradients in the interstitial compartment. (continued on next page).

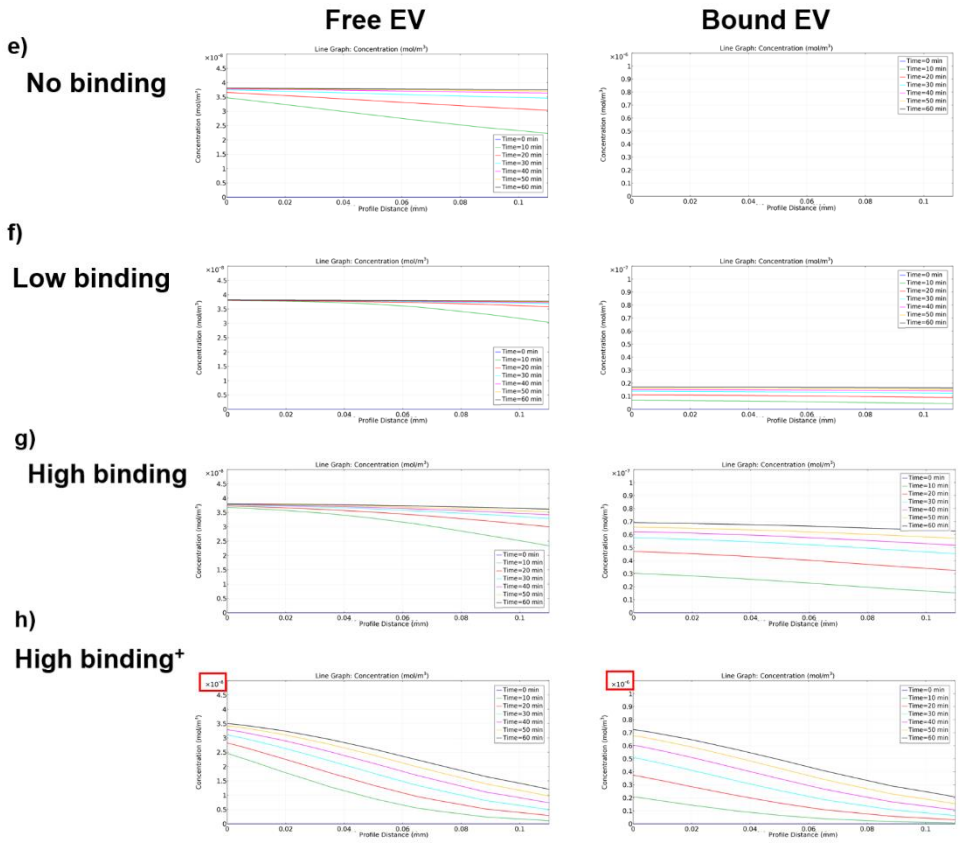

Figure 26. (continued). e-h) Concentration curves over 60 minutes demonstrated shifting shapes of the free and bound sEV curves. Only with high and high binding⁺ integrin activation were free and bound sEV gradients observed.

Chapter 6: Convective Transport of sEVs in a Microfluidic Device

To experimentally demonstrate the accumulation of sEVs and dynamic gradients in a laminin-rich ECM generated by the *in silico* model, a microfluidic approach was pursued using the same device leveraged in the FRAP diffusion experiments. Device chambers were loaded according to the following arrangement (**Fig. 27**) with pressure heads decreasing from left to right and from chamber three outwards to chambers one and five. To validate experimental interstitial flow velocity (i.e. flow through chambers two and four) to match *in silico* modeling results, fluorescently labeled 40kDa dextran was added to PBS and flowed into chamber 3. 40 kDa dextran was selected due to its small size and negligible binding to laminin-rich ECM which approximates the transport of soluble mediators that do not have the capability to bind to ECM.

Due to the heterogeneity in laminin-rich ECM loading, dextran convective transport varied port to port within individual devices (**Fig. 28a**). These variations in flow velocity were ultimately a function of differences between local permeability of matrix in each pore caused by anisotropic

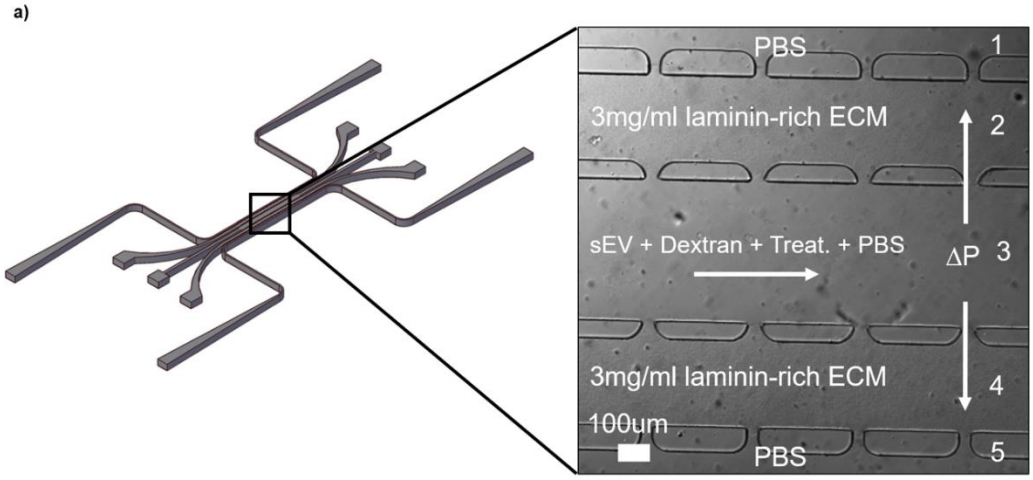

Figure 27. The experimental design to assess sEV convective flow. a) The same microfluidic platform used in diffusion studies featuring five parallel chambers (1-5) was loaded with $CTFR^{+}$ sEVs with the experimental treatment condition and FITC dextran in chamber 3. 3 mg/ml laminin-rich ECM was loaded into chambers 2 and 4. Hydrostatic pressure heads were established so flow would pass through chambers 2 and 4 at approximately 0.5 μm/sec. Devices were continuously imaged over the first ten minutes of flow to visualize dextran flow and sEV accumulation, as well as at T=30 min.

laminin-rich ECM polymerization[98]. In order to calculate the bulk fluid flow velocity within each port, the convection-diffusion equation was utilized in tandem with *in silico* simulations. These simulations were necessary to decouple dextran diffusive transport from convective transport since dextran diffusion was non-negligible at experimental flow velocities and length scales ($Pe_{dextran}$ ~ 1.5). Images were subjected to thresholding, and spatial differences in dextran fronts varied from pore to pore (notice differences in dextran concentration between the top ports (a-d) and the bottom (e-h)) (**Fig. 28a**).

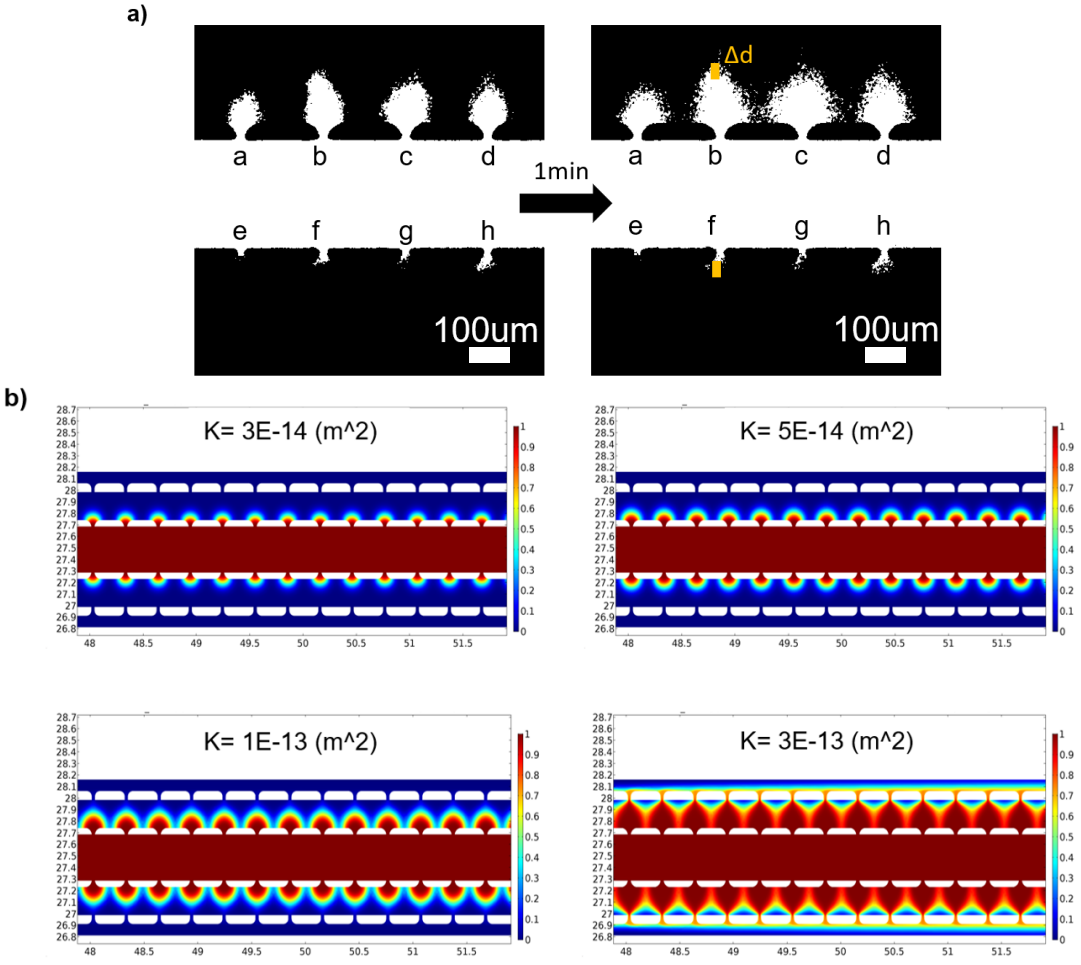

Figure 28. Interstitial fluid velocity was determined via experimental dextran flow and computational modeling. a) Fluorescent dextran profiles were thresholded and resulting representative images demonstrate the distance of dextran transport (Δd) over 1 minute. b) Simulation results using the same hydrostatic pressure head as *in vitro* experiments demonstrate increased dextran transport by increasing the permeability (K) of the ECM. (continued on next page).

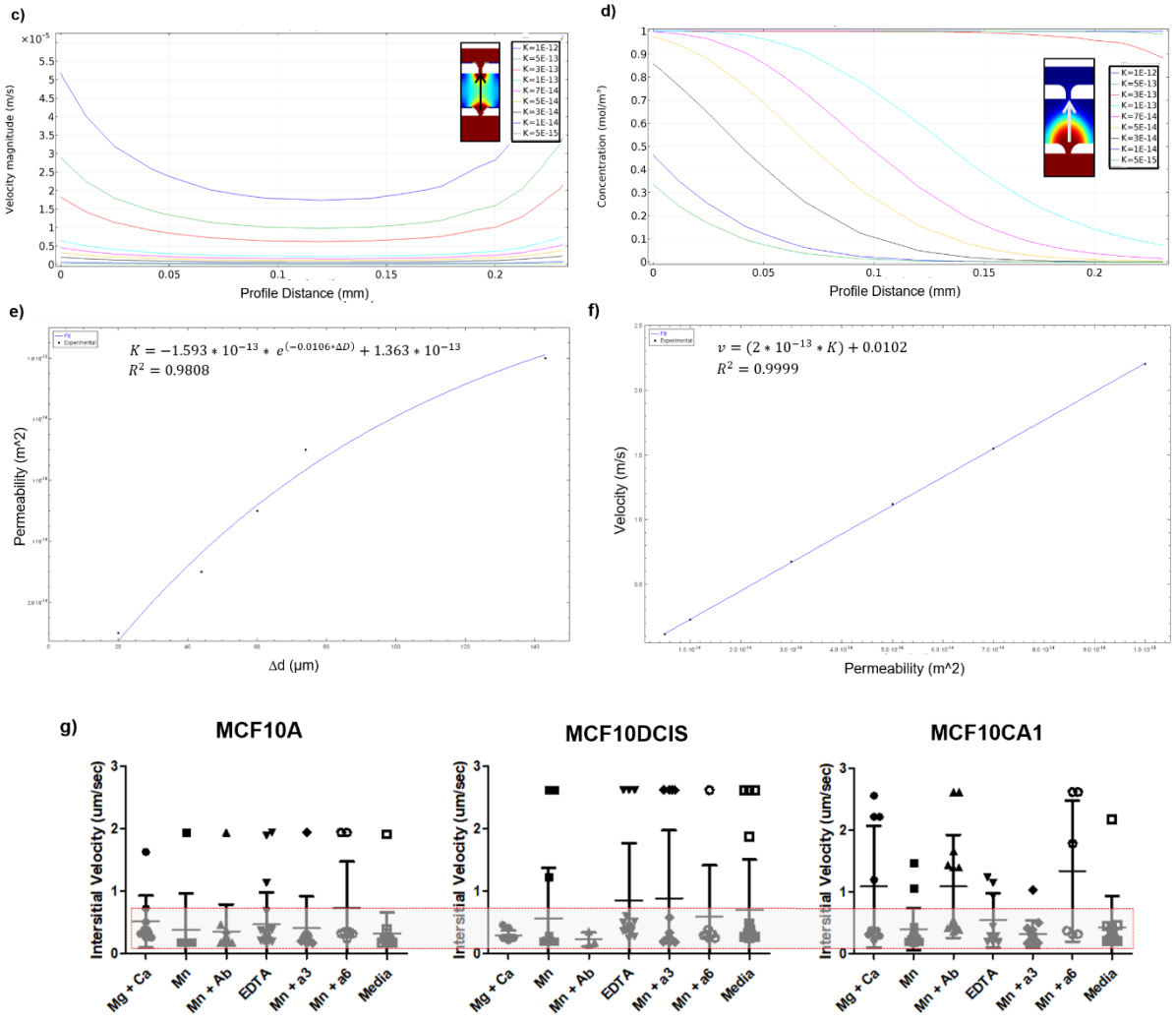

Figure 28. (continued). c) Average interstitial velocity profiles and d) concentration profiles showed the dependence of flow on ECM permeability. e) Computational Δd values were recorded and plotted against ECM permeability. A model with strong R^2 was fitted to the data to determine permeability values from experimental Δd. f) Computational permeability values were plotted against computational velocities and linearly fit. g) Across all convective flow experiments, most interstitial flow velocities were between 0-1 μm/sec. A binned interstitial flow velocity range of 0.15-0.75 μm/sec was selected for subsequent experiments.

To match experimental differences in permeability, COMSOL simulations were designed to mimic identical flow parameters with varying permeability of the ECM. As expected, increasing permeability resulted in increasing dextran transit due to increased interstitial fluid flow velocities (**Fig. 28b,c**). Assessing the transport of the simulated dextran also demonstrated increased distance travelled per unit time with increasing permeability (**Fig. 28d**). Fits were generated to

plot graphs of interstitial velocity vs. permeability as well as distance of dextran transport vs. permeability (**Fig. 28e,f**). Experimentally determined distances of dextran transport were input into these fits to determine the permeability of each pore, and subsequently the fluid flow velocity. Experimental permeabilities and flow velocities had similar variability between experimental conditions (**Fig. 28g**), but to control for the effects of bulk flow velocity on sEV binding, only pores with flow velocities between 0.15 μm/sec and 0.75 μm/sec were considered for downstream analysis to prevent biases introduced by gel breakage or gaps (and resulting high interstitial flow velocity).

Table 5. Integrin activation state assessed by each experimental convective flow experimental condition

Integrin State	Condition
Physiologic binding	EV + Ca^{2+} + Mg^{2+}
Hyper-physiologic binding	EV + Mn^{2+}
Hyper-physiologic blocked:	EV + Mn^{2+}+ Ab cocktail (α3, α6, β1, β4)
Blocked	EV + EDTA
Hyper-physiologic partial block	EV + Mn^{2+} + α3 Ab
Hyper-physiologic partial block	EV + Mn^{2+} + α6 Ab
Physiologic binding	EV + RPMI Media

sEV convective transport through laminin-rich ECM from each of the MCF10 series lines was next assessed with several integrin activity modulating conditions (**Table 5**). Device layouts mimicked *in silico* models (**Fig. 26**). Representative images after 30 minutes of flow with CTFR-labeled sEVs demonstrated clear differences in sEV transport based on parent cell malignancy and integrin activation state (**Fig. 29**). Accumulation was most apparent within the first 100μm of the laminin-rich ECM (**Fig. 29b**; white arrows). Highest sEV accumulation was observed with MCF10CA1 sEVs treated with $MnCl_2$ (**Fig. 29b**; right column), which is consistent with high binding observed in FRAP and *in silico* results. The addition of EDTA or integrin blocking antibodies (**Fig. 29c-f**) neutralized sEV accumulation, particularly with MCF10CA1 sEVs, but also for MCF10A and MCF10DCIS sEVs. Although differences in background fluorescent intensity were evident (partially due to fluorescent spill-over from highly fluorescent FITC-dextran which

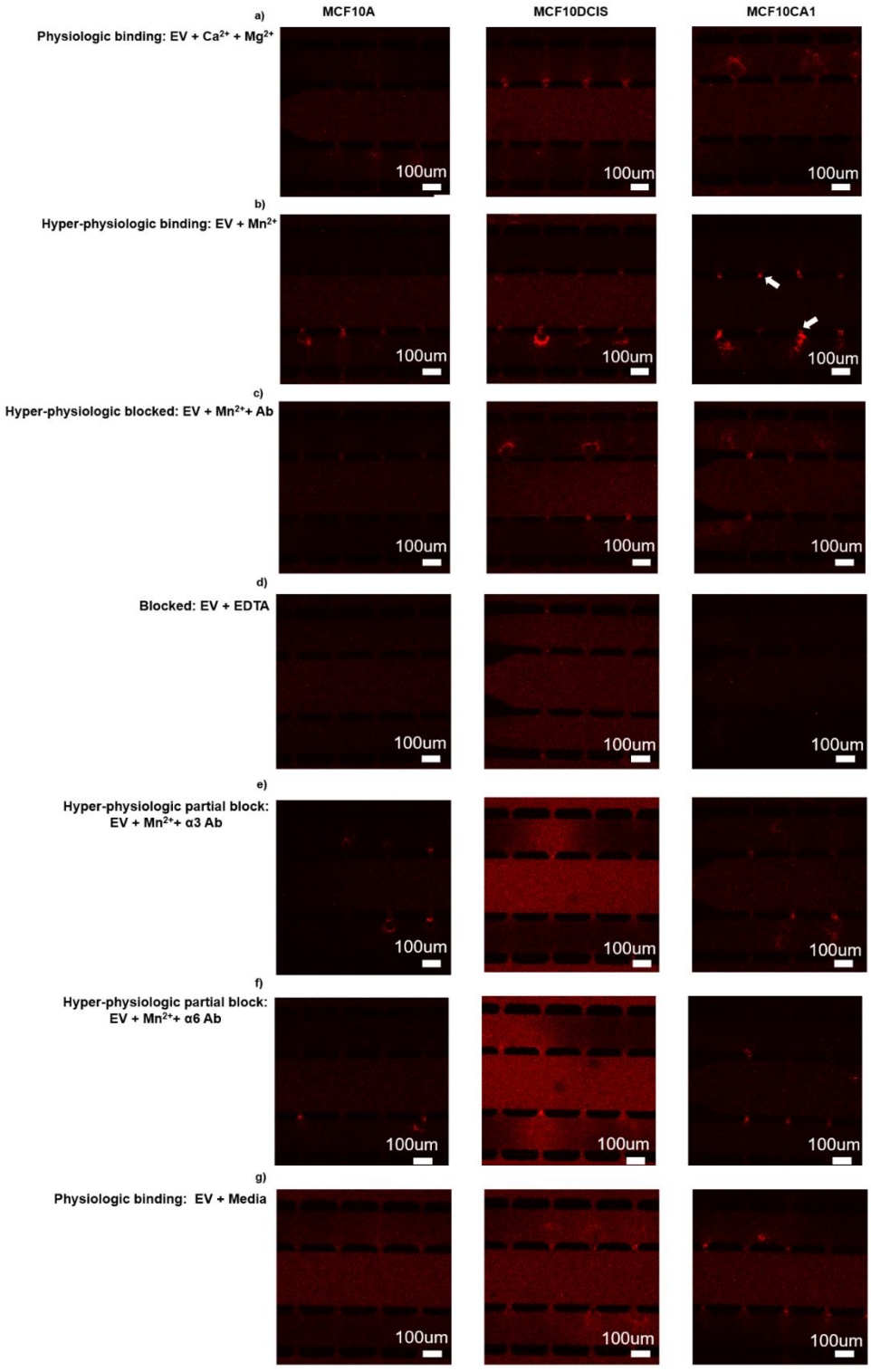

Figure 29. Representative images of devices after T=30 min of convective flow. a-g) Representative images demonstrated a range of sEV binding profiles. Most consistent high binding was observed with MCF10CA1 sEVs treated with hyper-physiologic Mn^{2+} (b, right column, white arrows). Differences in background fluorescent intensity were evident but were normalized for quantitative analysis.

was co-loaded with sEVs), quantification of sEV spatial accumulation was achieved by normalizing the fluorescent intensity in the chamber to that at the centerline (the source, chamber 3). This normalization accounts for fluorescent bleed-over as well as differences in CTFR staining efficacy described in Chapter 3.

To quantify differences between cell lines and experimental conditions, images after 10 minutes of convective flow were analyzed to incorporate fluid flow velocity into the analysis. Dextran velocity was measured for each pore, and only pores with a dextran velocity between 0.15 μm/sec and 0.75 μm/sec were included for analysis. Line profiles to measure CTFR-stained sEVs were drawn between pores (**Fig. 30a**), and resulting curves were smoothed and averaged (**Fig. 30b-h**). For all conditions, MCF10A sEVs did not form concentration gradients within the physiologic 100μm length scale. Appreciable binding and ensuing gradient were only significantly present in MCF10CA1 sEVs, and to a lesser extent MCF10DCIS sEVs, treated with $MnCl_2$ (**Fig. 30c**). In contrast, spatial concentration curves of sEVs treated with EDTA were completely flat at

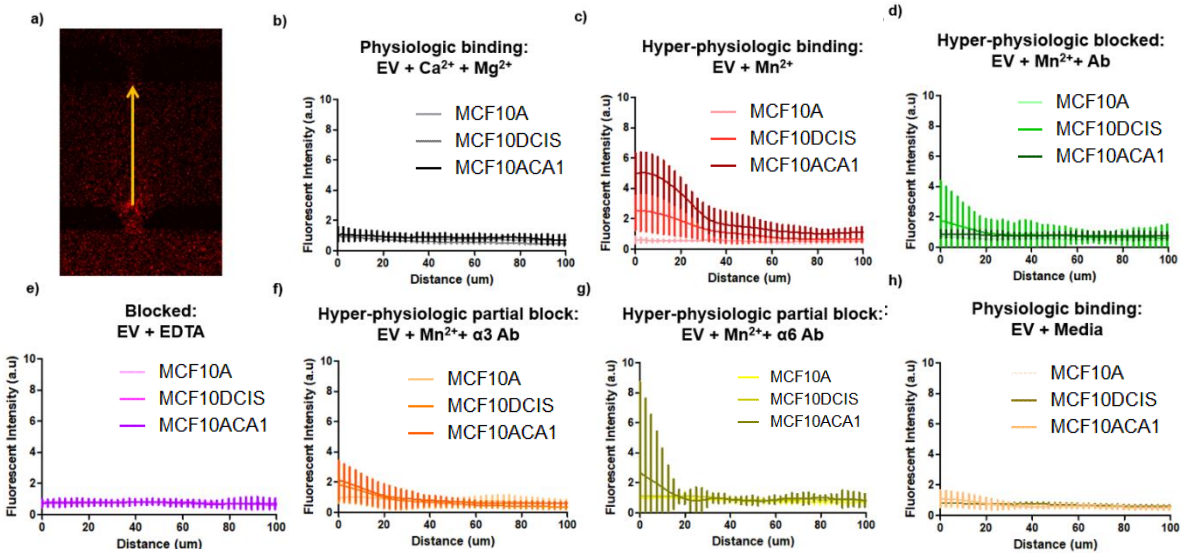

Figure 30. sEV convective transport is affected by parent cell malignancy and integrin activation state. a) Line profiles were used to assess sEV concentration after T=10 min of flow. b-h) Comparisons of concentration profiles by integrin activation state showed highest differences for hyper-physiologic MCF10CA1 and MCF10DCIS sEV binding. Blocking conditions reduced the formation of spatial gradients. Physiologic binding conditions showed minimal differences between sEV conditions. Error bars=95% CI. n=2-4 devices per curve; n=3-25 ports per curve; average ports per curve=12.

baseline values across the MCF10 series, suggesting a role of integrins in sEV binding. Although there was a slight increase in MCF10CA1 sEV binding in the physiologic sEV + media condition, differences between the curves were within the 95% confidence intervals (**Fig. 30h**). Integrin blocking antibody conditions reduced binding particularly for MCF10CA1 and MCF10DCIS sEVs (**Fig. 30d,f,g**).

To further investigate the effect of integrin blocking antibodies, sEV concentration curves were plotted on the basis of parent cell line for select conditions (**Fig. 31**). MCF10A sEVs showed no appreciable difference in sEV concentration, while MCF10DCIS sEVs showed a trend of higher binding in the $MnCl_2$ and $MnCl_2$ + integrin blocking antibody conditions (**Fig. 30a**; left and middle columns). Only in the MCF10CA1 sEV curves was the effect of integrin antibody blocking significant (**Fig. 30a**; right column). Assessing the effects of individually blocking α3 and α6 integrin subunits revealed decrease in the spatial gradient for MCF10CA1 sEVs for each blocking condition (**Fig. 30b**; right column). Trends for MCF10A and MCF10DCIS sEVs were not evident due to the high noise in the curves. In aggregate, these data indicate that sEVs in a physiologic state will not form appreciable interstitial gradients due to integrin binding alone, but binding does result in an accumulation of sEVs in the matrix. This is particularly evident when comparing sEVs from each cell line to the physiologic sEV + media control (**Fig. 30c**), which shows similarly low levels of sEV spatial gradient. These data are consistent with both the *in silico* results presented in Chapter 5 as well as the t=30 minute representative images (**Fig. 29**).

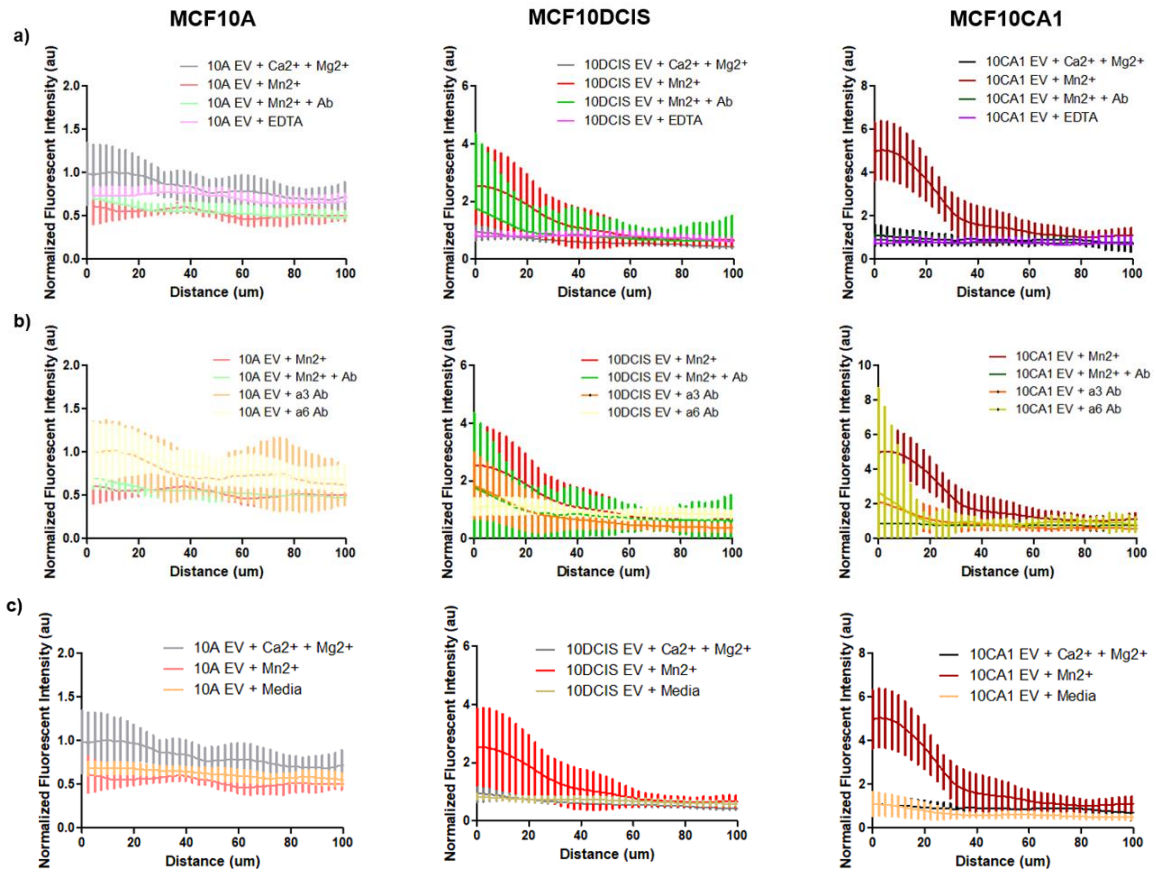

Figure 31. sEV convective transport is affected by integrin activation state. a) Physiologic, hyper-physiologic, and blocking conditions were plotted for each cell lines. Unique y-axes were selected to highlight differences within cell lines. MCF10CA1 hyper-physiologic binding curves generated gradients above blocking controls, while MCF10DCIS curves followed a similar, albeit, noisier trend. Concentration profiles were plotted to compare b) blocking and partial blocking conditions as well as c) physiologic binding conditions. Error bars=95% CI. n=2-4 devices per curve; n=3-25 ports per curve; average ports per curve=12.

Chapter 7: Discussion and Conclusion

In this body of work, we explored how sEV interstitial transport changes with malignant cancer progression, the relative importance of sEV convective and diffusive transport, and the impact and mechanism of sEV binding to the ECM. We hypothesized that sEVs are transported predominantly by convection through the interstitium where accumulation and the formation of a spatial gradient occurs, in part, via sEV binding to laminin through integrins α3β1 and α6β1 expressed on sEVs. Further, we hypothesized transport is altered over the course of malignant progression, with sEVs from more malignant parent cells accumulating to higher concentrations and forming steeper bound gradients in the interstitium due to the increased presence of laminin binding integrins on those sEVs. Examining the data presented holistically, it is evident this hypothesis can be partially accepted while some claims must be reassessed. In summary, sEV integrin expression and colocalization on single sEVs increases with malignant progression. sEV diffusive transport is negligible compared to convective transport, and binding to the extracellular matrix (and thus net transport) is altered by the malignant potential of the parent cell. However, differences in net transport cannot be fully attributed to differences in α3β1 and α6β1 integrin expression and binding. Further, while the physiologic interstitial spatial gradients that are established *in silico* and *in vitro* are shallow and transient, sEV accumulation is increased with higher binding sEVs from malignant parent lines.

Arriving at these conclusions required confidence that that sEV isolation procedure could successfully yield purified, and fluorescently labeled sEVs. NTA and TEM results indicate successful isolation of sEV populations, and at a sufficiently high concentration for *in vitro* experiments. sEV concentrations increased with increasing parent cell malignancy which is consistent with literature suggesting that sEV secretion is impacted by microenvironmental features like hypoxia and acidic pH as well as internal signaling through Wnt and STAT3 pathways[29,119,120]. While it is unclear exactly why MCF10CA1 cells secreted higher levels of sEVs,

observations made during routine culture showed these cells grew comparably faster and depleted culture medium quicker (apparent by pH indicator in media) than MCF10A and MCF10DCIS lines. Improving sEV yield in future experiments is a necessary step to reach the yields required for BCA and western blotting. The use of larger culture flasks or bioreactors could meet this need and would allow for more robust bulk analysis of sEV isolates.

Isolated sEV populations expressed a range of tetraspanins, which along with NTA and TEM results, suggest the isolation of exosomes. Tetraspanin presence was heterogeneous across the MCF10 series, and highlights the accepted trend that tetraspanin presence is not uniform across cell populations[121,122]. All lines had the highest levels of surface bound CD9, which serves as the best tetraspanin marker (of those assessed) to identify MCF10 series sEVs, and would be the ideal candidate for a fluorescent fusion protein to identify MCF10 series sEVs. Staining of sEVs with CTFR was pursued in this study rather than a fluorescent fusion protein approach, and demonstrated successful staining of sEV populations. Staining was lower for MCF10DCIS sEVs, but downstream experiments were normalized based off of the fluorescent intensity of background signal which should minimize staining biases. Further, visualization of sEVs was apparent via confocal microscopy, although it was not possible to determine whether observations were for single sEVs or multiple due to sEV diameters smaller than emitted wavelengths. Importantly, a fluorescent intensity dose-dependent response was observed by increasing sEV concentrations which supported the conclusion that signal was due to sEVs and provided an approximate noise baseline concentration of 2E8 EVs.

Analysis of integrin presence on sEVs via ExoView supported our hypothesis that the more malignant MCF10CA1 sEVs possessed higher levels of laminin binding integrins α3, α6, and β1. Western blots did not detract from this conclusion, but the inability to perform BCA, and thus inability to load equal numbers of sEVs (based off of protein concentration) per MCF10 line, prevents further analysis of the blots. At the minimum, these blots do demonstrate the presence of laminin binding integrins on bulk sEVs from the MCF10CA1 line, with some expression on

MCF10A and MCF10DCIS lines. Improved sEV yield will be required to perform more robust blots. A key advantage of the ExoView methodology, however, is the ability to assess single sEV protein expression even with dilute samples. Colocalization analyses revealed increasing integrin colocalization on increasingly malignant sEVs, and the percentage of sEVs with colocalized integrins was nonnegligible (~20-40% for MCF10CA1 sEVs). This indicates that not only are there more MCF10CA1 sEVs secreted per unit cell, but on a per sEV basis, more MCF10CA1 sEVs have the integrin pairs necessary to bind laminin ECM. Subsequent *in vitro* experiments loaded the same concentration of sEVs per experimental condition; however, differences in how these lines may behave *in vivo* could be due to the increased baseline secretion of sEVs as well as integrin expression as malignant potential increases.

sEV diffusion was first assessed with a particle tracking methodology since other groups have demonstrated success in tracking sEVs[70] . Although sEVs were successfully tracked with this technique, and integrin blocking antibody conditions reduced the number of bound sEVs for MCF10CA1 and MCF10DCIS conditions, these results are limited by the ability to resolve with certainty single sEVs. Measured diffusion coefficients were an order of magnitude lower than what they would have been for a theoretical 100 nm particle diffusing in water, which may be due to biased tracking of larger diameter sEVs or the retardation effects of the matrix on effective diffusion. To overcome these limitations, analysis of sEV diffusion in bulk via FRAP analysis was performed. The selected fitting equation[106] permitted the ability to extract not just diffusion coefficients from the curves, but also kinetic binding parameters K_{on} and K_{off}. The model generally fit the raw data curves well, although sum of squares residual surface plots demonstrated an acknowledged limitation in the original paper[106] that there was lower certainty in identifying K_{on} and K_{off}. The long trough of minimums in the residual plots (**Fig. 15b**) suggest multiple combinations of K_{on} and K_{off} can fit the data. In fact, it is the ratio of K_{off}/K_{on}, or K_d, which can be uniquely identified. Calculated K_d values of approximately 5E-3 mol/m^3 equates to 5000nM, which is several orders of magnitude higher than SPR-measured α3β1 and α6β1 binding to laminin

domains[123]. These results are consistent with the additional drag forces on an sEV which would act to dissociate integrin-laminin binds. Experimental K_d values additionally are a measure of avidity rather than affinity, and thus should be carefully compared. Regardless, to our knowledge, this is the first presentation of sEV kinetic binding parameters to a 3D ECM matrix, and the first to do so using FRAP methodology.

Resulting fitted FRAP curves demonstrated reduced net diffusive transport for MCF10CA1 sEVs. The dissociation constant K_d was lower for MCF10CA1 across all conditions, and the bound fraction C_{eq} was likewise higher. Step-wise decreases in K_d (and increase in C_{eq}) where MCF10A<MCF10DCIS<MCF10CA1 were only apparent in the hyper-physiologic binding condition, which may suggest that integrins on sEVs at physiologic ionic levels are minimally active, or there may be a critical concentration of integrins necessary to achieve measurable binding. This could partially explain why integrin blocking experiments (**Fig. 21**) did not result in statistically significant differences across most of the experimental conditions. If sEV integrins are unactive at physiologic ionic conditions, or below a critical concentration on the sEV, this would have significant implications for the field's understanding of sEV-integrin relationships and binding. The studies performed here were insufficient to fully assess this position, and would therefore require future studies to support this postulate. More likely, the noisiness inherent in FRAP data was compounded by the fact that MCF10 sEV populations have heterogeneous integrin expression, and resulting differences in the curves could not be extracted.

Additional extraneous variables which could have a profound impact on diffusive transport but were not assessed include the effects of matrix pore size, the possibility of incomplete blocking with integrin-blocking antibodies, and dim baseline fluorescent signal. Pore sizes in laminin-rich ECM are 1-5 μm in diameter[124–127] which is an order of magnitude larger than sEV diameter and thus should not considerably impact sEV transport. Alternatively, laminin-rich ECMs appeared anisotropic and likely had varying pore diameters throughout the bulk matrix which may have impacted sEV diffusion in some instances. Future experiments with a wider range of integrin

blocking antibodies as well as titrating an effective dose would improve certainty with blocking. Improving sEV fluorescent signal via fluorescent transgenes or brighter fluorophores, such as quantum dots, would likely improve signal to noise.

Although not explicitly discussed to this point, computational models were iteratively built with *in vitro* experimental tests. Hydrostatic pressure heads, laminin rich ECM permeability, interstitial flow velocities, EV influx concentration, and free and effective sEV diffusion coefficients were determined through this iterative process. The concentration of laminin binding sites in laminin rich ECM was likely in excess in relation to the number of sEVs introduced to the system, resulting in effectively an unlimited sink of binding sites. Simulations with higher levels of initial free sEVs resulted in higher levels of bound sEVs (**Fig. 22**; right column), which suggests MCF10CA1 sEVs would inherently reach higher bound concentrations in the matrix due to higher levels of secretion. Including higher rates of binding (lower K_d) further increases bound concentration. This data directly supports the hypothesis that more malignant sEVs may reach higher concentrations in the TME, and due to the numerous interactions between sEVs and target cells[33,36,41,128], malignant sEVs may be able to more effectively alter recipient cell phenotype.

Modeling results also highlighted the differences in transport between sEVs and small molecule soluble mediators. Point source diffusion experiments demonstrated that diffusion coefficients less than the approximate experimentally determined D_{eff} of a 100 nm sEV (D=1.53E-12 m^2/s) have similar spatial profiles, compared to profiles of more quickly diffusing small molecule soluble mediators. Considering Peclet numbers calculated over a physiologic characteristic length (100 μm) and flow velocity (0.5 μm/sec) resulted in values of Pe~30 for 100nm particles (values that only become larger with decreasing D_{eff}), it becomes clear that interstitial sEV transport is perfusion-limited. Varying convective flow velocity further demonstrates the sEVs are primarily transported by convection in support of our hypothesis. As expected, increasing convective flow velocity removes bound and soluble gradients more rapidly than slower flow velocities.

General agreement between updated computational models and experimental results were observed with the exception of the shape of the bound sEV gradient between models (**Fig. 26**) and *in vitro* device experiments (**Fig. 30**). Computational results indicate the presence of shallow free and bound sEV gradients at T=30 min. Concentrations are an order of magnitude higher for bound sEV fractions compared to free fractions in most parameter sweeps, and bound gradients became steeper by increasing K_{on} (decreasing K_d). *In vitro* convective flow device experiments did not precisely match these trends. These discrepancies could be due to improper experimental calculation of sEV kinetic binding parameters, but is more likely due to limitations in the design (or assumptions) of the computational model. For example, the model was designed to treat sEVs as dilute dissolved solutes with no mass or size, and would thus not experience drag forces or steric interactions within the ECM pore geometry. Generating computational models that treat sEVs as physical particles may reconcile these differences and would serve as reasonable next steps.

In vitro experiments with microfluidic platforms provided the ability to regulate fluid flows and assess sEV convective transport. Interstitial gradients were significantly present only in hyper-physiologic binding conditions, and were most obvious with MCF10CA1 sEVs. These gradients were ablated with 5mM EDTA, and reduced with functionally inhibitory integrin blocking antibodies. Physiologic binding conditions resulted in shallow or negligible gradients. Although physiologic gradients were shallow, immune cell migration can be impacted by very small concentration gradients. Neutrophils are capable of responding to concentration differences that are only 1% different over the cell length[129], which suggests cells in the interstitium may still respond to shallow sEV gradients.

Nonetheless, low visible gradients again raise the possibility that although sEV have integrins capable of binding, without outside-in integrin signaling (through the addition of Mn^{2+}), they are unlikely to bind ECM through those integrins. This is apparent even in the sEV + cell culture media condition, where only a slight spatial gradient is apparent for MCF10CA1 sEVs.

Limitations regarding sEV brightness versus the detection limit as well as a heterogeneous sEV population prevent strong support of this argument. Future studies to assess this claim would include longer time courses of sEV flow which may establish more concentrated gradients and assess a steady state concentration, varying ECM pore size, and introducing sEVs with a brighter fluorescent signal to reduce background noise.

In conclusion, the results of this study demonstrate that sEV interstitial transport changes with malignant progression. sEVs from increasingly malignant cells have increasing binding to laminin-rich ECM, and also have higher levels of colocalized laminin-binding integrins. However, the presence of integrins can only account for part of the differences in sEV ECM binding. The data demonstrated consistently increased binding and bound fraction for sEVs from malignant MCF10CA1 parent cells. Computational studies confirmed the hypothesis that sEV transport is perfusion-limited and dominated by convective flow, while also highlighting the fact that sEVs with higher binding avidities result in increased bound fractions. This has direct implications for impacting cell phenotype in the tumor microenvironment, since significantly more malignant sEVs may be sequestered within the ECM due to both a higher rate of sEVs secretion and enhanced binding to the ECM. While computational and experimental results indicated that only shallow gradients could be established with physiologic binding parameters, future studies may reveal these shallow gradients are functional due to high chemotactic sensitivity characteristic to many immune cell populations.

Taken together, these studies advance our fundamental understanding of how the TME evolves over the course of malignant progression. Due to the wide range of phenotypic responses sEVs can elicit from recipient cells, understanding the dynamic spatial distributions of sEVs in the interstitial microenvironment is critical. This data also improves the understanding of how nanoparticles, in general, may be transported in the TME, as well as what level of binding avidity is needed to impact the bound concentration in the ECM. These results add to our functional

understanding of sEVs in the TME and could be leveraged to not only identify new targets for early-stage disease, but also to design novel nanoparticle therapeutics that target the TME.

Chapter 8: Future Directions

Immune cell phenotypic response to sEVs was a major initial focus of this work, but became a secondary priority to allow for robust exploration of sEV interstitial transport. The following future studies expand on the theme of monocyte chemotaxis to developing breast tumors, and present realistic future directions for this body of work. We hypothesized that sEVs may serve as a novel mechanism for monocyte recruitment to DCIS.

Monocytes are circulating phagocytes of the innate immune system capable of extravasating the vasculature and differentiating into macrophages and dendritic cells. They are commonly divided into three distinct subsets by CD14 and CD16 expression, each with unique phenotypic and functional properties. Although the patrolling monocyte (PMo) subset only comprises 10% of circulating monocytes[130], evidence suggests the PMo subset may play a pivotal role in breast cancer. In homeostatic conditions, PMos characteristically patrol the vascular lumen, and play a role in tissue surveillance and disposal of damaged endothelial cells[131,132]. In pathologic conditions, PMos are one of the first immune responders to infection, and can extravasate the vasculature to reach target tissues[131,133]. PMos engulf tumor debris more efficiently than classical monocytes to prevent breast cancer metastatic seeding in autochthonous murine models[133,134]. In human breast cancer, circulating PMo fractions in patients suffering from early stage disease are expanded 1.5-3 fold and express an altered phenotype compared to healthy patient controls[135,136]. In murine models, PMos are also preferentially recruited over classical monocytes to autochthonous late-stage Polyoma Middle T (PyMT) mammary tumors[137]. Furthermore, in a murine model comparing the effects of EVs from pre-metastatic melanoma and metastatic melanoma, it was shown that PMos uptake both EV populations, but only pre-metastatic derived EVs resulted in an increased PMo population in the lung and a protective PMo phenotype that reduced lung metastasis[138]. Taken together, this evidence warrants investigation into sEV interstitial distribution under physiologic flow conditions and its effects on PMo migration

in a model of human pre-malignant breast cancer. This study would reveal a novel mechanism of immune recruitment to primary tumors which could be leveraged to develop novel therapies in early stages of breast cancer.

We hypothesize that an inflamed post-capillary venule endothelium facilitates PMo arrest via LFA1-ICAM1 and ICAM2 interactions, enabling the extravasation of PMos. Transmigrated PMos respond to a DCIS secreted sEV gradient and migrate up the gradient towards the primary tumor in response to sEV membrane bound CX3CL1. ICAM-1 and ICAM-2 are expressed on inflamed endothelium and are critical for the PMo crawling phenotype via LFA-1 interactions[133]. PMos express high levels of CX3CR1 and are responsive to the chemoattractant CX3CL1[139]. Endothelial cell membrane bound CX3CL1 facilitates PMo interaction with endothelial cells[133], while soluble CX3CL1 functions as a potent chemoattractant[139]. CX3CL1 is also expressed on the MCF10 series (**Fig. 33**) and is expressed on primary human mammary epithelial cell sEVs[79]. We propose that PMos are responsive to an interstitial sEV gradient and do so through cell-surface interactions between CX3CR1 and sEV bound CX3CL1.

Preliminary experiments demonstrated differential THP-1 monocyte migration in response to MCF10 series sEVs (**Fig. 32**). $2x10^9$ sEV/ml were added to the bottom of a 5µm pore transwell assay with THP-1 monocytes on top, and migration was assessed over the course of a five-hour experiment. Differential migration was observed with highest monocyte migration in response to malignant MCF10CA1 sEVs, and similar levels of migration with MCF10A and MCF10AT sEVs (note-MCF10AT is an alternative pre-malignant breast cancer line derived from MCF10A, and was used because the MCF10DCIS cell line was not available at

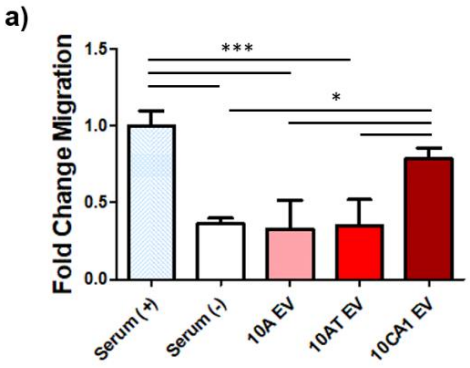

Figure 32. MCF10 series sEVs influence monocyte chemotaxis. a) Increasing THP-1 migration was observed in response to sEVs from the malignant MCF10CA1 line compared to normal MCF10A and pre-malignant MCF10AT sEVs. *p<0.05, ***p<0.001; One-way Anova, Tukey post-hoc.

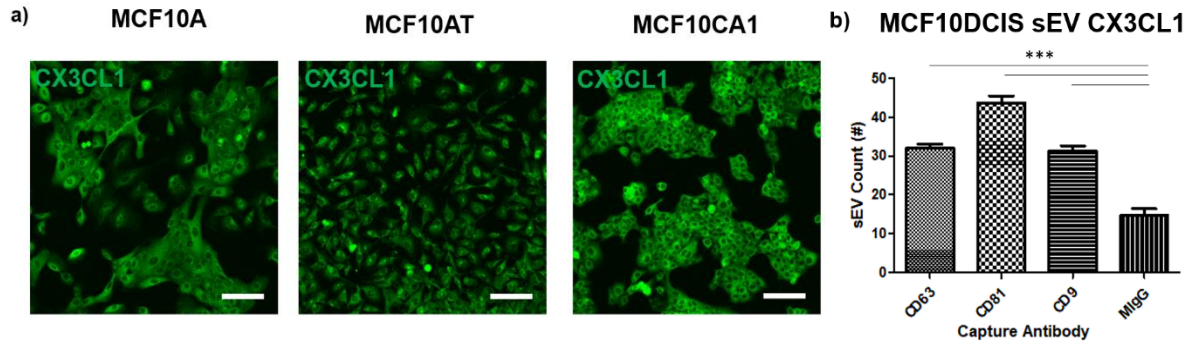

Figure 33. The MCF10 series expresses CX3CL1. a) Immunofluorescent images of normal MCF10A, pre-malignant MCF10AT, and malignant MCF10CA1 cells express CX3CL1. Scalebars=100μm. b) ExoView analysis of MCF10DCIS sEVs reveals low, but statistically significant presence of CX3CL1 compared to MIgG controls. ***p<0.001; One-way Anova, Tukey post-hoc.

the time of this experiment). Interestingly, migration towards MCF10A and MCF10AT sEVs was comparable to negative serum free media controls, warranting future studies to determine how sEVs are affecting monocyte migratory phenotype.

The presence of CX3CL1 was validated on the MCF10A, MCF10AT, and MCF10CA1 series via immunofluorescence (**Fig. 33a**); the MCF10DCIS cell line was not available at the time of this experiment to assess the presence of surface CX3CL1. It is also reported that CX3CL1 is expressed on primary human mammary epithelium[79], consistent with our premise that MCF10 series-derived sEVs contain membrane bound CX3CL1. Preliminary ExoView experiments were performed on the MCF10DCIS fraction and revealed low, but statistically significant levels of membrane-bound CX3CL1 on the sEV surface (**Fig. 33b**). Future studies would likely assess the presence of alternative chemokines such as CCL2, a more general monocyte chemoattractant, to further understand the chemotactic potential of cancer-derived sEVs in the TME. These data serve as proof of principle that MCF10 series sEVs influence monocyte migration, and may do so through chemokine receptor pairs such as CX3CL1 and CX3CR1.

References

1. Wong, C. H., Siah, K. W. & Lo, A. W. Estimation of clinical trial success rates and related parameters. *Biostatistics* **20**, 273–286 (2019).
2. Quail, D. F. & Joyce, J. A. Microenvironmental regulation of tumor progression and metastasis. (2013). doi:10.1038/nm.3394
3. Saini, K. S. & Twelves, C. Determining lines of therapy in patients with solid cancers: a proposed new systematic and comprehensive framework. *British Journal of Cancer* **125**, 155–163 (2021).
4. Miller, K. D. *et al.* Cancer treatment and survivorship statistics, 2019. *CA. Cancer J. Clin.* caac.21565 (2019). doi:10.3322/caac.21565
5. Hanahan, D. & Weinberg, R. A. Hallmarks of cancer: The next generation. *Cell* **144**, 646–674 (2011).
6. Hanahan, D. Hallmarks of Cancer: New Dimensions. *Cancer Discovery* **12**, 31–46 (2022).
7. Falzone, L., Salomone, S. & Libra, M. Evolution of cancer pharmacological treatments at the turn of the third millennium. *Frontiers in Pharmacology* **9**, (2018).
8. Collins, I. & Workman, P. New approaches to molecular cancer therapeutics. *Nature Chemical Biology* **2**, 689–700 (2006).
9. Sun, L. *et al.* Clinical efficacy and safety of anti-PD-1/PD-L1 inhibitors for the treatment of advanced or metastatic cancer: a systematic review and meta-analysis. *Sci. Rep.* **10**, (2020).
10. June, C. H., O'Connor, R. S., Kawalekar, O. U., Ghassemi, S. & Milone, M. C. CAR T cell immunotherapy for human cancer. *Science (80-.).* **359**, 1361–1365 (2018).
11. Sanmamed, M. F. & Chen, L. A Paradigm Shift in Cancer Immunotherapy: From Enhancement to Normalization. *Cell* **175**, 313–326 (2018).
12. Lawson, D. A., Kessenbrock, K., Davis, R. T., Pervolarakis, N. & Werb, Z. Tumour heterogeneity and metastasis at single-cell resolution. *Nat. Cell Biol.* (2018). doi:10.1038/s41556-018-0236-7
13. Quail, D. F. & Joyce, J. A. Microenvironmental regulation of tumor progression and metastasis. *Nature Medicine* **19**, 1423–1437 (2013).
14. Binnewies, M. *et al.* Understanding the tumor immune microenvironment (TIME) for effective therapy. *Nat. Med.* **24**, 541–550 (2018).
15. Laplane, L., Duluc, D., Larmonier, N., Pradeu, T. & Bikfalvi, A. The Multiple Layers of the Tumor Environment. *Trends in Cancer* **4**, 802–809 (2018).
16. Baghban, R. *et al.* Tumor microenvironment complexity and therapeutic implications at a glance. *Cell Communication and Signaling* **18**, (2020).
17. Lim, B., Woodward, W. A., Wang, X., Reuben, J. M. & Ueno, N. T. Inflammatory breast cancer biology: the tumour microenvironment is key. *Nature Reviews Cancer* **18**, 485–499 (2018).
18. Keren, L. *et al.* A Structure Tumor-Immune Microenvironment in Triple Negative Breast Cancer Revealed by Multiplexed Ion Beam imaging. *Cell* **174**, 1373–1387 (2018).
19. Cox, T. R. The matrix in cancer. *Nature Reviews Cancer* **21**, 217–238 (2021).
20. Fridman, W. H., Zitvogel, L., Sautès-Fridman, C. & Kroemer, G. The immune contexture in cancer prognosis and treatment. *Nature Reviews Clinical Oncology* **14**, 717–734 (2017).
21. Kalluri, R. The biology and function of fibroblasts in cancer. *Nature Reviews Cancer* **16**, 582–598 (2016).
22. Dewhirst, M. W. & Secomb, T. W. Transport of drugs from blood vessels to tumour tissue. *Nature Reviews Cancer* **17**, 738–750 (2017).

23. Dranoff, G. Cytokines in cancer pathogenesis and cancer therapy. *Nature Reviews Cancer* **4**, 11–22 (2004).
24. Atretkhany, K. S. N., Drutskaya, M. S., Nedospasov, S. A., Grivennikov, S. I. & Kuprash, D. V. Chemokines, cytokines and exosomes help tumors to shape inflammatory microenvironment. *Pharmacology and Therapeutics* **168**, 98–112 (2016).
25. Duan, Q., Zhang, H., Zheng, J. & Zhang, L. Turning Cold into Hot: Firing up the Tumor Microenvironment. *Trends in Cancer* **6**, 605–618 (2020).
26. Kalluri, R. The biology and function of exosomes in cancer. *J. Clin. Invest.* **126**, 1208–1215 (2016).
27. Whiteside, T. L. Tumor-Derived Exosomes and Their Role in Cancer Progression. in *Advances in Clinical Chemistry* **74**, 103–141 (2016).
28. Benito-Martin, A., Di Giannatale, A., Ceder, S. & Peinado, H. The new deal: A potential role for secreted vesicles in innate immunity and tumor progression. *Frontiers in Immunology* **6**, (2015).
29. Becker, A. *et al.* Extracellular Vesicles in Cancer: Cell-to-Cell Mediators of Metastasis. *Cancer Cell* **30**, 836–848 (2016).
30. Melo, S. A. *et al.* Cancer Exosomes Perform Cell-Independent MicroRNA Biogenesis and Promote Tumorigenesis. *Cancer Cell* (2014). doi:10.1016/j.ccell.2014.09.005
31. Wolfers, J. *et al.* Tumor-derived exosomes are a source of shared tumor rejection antigens for CTL cross-priming. *Nat. Med.* **7**, 297–303 (2001).
32. Szczepanski, M. J., Szajnik, M., Welsh, A., Whiteside, T. L. & Boyiadzis, M. Blast-derived microvesicles in sera from patients with acute myeloid leukemia suppress natural killer cell function via membrane-associated transforming growth factor-β1. *Haematologica* **96**, 1302–1309 (2011).
33. Brown, M. *et al.* Lymphatic exosomes promote dendritic cell migration along guidance cues. *J. Cell Biol.* **217**, 2205–2221 (2018).
34. Gao, L. *et al.* Tumor-derived exosomes antagonize innate antiviral immunity. *Nat. Immunol.* **19**, 233–245 (2018).
35. Chow, A. *et al.* Macrophage immunomodulation by breast cancer-derived exosomes requires Toll-like receptor 2-mediated activation of NF-κ B. *Sci. Rep.* (2014). doi:10.1038/srep05750
36. Marton, A. *et al.* Melanoma cell-derived exosomes alter macrophage and dendritic cell functions in vitro. *Immunol. Lett.* **148**, 34–38 (2012).
37. Valenti, R. *et al.* Human tumor-released microvesicles promote the differentiation of myeloid cells with transforming growth factor-β-mediated suppressive activity on T lymphocytes. *Cancer Res.* **66**, 9290–9298 (2006).
38. Chalmin, F. *et al.* Membrane-associated Hsp72 from tumor-derived exosomes mediates STAT3-dependent immunosuppressive function of mouse and human myeloid-derived suppressor cells. *J. Clin. Invest.* **120**, 457–471 (2010).
39. Song, X. *et al.* Cancer cell-derived exosomes induce mitogen-activated protein kinase-dependent monocyte survival by transport of functional receptor tyrosine kinases. *J. Biol. Chem.* **291**, 8453–8464 (2016).
40. Lima, L. G. *et al.* Tumor microenvironmental cytokines bound to cancer exosomes determine uptake by cytokine receptor-expressing cells and biodistribution. *Nat. Commun.* **12**, (2021).
41. O'Brien, K. *et al.* Exosomes from triple-negative breast cancer cells can transfer phenotypic traits representing their cells of origin to secondary cells. *Eur. J. Cancer* **49**, 1845–1859 (2013).
42. Sung, B. H. & Weaver, A. M. Exosome secretion promotes chemotaxis of cancer cells. *Cell Adhes. Migr.* **11**, 187–195 (2017).
43. Majumdar, R., Tavakoli Tameh, A. & Parent, C. A. Exosomes Mediate LTB4 Release

during Neutrophil Chemotaxis. *PLoS Biol.* **14**, (2016).
44. Török, N. J. Extracellular vesicles and ceramide: New mediators for macrophage chemotaxis? *J. Lipid Res.* **57**, 157–158 (2016).
45. Kakazu, E., Mauer, A. S., Yin, M. & Malhi, H. Hepatocytes release ceramide-enriched pro-inflammatory extracellular vesicles in an IRE1 α -dependent manner. *J. Lipid Res.* **57**, 233–245 (2016).
46. Silva, T. A. *et al.* AHNAK enables mammary carcinoma cells to produce extracellular vesicles that increase neighboring fibroblast cell motility. *Oncotarget* **7**, 49998–50016 (2016).
47. Gutkin, A. *et al.* Tumor cells derived exosomes contain hTERT mRNA and transform nonmalignant fibroblasts into telomerase positive cells. *Oncotarget* **7**, 59173–59188 (2016).
48. Rilla, K. *et al.* Extracellular vesicles are integral and functional components of the extracellular matrix. *Matrix Biology* **75**–**76**, 201–219 (2019).
49. Genschmer, K. R. *et al.* Activated PMN Exosomes: Pathogenic Entities Causing Matrix Destruction and Disease in the Lung. *Cell* **176**, 113-126.e15 (2019).
50. Yue, S., Mu, W., Erb, U. & Zöller, M. The tetraspanins CD151 and Tspan8 are essential exosome components for the crosstalk between cancer initiating cells and their surrounding. *Oncotarget* **6**, 2366–2384 (2015).
51. Umezu, T. *et al.* Exosomal miR-135b shed from hypoxic multiple myeloma cells enhances angiogenesis by targeting factor-inhibiting HIF-1. *Blood* **124**, 3748–3757 (2014).
52. Mineo, M. *et al.* Exosomes released by K562 chronic myeloid leukemia cells promote angiogenesis in a src-dependent fashion. *Angiogenesis* **15**, 33–45 (2012).
53. Théry, C. *et al.* Minimal information for studies of extracellular vesicles 2018 (MISEV2018): a position statement of the International Society for Extracellular Vesicles and update of the MISEV2014 guidelines. *J. Extracell. Vesicles* **7**, (2018).
54. Hoshino, A. *et al.* Tumour exosome integrins determine organotropic metastasis. *Nature* **527**, 329–335 (2015).
55. Hyenne, V. *et al.* Studying the Fate of Tumor Extracellular Vesicles at High Spatiotemporal Resolution Using the Zebrafish Embryo. *Dev. Cell* **48**, 554-572.e7 (2019).
56. Wiklander, O. P. B. *et al.* Extracellular vesicle in vivo biodistribution is determined by cell source, route of administration and targeting. *J. Extracell. Vesicles* **4**, 1–13 (2015).
57. Cohen, O. *et al.* 'Golden' exosomes as delivery vehicles to target tumors and overcome intratumoral barriers:: In vivo tracking in a model for head and neck cancer. *Biomater. Sci.* **9**, 2103–2114 (2021).
58. Imai, T. *et al.* Macrophage-dependent clearance of systemically administered B16BL6-derived exosomes from the blood circulation in mice. *J. Extracell. Vesicles* **4**, 1–8 (2015).
59. Lai, C. P. *et al.* Dynamic biodistribution of extracellular vesicles in vivo using a multimodal imaging reporter. *ACS Nano* **8**, 483–494 (2014).
60. Takahashi, Y. *et al.* Visualization and in vivo tracking of the exosomes of murine melanoma B16-BL6 cells in mice after intravenous injection. *J. Biotechnol.* **165**, 77–84 (2013).
61. Matsumoto, A. *et al.* Role of Phosphatidylserine-Derived Negative Surface Charges in the Recognition and Uptake of Intravenously Injected B16BL6-Derived Exosomes by Macrophages. *J. Pharm. Sci.* **106**, 168–175 (2017).
62. Levick, J. R. *FLOW THROUGH INTERSTITIUM AND OTHER FIBROUS MATRICES*. *Quarterly Journal of Experimental Phsyiology* **72**, (1987).
63. Shirure, V. S., Lezia, A., Tao, A., Alonzo, L. F. & George, S. C. Low levels of physiological interstitial flow eliminate morphogen gradients and guide angiogenesis. *Angiogenesis* **20**, 493–504 (2017).

64. Swartz, M. A. & Lund, A. W. Lymphatic and interstitial flow in the tumour microenvironment: Linking mechanobiology with immunity. *Nature Reviews Cancer* **12**, 210–219 (2012).
65. Hsu, Y. H. *et al.* Full range physiological mass transport control in 3D tissue cultures. *Lab Chip* **13**, 81–89 (2013).
66. Swartz, M. A. & Fleury, M. E. Interstitial Flow and Its Effects in Soft Tissues. *Annu. Rev. Biomed. Eng.* **9**, 229–256 (2007).
67. Swabb, E. A., Wei, J. & Cullino3, P. M. *Diffusion and Convection in Normal and Neoplastic Tissues*. *CANCER RESEARCH* **34**, (1974).
68. Chary, S. R. & Jain, R. K. Direct measurement of interstitial convection and diffusion of albumin in normal and neoplastic tissues by fluorescence photobleaching. *Proc. Natl. Acad. Sci. U. S. A.* **86**, 5385–5389 (1989).
69. Pedersen, J. A., Lichter, S. & Swartz, M. A. Cells in 3D matrices under interstitial flow: Effects of extracellular matrix alignment on cell shear stress and drag forces. *J. Biomech.* **43**, 900–905 (2010).
70. Lenzini, S., Bargi, R., Chung, G. & Shin, J. W. Matrix mechanics and water permeation regulate extracellular vesicle transport. *Nature Nanotechnology* (2020). doi:10.1038/s41565-020-0636-2
71. Huleihel, L. *et al.* Matrix-bound nanovesicles within ECM bioscaffolds. *Sci. Adv.* **2**, (2016).
72. Lo Cicero, A., Majkowska, I., Nagase, H., Di Liegro, I. & Troeberg, L. Microvesicles shed by oligodendroglioma cells and rheumatoid synovial fibroblasts contain aggrecanase activity. *Matrix Biol.* **31**, 229–233 (2012).
73. Dolo, V. *et al.* Selective localization of matrix metalloproteinase 9, β1 integrins, and human lymphocyte antigen class I molecules on membrane vesicles shed by 8701-BC breast carcinoma cells. *Cancer Res.* **58**, 4468–4474 (1998).
74. You, Y. *et al.* Matrix metalloproteinase 13-containing exosomes promote nasopharyngeal carcinoma metastasis. *Cancer Sci.* **106**, 1669–1677 (2015).
75. Mu, W., Rana, S. & Zöller, M. Host matrix modulation by tumor exosomes promotes motility and invasiveness. *Neoplasia (United States)* **15**, 875–887 (2013).
76. Gerlach, J. Q. & Griffin, M. D. Getting to know the extracellular vesicle glycome. *Molecular BioSystems* **12**, 1071–1081 (2016).
77. Jimenez, L. *et al.* Quantitative Proteomic Analysis of Small and Large Extracellular Vesicles (EVs) Reveals Enrichment of Adhesion Proteins in Small EVs. *J. Proteome Res.* **18**, 947–959 (2019).
78. Gangoda, L. *et al.* Proteomic Profiling of Exosomes Secreted by Breast Cancer Cells with Varying Metastatic Potential. *Proteomics* **17**, (2017).
79. Chin, A. R., Yan, W., Cao, M., Liu, X. & Wang, S. E. Polarized Secretion of Extracellular Vesicles by Mammary Epithelia. *J. Mammary Gland Biol. Neoplasia* **23**, 165–176 (2018).
80. Sung, B. H., Ketova, T., Hoshino, D., Zijlstra, A. & Weaver, A. M. Directional cell movement through tissues is controlled by exosome secretion. *Nat. Commun.* **6**, (2015).
81. Rhee, D. K., Park, S. H. & Jang, Y. K. Molecular signatures associated with transformation and progression to breast cancer in the isogenic MCF10 model. *Genomics* **92**, 419–428 (2008).
82. Choong, L. Y. *et al.* Proteome-wide profiling of the MCF10AT breast cancer progression model. *PLoS One* **5**, 1–8 (2010).
83. Maguire, S. L. *et al.* Three-dimensional modelling identifies novel genetic dependencies associated with breast cancer progression in the isogenic MCF10 model. *J. Pathol.* **240**, 315–328 (2016).
84. Soule, H. D. *et al.* Isolation and Characterization of a Spontaneously Immortalized Human Breast Epithelial Cell Line, MCF-10. *Cancer Res.* **50**, 6075–6086 (1990).
85. Miller, F. R. *et al.* Xenograft model of progressive human proliferative breast disease. *J.*

Natl. Cancer Inst. **85**, 1725–1732 (1993).
86. Miller, F. R., Santner, S. J., Tait, L. & Dawson, P. J. MCF10DCIS.com xenograft model of human comedo ductal carcinoma in situ. *J. Natl. Cancer Inst.* **92**, 1185–1186 (2000).
87. Santner, S. J. *et al.* Malignant MCF10CA1 cell lines derived from premalignant human breast epithelial MCF10AT cells. *Breast Cancer Res. Treat.* **65**, 101–110 (2001).
88. Neve, R. M. *et al.* A collection of breast cancer cell lines for the study of functionally distinct cancer subtypes. *Cancer Cell* **10**, 515–527 (2006).
89. Imbalzano, K. M., Tatarkova, I., Imbalzano, A. N. & Nickerson, J. A. Increasingly transformed MCF-10A cells have a progressively tumor-like phenotype in three-dimensional basement membrane culture. *Cancer Cell Int.* **9**, 1–11 (2009).
90. Bessette, D. C. *et al.* Using the MCF10A/MCF10CA1a breast cancer progression cell line model to investigate the effect of active, mutant forms of EGFR in breast cancer development and treatment using gefitinib. *PLoS One* **10**, (2015).
91. Behbod, F. *et al.* An intraductal human-in-mouse transplantation model mimics the subtypes of ductal carcinoma in situ. *Breast Cancer Res.* (2009). doi:10.1186/bcr2358
92. Espina, V. *et al.* Malignant Precursor Cells Pre-Exist in Human Breast DCIS and Require Autophagy for Survival. *PLoS One* **5**, (2010).
93. Risha, Y., Minic, Z., Ghobadloo, S. M. & Berezovski, M. V. The proteomic analysis of breast cell line exosomes reveals disease patterns and potential biomarkers. *Sci. Rep.* **10**, (2020).
94. Jordan, K. R. *et al.* Extracellular vesicles from young women's breast cancer patients drive increased invasion of non-malignant cells via the Focal Adhesion Kinase pathway: a proteomic approach. *Breast Cancer Res.* **22**, (2020).
95. Vu, L. T. *et al.* Tumor-secreted extracellular vesicles promote the activation of cancer-associated fibroblasts via the transfer of microRNA-125b. *J. Extracell. Vesicles* **8**, (2019).
96. Insua-Rodríguez, J. & Oskarsson, T. The extracellular matrix in breast cancer. *Adv. Drug Deliv. Rev.* **97**, 41–55 (2016).
97. McCave, E. J., Cass, C. A. P., Burg, K. J. L. & Booth, B. W. The normal microenvironment directs mammary gland development. *Journal of Mammary Gland Biology and Neoplasia* **15**, 291–299 (2010).
98. Aisenbrey, E. A. & Murphy, W. L. Synthetic alternatives to Matrigel. *Nature Reviews Materials* **5**, 539–551 (2020).
99. Sontheimer-Phelps, A., Hassell, B. A. & Ingber, D. E. Modelling cancer in microfluidic human organs-on-chips. *Nat. Rev. Cancer* **19**, 65–81 (2019).
100. Boussommier-Calleja, A., Li, R., Chen, M. B., Wong, S. C. & Kamm, R. D. Microfluidics: A New Tool for Modeling Cancer–Immune Interactions. *Trends in Cancer* **2**, 6–19 (2016).
101. Caballero, D. *et al.* Organ-on-chip models of cancer metastasis for future personalized medicine: From chip to the patient. *Biomaterials* **149**, 98–115 (2017).
102. Vacchelli, E. *et al.* Chemotherapy-induced antitumor immunity requires formyl peptide receptor 1. *Science (80-.).* **350**, 972–977 (2015).
103. Morales-Kastresana, A. *et al.* Labeling extracellular vesicles for nanoscale flow cytometry. *Sci. Rep.* **7**, (2017).
104. Sbalzarini, I. F. & Koumoutsakos, P. Feature point tracking and trajectory analysis for video imaging in cell biology. *J. Struct. Biol.* **151**, 182–195 (2005).
105. Unruh, J. Stowers ImageJ Plugins: Jay_Plugins.jar.
106. Sprague, B. L., Pego, R. L., Stavreva, D. A. & McNally, J. G. Analysis of binding reactions by fluorescence recovery after photobleaching. *Biophys. J.* **86**, 3473–3495 (2004).
107. Hollenbeck, K. J. INVLAP.M: A MATLAB function for numerical inversion of Laplace transforms by the de Hoog algorithm. (1998).
108. Whiteside, T. L. Exosomes and tumor-mediated immune suppression. *Journal of Clinical Investigation* **126**, 1216–1223 (2016).

109. Garcia-Martin, R., Brandao, B. B., Thomou, T., Altindis, E. & Kahn, C. R. Tissue differences in the exosomal/small extracellular vesicle proteome and their potential as indicators of altered tissue metabolism. *Cell Rep.* **38**, (2022).
110. Takada, Y., Ye, X. & Simon, S. The integrins. *Genome Biology* **8**, (2007).
111. Pouwels, J., Nevo, J., Pellinen, T., Ylänne, J. & Ivaska, J. Negative regulators of integrin activity. *Journal of Cell Science* **125**, 3271–3280 (2012).
112. Campbell, I. D. & Humphries, M. J. Integrin structure, activation, and interactions. *Cold Spring Harbor Perspectives in Biology* **3**, 1–14 (2011).
113. Park, E. J., Yuki, Y., Kiyono, H. & Shimaoka, M. Structural basis of blocking integrin activation and deactivation for anti-inflammation. *Journal of Biomedical Science* **22**, (2015).
114. Byron, A. *et al.* Anti-integrin monoclonal antibodies. *J. Cell Sci.* **122**, 4009–4011 (2009).
115. Zhang, K. & Chen, J. F. The regulation of integrin function by divalent cations. *Cell Adhesion and Migration* **6**, 20–29 (2012).
116. Axelrod, D., Koppel, D. E., Schlessinger, J., Elson, E. & Webb, W. W. Mobility measurement by analysis of fluorescence photobleaching recovery kinetics. *Biophys. J.* **16**, 1055–1069 (1976).
117. Sprague, B. L. & McNally, J. G. FRAP analysis of binding: Proper and fitting. *Trends in Cell Biology* **15**, 84–91 (2005).
118. Rossi, C. & Bianchi, E. Diffusion of small molecules. *Nature* **189**, 822–824 (1961).
119. McAndrews, K. M. & Kalluri, R. Mechanisms associated with biogenesis of exosomes in cancer. *Molecular Cancer* **18**, (2019).
120. Azmi, A. S., Bao, B. & Sarkar, F. H. Exosomes in cancer development, metastasis, and drug resistance: A comprehensive review. *Cancer and Metastasis Reviews* **32**, 623–642 (2013).
121. Andreu, Z. & Yáñez-Mó, M. Tetraspanins in extracellular vesicle formation and function. *Front. Immunol.* **5**, (2014).
122. Mizenko, R. R. *et al.* Tetraspanins are unevenly distributed across single extracellular vesicles and bias sensitivity to multiplexed cancer biomarkers. *J. Nanobiotechnology* **19**, (2021).
123. Nishiuchi, R. *et al.* Ligand-binding specificities of laminin-binding integrins: A comprehensive survey of laminin-integrin interactions using recombinant α3β1, α6β1, α7β1 and α6β4 integrins. *Matrix Biol.* **25**, 189–197 (2006).
124. Zaman, M. H. *et al. Migration of tumor cells in 3D matrices is governed by matrix stiffness along with cell-matrix adhesion and proteolysis*. *PNAS* **103**, (2006).
125. Kim, H. J. *et al.* 3D cellulose nanofiber scaffold with homogeneous cell population and long-term proliferation. *Cellulose* **25**, 7299–7314 (2018).
126. Gelain, F., Bottai, D., Vescovi, A. & Zhang, S. Designer self-assembling peptide nanofiber scaffolds for adult mouse neural stem cell 3-dimensional cultures. *PLoS One* **1**, (2006).
127. Anguiano, M. *et al.* Characterization of three-dimensional cancer cell migration in mixed collagen-Matrigel scaffolds using microfluidics and image analysis. *PLoS One* **12**, (2017).
128. Sung, B. H. & Weaver, A. M. Exosome secretion promotes chemotaxis of cancer cells. *Cell Adhes. Migr.* **11**, 187–195 (2017).
129. Zigmond, S. H. Ability of polymorphonuclear leukocytes to orient in gradients of chemotactic factors. *J. Cell Biol.* **75**, 606–616 (1977).
130. Narasimhan, P. B., Marcovecchio, P., Hamers, A. A. & Hedrick, C. C. Nonclassical Monocytes in Health and Disease. *Annu. Rev. Immunol.* **37**, 439–456 (2019).
131. Auffray, C., Fogg, D., Garfa, M., Lauvau, G. & Geissmann, F. Monitoring of Blood Vessels and Tissues by a Population of Monocytes with Patrolling Behavior. *Science (80-.).* **317**, 666–670 (2007).
132. Carlin, L. M. *et al.* Nr4a1-dependent Ly6Clow monocytes monitor endothelial cells and

orchestrate their disposal. *Cell* **153**, 362–375 (2013).
133. Hanna, R. N. *et al.* Patrolling monocytes control tumor metastasis to the lung. *Science (80-.).* **350**, 985–990 (2015).
134. Cassetta, L. & Pollard, J. W. Cancer immunosurveillance: Role of patrolling monocytes. *Cell Res.* **26**, 3–4 (2016).
135. Cassetta, L. *et al.* Human Tumor-Associated Macrophage and Monocyte Transcriptional Landscapes Reveal Cancer-Specific Reprogramming, Biomarkers, and Therapeutic Targets. *Cancer Cell* **35**, 1–15 (2019).
136. Feng, A. L. *et al.* CD16+ monocytes in breast cancer patients: Expanded by monocyte chemoattractant protein-1 and may be useful for early diagnosis. *Clin. Exp. Immunol.* **164**, 57–65 (2011).
137. Qian, B. Z. *et al.* CCL2 recruits inflammatory monocytes to facilitate breast-tumour metastasis. *Nature* **475**, 222–225 (2011).
138. Plebanek, M. P. *et al.* Pre-metastatic cancer exosomes induce immune surveillance by patrolling monocytes at the metastatic niche. *Nat. Commun.* (2017). doi:10.1038/s41467-017-01433-3
139. Ancuta, P. *et al.* Fractalkine preferentially mediates arrest and migration of CD16+ monocytes. *J. Exp. Med.* **197**, 1701–1707 (2003).
140. Aumailley, M. The Laminin Family. *Cell Adh. and Mig.* **7**, 48-55 (2013).